POLITECNICO
MILANO 1863

SCUOLA DI INGEGNERIA INDUSTRIALE
E DELL'INFORMAZIONE

Global Stability of Road Vehicle and Driver

Tesi di Laurea Magistrale in
Mechanical Engineering - Ingegneria Meccanica

Author: **Samuele Giacintucci**

Student ID: 992324
Advisor: Prof. Gianpiero Mastinu
Academic Year: 2022-23

Abstract

The loss of vehicle stability is a major cause of road accidents, with over one million fatalities recorded yearly in the world. Even novice drivers recognize that their vehicle may become uncontrollable under the action of severe perturbations, e.g. wind gusts or evasive maneuvers, yet a complete mathematical characterisation of unstable motions of vehicle-and-driver is still lacking. Studies on global stability of road vehicle and driver are in their infancy: many research avenues are open to exploration with the goal of increasing the active safety of vehicles, human-driven or automated. This work aims to start providing a substantial theoretical contribution in the field. Using a simple vehicle-and-driver model, considering an oversteering car, a subcritical Hopf bifurcation is found at relatively high forward speed, caused by the driver's delayed steering action. Both rectilinear and circular motions are characterized by a saddle-type limit cycle, which exists when the steady-state condition is still locally stable. The amplitude of the cycle grows as the vehicle speed decreases. For circular motion, multiple saddle limit cycles may exist simultaneously; this should be verified using a more complex model. To compute the stability region of the vehicle-and-driver model, a kinetic energy-based Lyapunov function is employed. The region shrinks closer to the Hopf bifurcation. The disturbed motion is stable if and only if the variation of kinetic energy vanishes at the end of the maneuver, suggesting that unstable motions could be detected by monitoring the evolution in time of the kinetic energy. The same goal could be achieved by monitoring specific kinematic indices or by measuring tyre forces. The latter strategy is most effective at low speeds; at high speeds, the stability threshold is instead quite lower than tyre saturation. Lastly, a stability criterion valid for motions close to the saddle limit cycle is derived based on Floquet theory, analysing the deviation of the trajectory from the cycle in relation to its manifolds. The criterion serves as a formal demonstration of how such cycles influence stable and unstable motions of vehicle-and-driver.

Keywords: Road vehicle, Driver, Global stability, Hopf bifurcation, Saddle-type limit cycle, Lyapunov function, Floquet theory

Abstract in Lingua Italiana

La perdita di stabilità del veicolo è una delle principali cause di incidenti stradali, con oltre un milione di vittime registrate annualmente nel mondo. Anche i guidatori meno esperti sanno che un veicolo può diventare incontrollabile in seguito a forti disturbi, come raffiche di vento o manovre evasive. Tuttavia, i moti instabili di veicolo e guidatore non sono ancora stati definiti del tutto dal punto di vista matematico. Gli studi sulla stabilità globale di veicolo e guidatore sono ancora agli albori: diverse strade di ricerca possono essere perseguite con l'obiettivo di aumentare la sicurezza dei veicoli, inclusi quelli a guida autonoma. Lo scopo della tesi è fornire un contributo teorico in questo campo. Utilizzando un modello semplice di veicolo e guidatore, considerando un veicolo sovrasterzante, si osserva una biforcazione di Hopf subcritica ad alta velocità, causata dal ritardo di sterzata del pilota. Sia il moto su rettilineo che quello in curva sono catatterizzati da un ciclo limite di tipo sella, che esiste quando la condizione di equilibrio è ancora stabile. L'ampiezza del ciclo cresce al diminuire della velocità del veicolo. Per il moto in curva, potrebbero esistere contemporaneamente più cicli sella; ciò dovrebbe essere verificato utilizzando un modello più complesso. Per calcolare la regione di stabilità del modello veicolo/guidatore, viene utilizzata una funzione di Lyapunov basata sull'energia cinetica. Avvicinandosi alla biforcazione di Hopf, la regione si restringe. Il moto perturbato è stabile se e solo se la variazione di energia cinetica si azzera a fine manovra, suggerendo che un moto instabile possa essere rilevato monitorando l'evoluzione temporale dell'energia cinetica. Lo stesso risultato potrebbe essere ottenuto monitorando specifici indici cinematici o misurando le forze generate dagli pneumatici. Quest'ultima strategia è più efficace a bassa velocità: a velocità elevate invece, la soglia di stabilità è molto inferiore rispetto alla saturazione degli pneumatici. Viene infine derivato un criterio di stabilità valido per moti in prossimità del ciclo limite sella, ricorrendo alla teoria di Floquet e analizzando la deviazione della traiettoria dal ciclo in relazione alle varietà di quest'ultimo. Il criterio fornisce anche una dimostrazione di come tali cicli influenzino i moti stabili e instabili di veicolo e guidatore.

Parole chiave: Veicolo, Guidatore, Stabilità globale, Biforcazione di Hopf, Ciclo limite sella, Funzione di Lyapunov, Teoria di Floquet

Contents

Introduction

A comprehensive mathematical description and classification of unstable motions of road vehicle and driver is currently lacking [1], despite nearly one billion vehicles running on roads all around the globe. The loss of vehicle stability stands out as one of the primary causes of road accidents, with over one million road fatalities being recorded yearly in the world. Substantial investments are being poured into R&D within the automotive sector, yet it is evident that safety remains a concern. With the advent of automated vehicles, that may be able to avoid instability phenomena typically exhibited by human-driven vehicles, today it becomes imperative to launch an extensive research program to address the unresolved issues on vehicle stability from a sound theoretical standpoint.

State of The Art

Vehicle stability is a broad term used in literature with reference to concepts such as active safety and handling behaviour. Stability can loosely be defined as the ability of a vehicle (and driver) to maintain the intended trajectory and speed under the action of external disturbances or after the execution of an abrupt maneuver. Even novice drivers recognize that their vehicle may become uncontrollable if an impulse force of *sufficient intensity* is applied. While this may represent an intuitive fact, a formal description of the underlying mechanisms that lead to unstable motions of vehicle-and-driver is still in its infancy. For instance, establishing a clear definition of "sufficient intensity", i.e. defining a threshold above which a disturbance makes the motion of vehicle-and-driver unstable, currently constitutes a significant challenge. To date, no carmaker nor national or international regulatory body has ever attempted or managed to provide practical information on any threshold [2]. Indeed, nowadays anti-spin controls are still often developed experimentally with a trial-and-error approach, with the vehicle being driven on low friction surfaces [1].

In academic books [1, 3, 4], studies on vehicle stability predominantly involve the linearized vehicle model, excluding the active control by the driver. Even when the driver is introduced in the loop, a linearized vehicle-and-driver system is considered. The analysis lacks of realism since it is conducted assuming that the vehicle experiences minor

disturbances from steady-state, which is never the case during evasive maneuvers or accidents. Stability is therefore assessed *locally*, i.e. referring to the motion restricted to a small neighbourhood of the equilibrium condition. If the disturbance is large, like in the situations mentioned, the motion of the system can only be properly characterized by utilizing full nonlinear models of both the vehicle and the driver. The different behaviours exhibited by a nonlinear system as its parameters are altered can be studied and classified using *bifurcation theory* [5–7]. Bifurcation theory provides the necessary tools to analyse the stability of vehicle-and-driver undergoing large motions, since it is able to obtain *global* information about the system dynamics, such as the presence of other attractors. Bifurcation analysis is an instrument very well-known to mathematicians, but still today it appears almost disregarded by automotive engineers.

Studies on stability of nonlinear road vehicle models started in 1973, when Pacejka [8] demonstrated the existence of multiple equilibria of various types (nodes and saddles), highlighting the issue of global stability and defining the *region of attraction* of a stable equilibrium. If a disturbance outside this region is applied to the vehicle, the motion becomes unstable. A simple single-track model was used. In 1998, Ono *et al.* [9] showed that the loss of vehicle control (spin phenomenon) is caused by a saddle-node bifurcation which depends heavily on rear tyre lateral force saturation. A simple single-track model was again used, considering a vehicle which is understeering at low lateral accelerations and oversteering at high lateral accelerations. In 2009, Edelmann and Plöchl [10] analysed the stability of the steady-state powerslide motion, both analytically (using a four-wheel vehicle model) and experimentally, demonstrating the existence of highly nonlinear behaviours exhibited by the vehicle in the real world. In 2012, Della Rossa *et al.* [11] produced a taxonomy of nonlinear behaviours of different types of vehicle, classified on the basis of tyre characteristics, with fixed steering and speed inputs. They exploited bifurcation analysis and analysed the global stability of the single-track model. Apart from various bifurcations, they found oscillatory motions in the form of *limit cycles* and verified that the bare undesteering vehicle is globally stable, i.e. able to absorb also strong disturbances. In 2017, Bobier-Tiu *et al.* [12] provided an overview of the use of phase portraits to design control strategies for vehicle stabilization, focusing on yaw rate and sideslip dynamics, referring to bifurcation theory. More recently, Lian and Li [13] computed the stability boundary of an 8-DoF vehicle model with fixed steering and speed inputs using a Lyapunov exponent based stability analysis method, validating the results experimentally.

Neither of the studies mentioned above included the active control by the driver. However, vehicle and driver form a closely coupled system and their interaction can fundamentally

change the behaviour of the vehicle. Indeed, already in 1994 Liu *et al.* [14] demonstrated that a simple 5-dimensional vehicle-and-driver system undergoes a Hopf bifurcation, with consequent generation of limit cycles whose stability depends also on driver control parameters. A disturbed straight running condition was considered, and even chaotic motions were observed. In a recent contribution by Biggio [15], the same analysis conducted in [11] was repeated on a 5-dimensional vehicle-and-driver model with first-order delayed steering dynamics. Again, the analysis was focused on rectilinear motion. Mastinu *et al.* [2] demonstrated that a Hopf bifurcation exists also when resorting to a third-order approximation of steering dynamics, with generation of saddle-type limit cycles. Experiments at the driving simulator with a human driver in the loop were done to verify the results and to define the region of asymptotic stability for the straight-line motion. Importantly, it was shown both numerically and experimentally that even an understeering vehicle can undergo a subcritical Hopf bifurcation when the driver is included in the loop, meaning that the coupled vehicle-and-driver system is not globally stable. A parallel work by Bertolami and Botto [16] provided indications on how real-time tyre force measurements can be used to improve vehicle stability. They found that the output of the Milliken Moment Method [4] approximates the region of attraction of equilibria of the vehicle-and-driver system far from the Hopf bifurcation, considering rectilinear motion. All the studies cited involved a human driver; nevertheless, automated vehicles might experience analogous stability issues (see for example [17, 18]). Additional papers that deal with bifurcation analysis of road vehicles, with or without driver control, are e.g. [19–23].

Project Rationale

To assist vehicle designers in developing safer vehicles, either human-driven or automated, there is an urgent need of quantifying the threshold above which a disturbance makes the motion of a road vehicle-and-driver unstable. In the literature, only one contribution has been identified that investigates the stability of vehicle and driver motion by developing a Lyapunov function, considering a vehicle-and-driver model of adequate complexity [2]. Likewise, only [16] was found to thoroughly examine the relationship between tyre forces and vehicle stability appropriately referring to the notions of global stability and region of attraction. More importantly, to the author's knowledge there are currently no contributions in literature aimed at studying the global stability of vehicle-and-driver negotiating a curve, as a bifurcation analysis of vehicle-and-driver running along a circular path has never been performed. In addition, the influence of limit cycles on stable and unstable motions of vehicle-and-driver remains unclear and there still is uncertainty among automotive engineers on whether acknowledging the existence of cycles could result beneficial

in practice. In this regard, perhaps the most relevant concern is whether it is possible to detect an unstable motion before the driver completely loses control of the vehicle, when a corrective action could be most effective in preventing an accident. Finally, the role played by the driver on the stability of the coupled system has not yet been adequately highlighted, nor has the mechanism leading to instability been thoroughly described from both a kinematic and energy standpoint. This thesis work aims to start addressing the evidenced gaps, albeit focusing on mathematical modelling, and stimulate further interest in the field of nonlinear dynamics applied to vehicle engineering.

The contents of this thesis are organized as follows: in Chapter 1, a mechanical model of the vehicle-and-driver system is developed, starting from the single-track vehicle model. The steering control action of the driver is introduced employing a single-point preview model, considering both rectilinear and circular reference trajectories. In Chapter 2, the local stability of the vehicle with and without driver control is studied as function of the forward speed, considering the linearized models, to make a preliminary assessment on the effect of the driver on vehicle stability. The analysis is enriched in Chapter 3, where bifurcation theory is exploited to fully characterize the nonlinear dynamical behaviours exhibited by the vehicle undergoing large motions, again both with and without driver control. Alongside vehicle speed and curve radius, independent parameters related to the driver are also varied to illustrate how the driver dramatically influences the overall behaviour of the coupled system. In Chapter 4, the global stability of the simple vehicle-and-driver model is analysed. Considering different driving conditions, the region of asymptotic stability of the equilibrium of the system in the lateral-velocity/yaw-rate plane is computed using a kinetic energy-based Lyapunov function. In Chapter 5, stable and unstable motions of vehicle and driver are described from the kinematic and energy standpoint. A strategy to detect as soon as the disturbance has acted if the motion of vehicle-and-driver is becoming unstable and provide an index that quantifies the severity of this condition is proposed in Chapter 6, also proving mathematically that the stability threshold for vehicle and driver can be computed referring directly to the saddle-type limit cycle. To achieve this goal, Floquet theory is applied. The thesis is concluded with a summary of the main results and an outlook for future research directions is provided.

1 | Vehicle and Driver Model

At the heart of any study aimed at characterizing the nonlinear dynamics of a vehicle lies a reliable vehicle model. While a highly complex model may be able to perfectly reproduce the behaviour of the vehicle under the most diverse operating conditions, it does not mean that it is the most appropriate to study a particular aspect of vehicle dynamics, since it may be hugely demanding in terms of computations and rely on numerous parameters which have to be tuned accordingly. Moreover, a complex model does not allow a thorough understanding of underlying physical phenomena, offered instead by simpler models.

In the first part of the chapter, a 2 Degrees of Freedom (DoF) single-track vehicle model is introduced. The single-track model is extensively used to mathematically characterize the lateral dynamics of the vehicle (see for example [11]), as it provides a comprehensive description of fundamental nonlinear behaviours despite its (apparent) simplicity. Throughout the entirety of this thesis work, it will be assumed that the vehicle maintains a constant forward speed, allowing to focus the attention on the remaining 2 DoF in the plane, i.e. lateral motion and yaw rotation. The steering action of a human driver will then be introduced in the second part of the chapter.

1.1. Vehicle Model

The vehicle model considered in this work is a 2 DoF single-track model that describes the lateral motion and yaw rotation of the vehicle, intended as a rigid beam that is free to move in the horizontal plane. The model is based on the following main assumptions:

- The vertical motion, roll and pitch rotations are neglected; this corresponds to assuming that the suspensions deflections and tyre vertical deformations are small, meaning that also the variations of camber and toe are not accounted for;
- The effect of aerodynamic forces on lateral dynamics is negligible;
- The width of the vehicle is neglected; tyres of the same axle are subject to the same slip angle, which is equal to the slip angle of a virtual tyre positioned at the centre of the axle;

- The forward velocity of the vehicle is constant;
- Tyre lateral forces are not affected by the longitudinal slip (longitudinal forces are small);
- Geometrical nonlinearities are neglected, i.e. the small angles approximation is used.

The single-track model is able to capture essential aspects of vehicle lateral dynamics, including the fundamental nonlinear behaviours that are relevant for studies concerning global stability. Nonetheless, the model maintains a manageable level of complexity and is therefore suitable for the preliminary mathematical characterization of these behaviours.

In the following, the equations of motion of the 2 DoF single-track vehicle model will be developed, starting from the description of the kinematic relations involved in the expressions of inertia forces and tyre lateral forces; the latter will be addressed in a separate section. Finally, the power balance equation for the system will be derived and the handling diagram theory will briefly be explained, as both topics are conceptually relevant in the context of vehicle stability.

1.1.1. Basic Kinematic Relations

The first step when building the model of any mechanical system is to identify the kinematic relations that define the position, velocity and acceleration of every element of the system, expressed in a reference system of choice. In this case, the reference frame for the vehicle is defined according to the SAE axis system, with the x-axis (versor $\mathbf{i}$) pointing towards the direction of forward movement, the z-axis (versor $\mathbf{k}$) perpendicular to the road and pointing downwards, and the y-axis (versor $\mathbf{j}$) obtained considering a right-hand system, indicating the lateral direction. The origin of the reference frame, which is fixed to the body as depicted in Fig. 1.1, is the vehicle centre of gravity G.

To completely describe the motion of a rigid body, it is in general sufficient to know its angular velocity $\boldsymbol{\omega}$ and the velocity $\boldsymbol{V}_P$ of a generic point P attached to the body. Then, recalling that the distance between any two points of a rigid body must always remain constant, the following fundamental vector equation can be written to express the velocity $\boldsymbol{V}_Q$ of any other point Q belonging to the body:

$$\boldsymbol{V}_Q = \boldsymbol{V}_P + \boldsymbol{\omega} \times (Q - P) \tag{1.1}$$

where $(Q-P)$ is the displacement vector from P to Q. For the vehicle, it results convenient expressing the velocity field as function of the velocity of the centre of gravity ($\boldsymbol{V}_G$) and the

yaw rate r, which is the only component of the angular velocity $\boldsymbol{\omega}$ due to the assumption of planar motion.

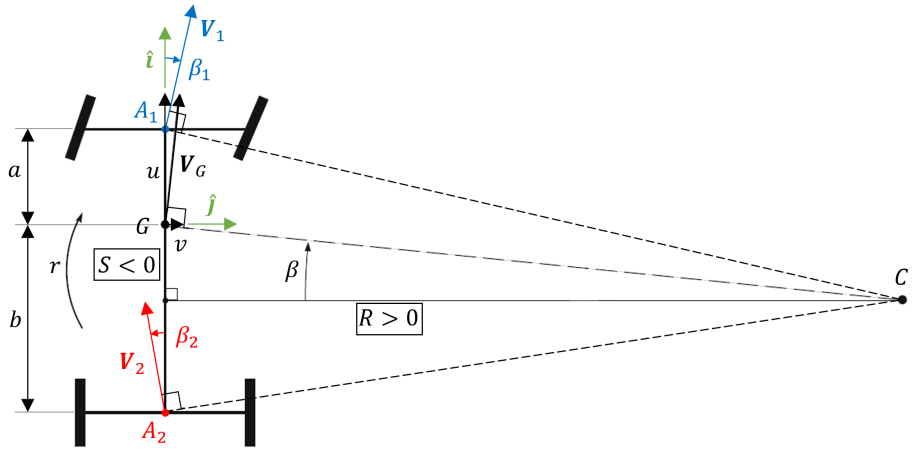

Figure 1.1: Main quantities related to the velocity field of a vehicle negotiating a curve. Adapted from [3].

The expression of $\boldsymbol{V}_G$ in the vehicle reference frame is:

$$\boldsymbol{V}_G = u\mathbf{i} + v\mathbf{j}$$

where u is the forward (longitudinal) velocity and v is the lateral velocity. The angle between $\boldsymbol{V}_G$ and the x-axis is called vehicle slip angle β:

$$\beta = \arctan\left(\frac{v}{u}\right) \tag{1.2}$$

and is one of the main quantities traditionally controlled by the ESP (Electronic Stability Program). The velocity vectors $\boldsymbol{V}_1$, $\boldsymbol{V}_2$ of the front and rear axle midpoints A_1, A_2 can now be computed using Eq. (1.1):

$$\boldsymbol{V}_1 = u\mathbf{i} + (v + ra)\mathbf{j} \tag{1.3}$$

$$\boldsymbol{V}_2 = u\mathbf{i} + (v - rb)\mathbf{j} \tag{1.4}$$

where a and b are the distance of the centre of mass from the front and rear axle respectively. The analogous expressions to (1.2) considering now the components of $\boldsymbol{V}_1$ and $\boldsymbol{V}_2$

yield the front (β_1) and rear (β_2) vehicle slip angles:

$$\beta_1 = \arctan\left(\frac{v + ra}{u}\right)$$
$$\beta_2 = \arctan\left(\frac{v - rb}{u}\right)$$

which are, in general, not equivalent to the tyre slip angles. The assumption of planar motion also implies that an instantaneous centre of zero velocity C (or *velocity centre*) can be defined on the body. Its coordinates in the vehicle reference frame can easily be found by solving Eq. (1.1) with $\boldsymbol{V}_Q = \boldsymbol{V}_C = \mathbf{0}$:

$$(C - G) = -\frac{v}{r}\mathbf{i} + \frac{u}{r}\mathbf{j} = S\mathbf{i} + R\mathbf{j}$$

At each instant during motion, the velocity field is equivalent to a pure rotation around the velocity centre C, so that the velocity of any given point Q of the body is perpendicular to the displacement vector $(Q - C)$. This is visualized in Fig. 1.1 for the velocity vectors $\boldsymbol{V}_G$, $\boldsymbol{V}_1$ and $\boldsymbol{V}_2$. It is important to remark that point C belongs to the rigid body and the property $\boldsymbol{V}_C = \mathbf{0}$ holds in general only instantaneously for that particular physical point. Indeed, the location of the velocity centre in space changes during motion, both in the body reference frame and in whichever ground-fixed reference system is considered. This concept will be further clarified in Section 5.2, where the notion of centrodes is introduced.

Once the velocity of the most notable points of the vehicle has been computed, their acceleration follows by taking the derivative with respect to time. Remembering that the versors of the vehicle reference system are not fixed in space, using the Poisson's formula for rotating versors yields the following expressions:

$$\mathbf{a}_G = (\dot{u} - vr)\mathbf{i} + (\dot{v} + ur)\mathbf{j} = a_x\mathbf{i} + a_y\mathbf{j} \tag{1.5}$$
$$\mathbf{a}_1 = (a_x - r^2 a)\mathbf{i} + (a_y + \dot{r}a)\mathbf{j} \tag{1.6}$$
$$\mathbf{a}_2 = (a_x + r^2 b)\mathbf{i} + (a_y - \dot{r}b)\mathbf{j} \tag{1.7}$$

where $\mathbf{a}_G$, $\mathbf{a}_1$ and $\mathbf{a}_2$ are the acceleration of the vehicle centre of mass, of the front axle midpoint and of the rear axle midpoint respectively. A more in-depth analysis of vehicle kinematics will be given in Chapter 5.

1.1.2. Tyre Lateral Forces

The characteristics of the fitted tyres are the most deciding factor in determining the handling behaviour of a road vehicle. It is therefore of utmost importance to incorporate in the vehicle model a tyre model which is able to accurately reproduce the forces exchanged between the tyres and the road surface. Traditionally, tyre models are categorized into physical and empirical models.

Physical models are developed considering phisically meaningful factors such as tyre stiffness, geometry and material properties. Some physical models can reach remarkable levels of complexity and are typically formulated using a finite elements approach, therefore while being the most accurate, they are not suitable for vehicle dynamics simulations, often being reserved for studies concerning rim-tyre interactions and NVH (Noise, Vibration, Harshness).

On the other hand, empirical models rely solely on experimental data collected during full-scale tests performed in laboratory and on road. Tyre forces and moments measured during testing are correlated to various input quantities, most notably tyre slips and vertical load. While conducting experimental campaigns to acquire the necessary data can be quite time-consuming, empirical models are widely used for vehicle dynamics simulations since they consist of analytical formulae or look-up tables which are quite efficient and reliable.

In this thesis work, the lateral tyre forces will be modelled using an adapted version of the Pacejka Magic Formula [8], which is one of the most well-known empirical tyre models. For the single-track vehicle model, one can directly refer to the total axle lateral force under the assumption that tyres of the same axle also share the same value of slip angle, equal to the angle calculated for an equivalent tyre placed in correspondence of the longitudinal axis of the vehicle. The slip angle at the front axle (α_f) and at the rear axle (α_r) of a front wheel steering vehicle read:

$$\alpha_f = \delta - \beta_1 \simeq \delta - \frac{v + ra}{u}$$
$$\alpha_r = -\beta_2 \simeq -\frac{v - rb}{u}$$

where δ is the steering angle, equal for both front tyres. The total lateral axle forces (or *axle characteristics*), either front (F_{y_f}) or rear (F_{y_r}), can be expressed as function of the slip angles using the Magic Formula, assuming that the effect of combined slip due to the

presence of longitudinal forces is negligible:

$$F_{y_i} = D_i \sin(C_i \arctan(B_i\alpha_i - E_i(B_i\alpha_i - \arctan(B_i\alpha_i))))$$

for $i = \{f, r\}$. B_i, C_i, D_i, E_i are the coefficients of the Magic Formula referred to axle i. These coefficients generally depend on the characteristics of the selected tyre, on road surface conditions, tyre pressure, vertical load on the tyre, camber angle and, since in this case the whole axle is being considered, on the equivalent roll stiffness of the axle. The values of the Magic Formula coefficients considered in this work are listed in Table 1.1. The characteristic curves of front and rear axle are visible in Fig. 1.2. It should be noted that the sign of the forces (and of the slip angles) is coherent with the vehicle reference system of Fig. 1.1. While the Magic Formula is often used to characterize also the longitudinal forces, in the present work it will not be necessary as the longitudinal dynamics is disregarded due to the hypothesis of constant forward velocity u.

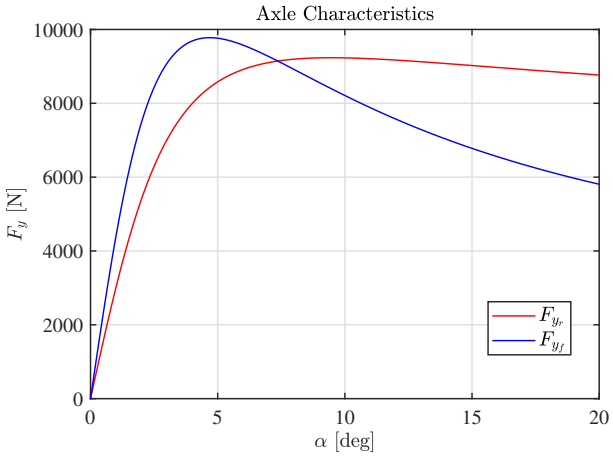

Figure 1.2: Front (F_{y_f}) and rear (F_{y_r}) axle characteristics of the considered vehicle (tyre data in Table 1.1).

1.1.3. Equations of Motion

The equations of motion of the vehicle can be obtained using the dynamical equilibrium equations for a rigid body in the plane:

$$\begin{cases} m\mathbf{a}_G = \boldsymbol{F}_t \\ J\dot{r} = \boldsymbol{M}_t \end{cases}$$

where m and J are respectively the vehicle's mass and moment of inertia about the z-axis, while $\boldsymbol{F}_t$ and $\boldsymbol{M}_t$ are the total force and moment applied on the vehicle body. With

reference to Fig. 1.3 one can immediately write:

$$\begin{cases} ma_x = F_{x_f} + F_{x_r} \\ ma_y = F_{y_f} + F_{y_r} + F \\ J\dot{r} = F_{y_f} a - F_{y_r} b + M \end{cases} \tag{1.8}$$

where F is an external force that acts at the vehicle centre of mass, M is an external yaw moment and F_{x_i} is the longitudinal force applied at axle i. It is assumed that the steering angle is small, so that the longitudinal component of F_{y_f} and the lateral component of F_{x_f} can be neglected. F and M are impulsive actions, that act as disturbances and are generally not present while the vehicle is in motion. They will not be directly considered for numerical computations throughout this work, but one should always be mindful of the fact that F and M are the physical actions that generate disturbances given in terms of lateral velocity v and yaw rate r respectively.

Considering the expression of the longitudinal (a_x) and lateral (a_y) acceleration from Eq. (1.5) and assuming constant forward velocity ($\dot{u} = 0$), system (1.8) can be rewritten as:

$$\begin{cases} -mvr = F_{x_f} + F_{x_r} & \text{(1.9a)} \\ \dot{v} = \dfrac{1}{m}\left(F_{y_f} + F_{y_r} + F\right) - ur & \text{(1.9b)} \\ \dot{r} = \dfrac{1}{J}\left(F_{y_f} a - F_{y_r} b + M\right) & \text{(1.9c)} \end{cases}$$

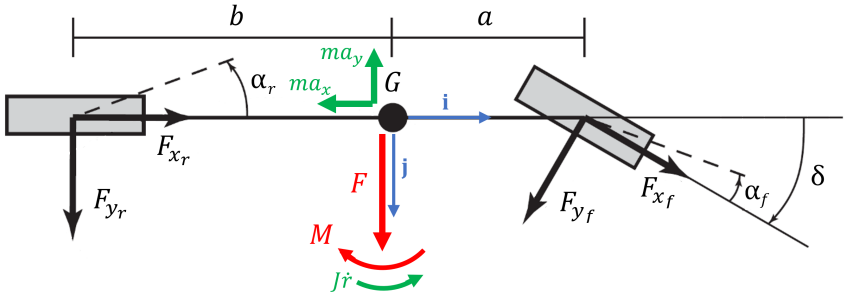

Figure 1.3: Single-track vehicle model. Adapted from [11].

The vehicle data considered in this work are listed in Table 1.2. Of the three equations above, only (1.9b) and (1.9c) are necessary to completely describe the motion of the bare vehicle at constant velocity (2 DoF model). Eq. (1.9a) is reported nonetheless due to its relevance in the power balance equation, as it will be commented in the following.

1.1.4. Power Balance Equation

The power balance equation for a mechanical system is derived from the principle of virtual work; it encapsulates the fundamental principle of conservation of energy and it is a useful tool to quickly obtain the equation of motion of 1 DoF systems. The general form of the power balance equation reads:

$$\frac{dE_k}{dt} = \sum_i W_i \tag{1.10}$$

where E_k is the kinetic energy of the system and W_i is the power of any active force or moment (either internal or external).

In the context of vehicle dynamics, the power balance equation is typically employed to assess the performance of the vehicle in the longitudinal direction by comparing tractive power and resistance power, computing for example the vehicle maximum speed and the acceleration time required to reach a particular speed. Considering instead the single-track vehicle model (1.9) developed for lateral dynamics, Eq. (1.10) reads:

$$\frac{dE_k}{dt} = \boldsymbol{F}_{y_f} \cdot \boldsymbol{V}_1 + \boldsymbol{F}_{y_r} \cdot \boldsymbol{V}_2 + (F_{x_f} + F_{x_r})u + Fv + Mr \tag{1.11}$$

where "$\cdot$" indicates the dot product of vectors and $\boldsymbol{F}_{y_i} = F_{y_i}\mathbf{j}$. By means of Konig's theorem, the kinetic energy of the vehicle can be expressed as:

$$E_k = \frac{1}{2}mu^2 + \frac{1}{2}mv^2 + \frac{1}{2}Jr^2$$

Considering now Eq. (1.3) for $\boldsymbol{V}_1$, Eq. (1.4) for $\boldsymbol{V}_2$ and the equilibrium in the longitudinal direction (1.9a), remembering also that and that $\frac{1}{2}mu^2 = const.$ due to the assumption of constant forward speed, one can finally rewrite Eq. (1.11) as:

$$\frac{dE_k}{dt} = \frac{d}{dt}\left(\frac{1}{2}mv^2 + \frac{1}{2}Jr^2\right) = F_{y_f}(v + ra) + F_{y_r}(v - rb) - muvr + Fv + Mr \tag{1.12}$$

Key aspects to be highlighted are:

- The power at the rear axle of a front wheel steering vehicle is always dissipative, i.e. $P_{y_r} = F_{y_r}(v - rb) \leq 0$. This can easily be verified at low lateral accelerations by considering the linearized expression of F_{y_r}, obtaining $P_{y_r} = -\frac{C_r}{u}(v - rb)^2$ which is always either zero or negative (C_r is the cornering stiffness evaluated at $\alpha_r = 0$). At high lateral accelerations, it is sufficient to remember that the sign of F_{y_r} remains consistent with that of the slip angle α_r, so $P_{y_r} \leq 0$ still holds true;

- The power at the front axle is not always dissipative. This is entirely attributable to the driver's steering action δ;
- Notwithstanding the disturbances F and M, which generally only act at the very first instants of the vehicle motion, the main contribution of positive power into the system is due to the longitudinal forces needed to keep the forward velocity constant: $P_x = -mvur \geq 0$ if $vr \leq 0$. Moreover, Eq. (1.12) also indicates that this power, if positive, directly translates to an increase of the kinetic energy associated to the lateral and rotational components of the motion.

Analysing how the powers (and consequently the energy) evolve during vehicle motion could be fundamental to characterize the unstable behaviour of the vehicle. This concept will be further clarified in Chapters 4 and 5.

1.1.5. Handling Diagram

The Handling Diagram theory [1, 3, 8] is one of the most essential tools in vehicle dynamics, commonly used to quickly highlight the steady-state cornering behaviour of the vehicle and analyse nonlinearities related to the tyre characteristics at high lateral accelerations. Its construction requires only a limited amount of data, therefore it can be employed to quickly understand the influence of basic changes in the setup of the vehicle. In essence, the handling diagram collects all the equilibrium states of the vehicle during cornering in terms of front and rear slip angles, steering angle, lateral acceleration and curve radius.

The diagram can be derived by rearranging the equations of motion of the vehicle (1.9b) and (1.9c), with the addition of two equations that describe the equilibrium in the vertical direction:

$$F_{z_f} = mg\frac{b}{a+b}$$
$$F_{z_r} = mg\frac{a}{a+b}$$

where g is the gravitational acceleration and F_{z_i} is the vertical load acting on axle i. Considering that the lateral acceleration a_y at steady-state ($\dot{v} = 0$) is $a_y = ur = u^2/R$, one can eventually obtain the following fundamental relation:

$$\frac{F_{y_f}}{F_{z_f}} = \frac{F_{y_r}}{F_{z_r}} = \frac{u^2}{Rg} \tag{1.13}$$

which indicates that the ratio between the lateral axle force and vertical axle force (the *effective* axle characteristic) is equal to the normalized lateral acceleration, both at the

front and at the rear axle. It should be noted that in general the coordinate of the velocity centre along the y-axis of the vehicle reference frame (R) is not exactly equal to the radius of curvature of the negotiated curve, therefore the lateral acceleration a_y is not equal to the centripetal acceleration; in any case, the approximation is acceptable since the longitudinal component of the centripetal acceleration is often quite small (the vehicle slip angle β is small).

Eq. (1.13) implies that at each level of lateral acceleration, one can identify the slip angle at the front (α_f) and at the rear (α_r) needed to satisfy the steady-state condition by utilizing the effective axle characteristics. The handling curve can then be traced by collecting the difference $\alpha_f - \alpha_r$ at each given value of $u^2/(Rg)$, until either axle reaches its peak normalized load. The curve related to the vehicle considered in this work is visible in Fig. 1.4. The curve is divided into four parts, each corresponding to equilibrium conditions in which the axles are either working before or after the respective saturation limit.

Through simple kinematic considerations, the steering angle δ can be approximated as:

$$\delta = \frac{a+b}{R} + \alpha_f - \alpha_r \tag{1.14}$$

Eq. (1.14) describes a straight line with slope $-u^2/(g(a+b))$ in the $(\alpha_f - \alpha_r,\, u^2/(Rg))$ plane; the line intersects the horizontal axis in correspondence of the steering angle δ. For any given combination of driver inputs $(u,\, \delta)$, all the steady-state conditions of the vehicle are identified by the intersection points of the straight line with the handling curve, as illustrated in Fig. 1.4.

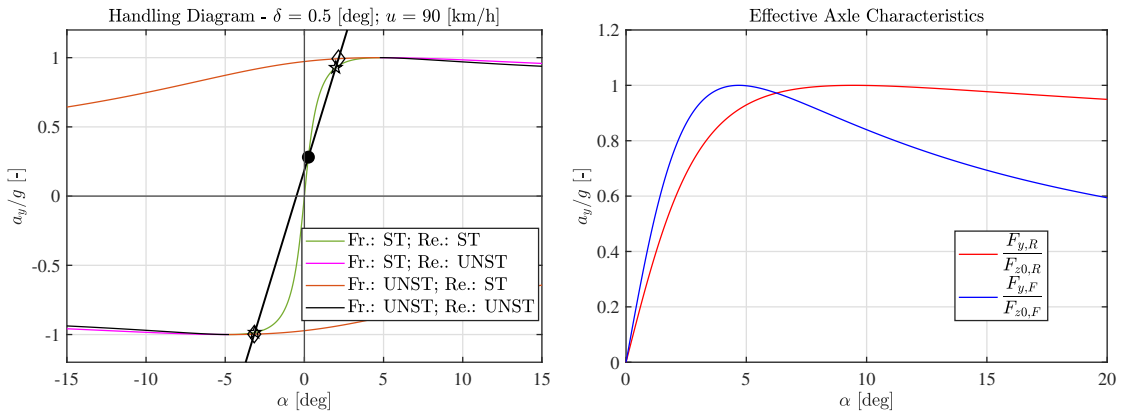

Figure 1.4: Handling diagram and effective axle characteristics (tyres and vehicle data in Tables 1.1 and 1.2).

The handling diagram also allows to easily recognize the understeering/oversteering character of the vehicle and its (local) stability at various levels of lateral acceleration. The understeering gradient is defined as:

$$UG = \frac{\partial(\delta - \delta_0)}{\partial(u^2/(Rg))} = \frac{\partial(\alpha_f - \alpha_r)}{\partial(u^2/(Rg))}$$

where $\delta_0 = (a+b)/R$ is the Ackermann steering angle. If $UG > 0$ (resp. < 0) the vehicle is classified as understeering (resp. oversteering). UG can be computed at any lateral acceleration level, therefore the character of the vehicle may vary along the handling curve; nonetheless, UG is more meaningful for lower values of a_y. The handling diagram represented in Fig. 1.4 pertains to an oversteering vehicle, which may become understeering at high lateral acceleration. This one of the most dangerous cases for what concerns stability [1], also because an abrupt change of vehicle behaviour is quite confusing for the driver.

The authors of [11] studied the dynamical behaviour of various types of vehicles, classified on the basis of their handling curve. In the present work, only one vehicle will be considered. The handling diagram will be utilized in Section 3.2 to compute the equilibria of the bare vehicle for different combinations of inputs (δ, u), investigating how the phase portrait of the vehicle is modified accordingly.

1.2. Driver Model

One of the most complex tasks when studying vehicle and driver stability is to appropriately model the control action of a human driver. It should be well understood that vehicle and driver form a closely coupled system, although the main focus in literature has always been to study the dynamical behaviour of the bare vehicle [24]. While typically the control action of the driver is purposely not included in studies concerning handling optimization since the primary focus is to design a vehicle that can perform well for the most generic driver, the interaction between vehicle and driver cannot be disregarded when the assessment is primarily focused on stability, as it will be seen in the following chapters. Unfortunately, driver models available today are not validated and a complete mathematical description of the human driver has not been achieved yet, hence the research efforts currently being reserved to this topic in particular.

The most relevant feature of human drivers from a modelling standpoint is their ability to predict the future state of the vehicle (in particular its trajectory) and adapt their actions, i.e. steering and throttle application, based on the acquired information. This

characteristic is a result of the driver looking ahead and being (to some extent) knowledgeable about how the vehicle is going to behave depending on its characteristics. One of the main challenges of developing a driver model which accurately emulates reality perhaps arises from the fact that preview information cannot be parameterized using a fixed quantity; it depends for example on the vehicle speed, vehicle conditions, type of maneuver and other external factors, which render the complete mathematical description of the decision-making process of the human driver extremely difficult.

For instance, current driver models seem not so efficient to react to a disturbance or to control a drifting vehicle [2]. Models based on neural networks could be the most effective in this sense, but they are entirely detached from the underlying physical phenomenon and essentially operate as black boxes. Models developed using control theory are instead well suited to investigate the effect of parameters with concrete physical meaning on the dynamics of the vehicle-and-driver system, which is one of the goals of the present work. A complete classification of driver models is out of the scope of this thesis work; the interested reader is referred to [24–27] for further details.

In the upcoming sections, a proportional-derivative steering controller is integrated with the vehicle model (1.9) to mimic the action of the driver. The driver's objective is to minimize the error between a reference path and the actual trajectory of the vehicle. Both the motion along a straight line and a along circular trajectory will be considered.

1.2.1. Straight Path Model

In this section, the driver model for rectilinear motion is developed according to [24]. We analyse the well-known path follower, which is the simplest driver model possible. With reference to Fig. 1.5, a preview point P is defined along the vehicle longitudinal axis at a distance L from the vehicle centre of mass G. During the maneuver, the driver controls the steering wheel to position point P on a reference straight path.

Defining the path error e requires the introduction of a global reference frame, whose coordinate axes X (versor $\mathbf{i_0}$) and Y (versor $\mathbf{j_0}$) are visible in the figure. Without loss of generality, the rectilinear path can simply be taken at $Y = Y_{ref} = 0$, and the error can be computed along the direction perpendicular to the path. The distance L is the mathematical equivalent of the driver's predictive ability, as he/she recognizes (computes) the deviation of the vehicle from the reference path in the immediate future. It is assumed that the preview distance L is proportional only to the vehicle forward velocity u by a constant preview time T_p, so $L = T_p u$. Although it was previously noted how the driver adjusts the preview information based on multiple factors, the dependence on the speed

is the most fundamental to be highlighted without excessively adding to the complexity of the model.

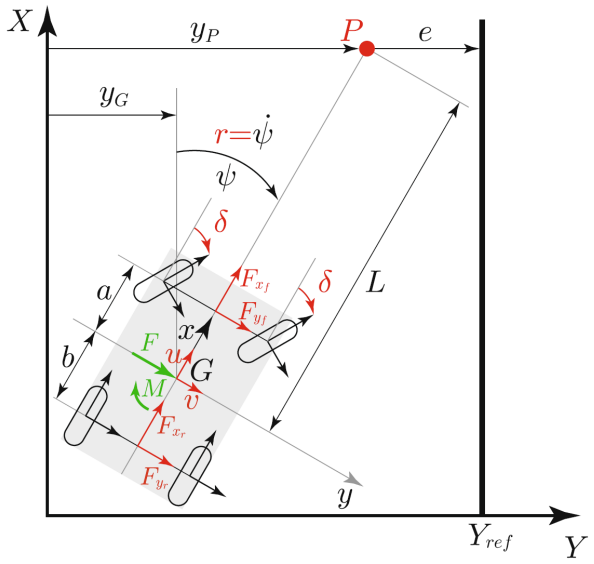

Figure 1.5: Simple vehicle-and-driver model for rectilinear motion. Reproduced from [2].

The coordinates of point P in the global reference system read:

$$(P-O) = (x_G + L\cos(\psi))\mathbf{i_0} + (y_G + L\sin(\psi))\mathbf{j_0} = x_P\mathbf{i_0} + y_P\mathbf{j_0} \tag{1.15}$$

where x_G and y_G are the global coordinates of the vehicle centre of mass and ψ is the yaw angle with respect to the X axis. The velocity of the preview point follows by deriving Eq. (1.15) with respect to time, obtaining:

$$\boldsymbol{V}_P = (\dot{x}_G - L\dot{\psi}\sin(\psi))\mathbf{i_0} + (\dot{y}_G + L\dot{\psi}\cos(\psi))\mathbf{j_0} = \dot{x}_P\mathbf{i_0} + \dot{y}_P\mathbf{j_0}$$

where $\dot{\psi} = r$. The path error e and its derivative $\dot{e}$ can then be computed as:

$$e = (Y_{ref} - y_P) = -y_P = -(y_G + L\sin(\psi)) \tag{1.16}$$

$$\dot{e} = -\dot{y}_P = -(\dot{y}_G + Lr\cos(\psi)) \tag{1.17}$$

where $\dot{y}_G = u\sin(\psi) + v\cos(\psi)$.

In this model, the steering action of the driver is provided by a Proportional-Derivative (PD) controller; this way, the transparency needed to study the effects of meaningful physical parameters associated with the driver on vehicle dynamics is still retained. For example, the proportional gain k_p controls how much steering angle the driver applies for a

given deviation from the reference trajectory: more nervous drivers would be characterized by a higher value of k_p. The derivative gain k_d indicates instead the extent of the driver's action in response to variations of the path error over time. Again, it should be noted that human drivers are able to adapt their parameters to maintain stability, or change their parameters in different driving conditions [20]: in the present work it is assumed that this effect is negligible, i.e. that the driver parameters are constant for a given forward speed.

Introducing a delay τ in the steering action is of paramount importance, to include in the mathematical model the time required for the real driver to gather information about the vehicle's state and surroundings, make a decision based on this information and finally execute the action physically. This holds true both for human-driven vehicles and automated vehicles [17], even if the actual process is different in practice. The typical delay for human drivers, who are the focus of the present work, is around 0.2 s [2], but can vary considerably depending on the age and psychophysical state of the subject. With this understanding, the steering angle applied by the driver can be expressed as:

$$\delta(t+\tau) = k_p e(t) + k_d \dot{e}(t) \tag{1.18}$$

It is assumed that δ saturates at a maximum value of δ_{sat}. A limit $\dot{\delta}_{sat}$ is also imposed to the steering angular velocity $\dot{\delta}$, since the driver is incapable of steering at an infinite rate. In control theory, a delay τ would typically be included in the model by employing a transfer function $G_0(s) = e^{s\tau}$, which multiplies the steering angle $\delta(s)$ in the frequency domain (s is the Laplace variable). Applying the Laplace transform to Eq. (1.18) then yields:

$$G_0(s)\delta(s) = k_p e(s) + k_d s e(s)$$

To continue the analysis in the time domain, $G_0(s)$ can be taylor-expanded around $s = 0$:

$$G_0(s) = 1 + \tau s + \frac{1}{2}\tau^2 s^2 + \frac{1}{6}\tau^3 s^3 + ...$$

As proposed in [2] we adopt here a third-order Taylor approximation, which is found to be a good compromise between accuracy and complexity for steering corrections of frequency up to about 1 Hz. The approximation is meaningful as the delay τ is relatively small. Reverting to the time domain, Eq. (1.18) can finally be approximated as:

$$\delta(t) + \tau\dot{\delta}(t) + \frac{1}{2}\tau^2\ddot{\delta}(t) + \frac{1}{6}\tau^3\dddot{\delta}(t) = k_p e(t) + k_d \dot{e}(t) \tag{1.19}$$

The above expression of the delayed steering dynamics is mainly what sets apart the current driver model from those utilized in previous studies concerning the stability of

vehicle-and-driver, such as [15, 20]. To summarize, the driver model adds five new equations to the equations of motion of the bare vehicle (1.9), corresponding to five additional state variables ψ, y_G, δ, δ_1, δ_2:

$$\begin{cases} \dot{\psi} = r \\ \dot{y}_G = u\sin(\psi) + v\cos(\psi) \\ \dot{\delta} = \delta_1 \\ \dot{\delta}_1 = \delta_2 \\ \dot{\delta}_2 = \dfrac{6}{\tau^3}\left(-\delta - \tau\delta_1 - \dfrac{\tau^2}{2}\delta_2 + k_p e + k_d \dot{e}\right) \end{cases} \tag{1.20}$$

where e and $\dot{e}$ can be computed using Eqs. (1.16) and (1.17). The complete set of equations of the vehicle-and-driver system for rectilinear motion will be presented in Section 1.3. Data of the reference driver considered throughout this work is listed in Table 1.3.

1.2.2. Circular Path Model

The single-point preview driver model developed in the previous section can be adapted for driving along a circular trajectory of radius ρ. The fundamentals of the model remain unaltered: the steering action is provided by a PD controller and a third-order approximation of steering dynamics is still employed. The only alteration relates to how the path error at the preview point P is computed, which requires switching to a polar coordinate system. With reference to Fig. 1.6, the position of the centre of mass of the vehicle with respect to the circular path can be described by a radial coordinate d_G, positive towards the outside of the turn, and an angular coordinate θ, positive clockwise. Using trigonometry, the path error along the radial direction and its time derivative now read:

$$e = \sqrt{(L\sin(\theta))^2 + (L\cos(\theta) + d_G + \rho)^2} - \rho \tag{1.21}$$

$$\dot{e} = \frac{1}{2(e+\rho)}\left[2L^2\dot{\theta}\sin(\theta)\cos(\theta) + 2(L\cos(\theta) + d_G + \rho)(-L\dot{\theta}\sin(\theta) + \dot{d}_G)\right] \tag{1.22}$$

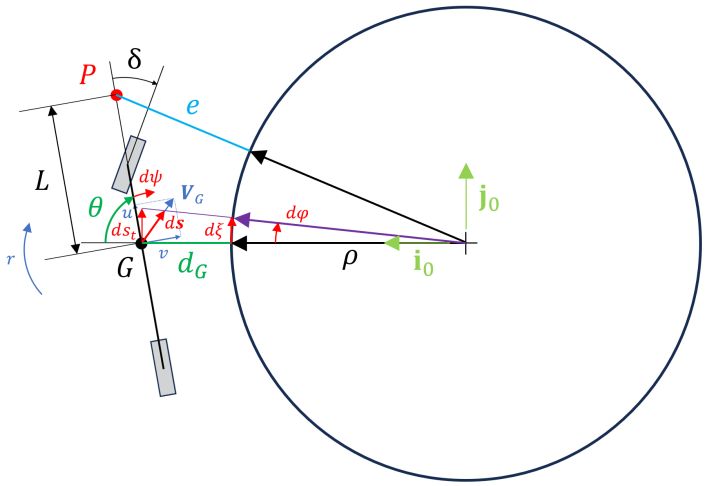

Figure 1.6: Simple vehicle-and-driver model for driving along a circular path.

The steering angle applied by the driver is then expressed by Eq. (1.18), which is again approximated using a third-order expansion to obtain Eq. (1.19), that describes the steering dynamics.

To compute the time derivatives of d_G and θ, it is useful to momentarily resort to a cartesian reference frame formed by a versor $\mathbf{i_0}$ positioned along the radial direction and a versor $\mathbf{j_0}$ tangent to the circular trajectory, as in Fig. 1.6. The velocity $\boldsymbol{V}_G$ of the centre of mass can then be expressed as:

$$\boldsymbol{V}_G = u\mathbf{i} + v\mathbf{j} = (u\cos(\theta) - v\sin(\theta))\mathbf{i_0} + (u\sin(\theta) + v\cos(\theta))\mathbf{j_0} \tag{1.23}$$

$\dot{d}_G$ is simply the projection of $\boldsymbol{V}_G$ in the radial direction:

$$\dot{d}_G = u\cos(\theta) - v\sin(\theta)$$

Computing $\dot{\theta}$ requires some additional passages. Let us consider the infinitesimal variation of the angle θ, which we call $d\theta$. This variation can be split into two contributions: referring again to Fig. 1.6, $d\psi$ is the actual infinitesimal yaw rotation of the vehicle related to the yaw rate r; $d\varphi$ is instead the component of $d\theta$ exclusively attributed to the curvature of the reference trajectory (it is perhaps easy to understand by observing Fig. 1.6 that even if the vehicle were to move straight, the desired path would "curve away" from it). One can therefore write:

$$d\theta = -d\varphi + d\psi \tag{1.24}$$

The expression of $d\psi$ is straightforward:

$$d\psi = r dt \tag{1.25}$$

where dt is an infinitesimal increment of time. To obtain $d\varphi$, we first introduce the infinitesimal displacement of the vehicle centre of mass: $d\boldsymbol{s} = \boldsymbol{V}_G dt$; its projection along the tangential direction, remembering Eq. (1.23), is:

$$ds_t = (u\sin(\theta) + v\cos(\theta))dt \tag{1.26}$$

The angle $d\varphi$ is equal to the ratio between the infinitesimal variation of the curvilinear coordinate along the circular path ($d\xi$) and the curve radius ρ. This ratio can be computed as (see Fig. 1.6):

$$d\varphi = \frac{d\xi}{\rho} = \frac{ds_t}{\rho + d_G} \tag{1.27}$$

Combining Eqs. (1.24), (1.25), (1.26) and (1.27) we obtain the following expression for $d\theta$:

$$d\theta = \left(r - \frac{u\sin(\theta) + v\cos(\theta)}{\rho + d_G}\right) dt = \dot{\theta} dt$$

which finally gives the expression of $\dot{\theta}$.

In summary, the driver model adds once again five new equations to the equations of motion of the bare vehicle (1.9), corresponding to five additional variables θ, d_G, δ, δ_1, δ_2:

$$\begin{cases} \dot{\theta} = r - \dfrac{u\sin(\theta) + v\cos(\theta)}{\rho + d_G} \\ \dot{d}_G = u\cos(\theta) - v\sin(\theta) \\ \dot{\delta} = \delta_1 \\ \dot{\delta}_1 = \delta_2 \\ \dot{\delta}_2 = \dfrac{6}{\tau^3}\left(-\delta - \tau\delta_1 - \dfrac{\tau^2}{2}\delta_2 + k_p e + k_d \dot{e}\right) \end{cases} \tag{1.28}$$

where e and $\dot{e}$ can be computed using Eqs. (1.21) and (1.22). The complete set of equations of the vehicle-and-driver system for circular motion will be presented in Section 1.3. Data of the reference driver is the same considered for rectilinear path tracking, listed in Table 1.3.

1.3. Vehicle-and-Driver Equations of Motion

For ease of reading, the complete sets of equations of the vehicle-and-driver models developed above are reported in this separate section. For rectilinear motion, combining Eqs. (1.9) and (1.20) we obtain the following system with 7 state variables $\boldsymbol{z} = \{v,\, r,\, \psi,\, y_G,\, \delta,\, \delta_1,\, \delta_2\}^{\mathrm{T}}$:

$$\begin{cases} \dot{v} = \dfrac{1}{m}\left(F_{y_f} + F_{y_r} + F\right) - ur \\ \dot{r} = \dfrac{1}{J}\left(F_{y_f}a - F_{y_r}b + M\right) \\ \dot{\psi} = r \\ \dot{y}_G = u\sin(\psi) + v\cos(\psi) \\ \dot{\delta} = \delta_1 \\ \dot{\delta}_1 = \delta_2 \\ \dot{\delta}_2 = \dfrac{6}{\tau^3}\left(-\delta - \tau\delta_1 - \dfrac{\tau^2}{2}\delta_2 + k_p e + k_d \dot{e}\right) \end{cases} \tag{1.29}$$

where:

$$e = -(y_G + L\sin(\psi)) \tag{1.16'}$$

$$\dot{e} = -(\dot{y}_G + Lr\cos(\psi)) \tag{1.17'}$$

Considering instead a reference circular path of radius ρ, combining systems (1.9) and (1.28) we obtain the following system with 7 state variables $\boldsymbol{z} = \{v,\, r,\, \theta,\, d_G,\, \delta,\, \delta_1,\, \delta_2\}^{\mathrm{T}}$:

$$\begin{cases} \dot{v} = \dfrac{1}{m}\left(F_{y_f} + F_{y_r} + F\right) - ur \\ \dot{r} = \dfrac{1}{J}\left(F_{y_f}a - F_{y_r}b + M\right) \\ \dot{\theta} = r - \dfrac{u\sin(\theta) + v\cos(\theta)}{\rho + d_G} \\ \dot{d}_G = u\cos(\theta) - v\sin(\theta) \\ \dot{\delta} = \delta_1 \\ \dot{\delta}_1 = \delta_2 \\ \dot{\delta}_2 = \dfrac{6}{\tau^3}\left(-\delta - \tau\delta_1 - \dfrac{\tau^2}{2}\delta_2 + k_p e + k_d \dot{e}\right) \end{cases} \tag{1.30}$$

where:

$$e = \sqrt{(L\sin(\theta))^2 + (L\cos(\theta) + d_G + \rho)^2} - \rho \tag{1.21'}$$

$$\dot{e} = \frac{1}{2(e+\rho)}\left[2L^2\dot{\theta}\sin(\theta)\cos(\theta) + 2(L\cos(\theta) + d_G + \rho)(-L\dot{\theta}\sin(\theta) + \dot{d}_G)\right] \tag{1.22'}$$

Tables 1.1 through 1.3 collect tyres, vehicle and driver data used as reference throughout the thesis work, considered fixed unless otherwise specified. Data is taken from [2].

	B	**C**	**D**	**E**
Front	14.5 rad^{-1}	1.89	9778 N	0.29
Rear	13.5 rad^{-1}	1.45	9234 N	0.31

Table 1.1: Tyres data.

Parameter	**Value**
Mass, m	1938 kg
Moment of inertia, J	4063 kg m^2
COG to Front Axle Distance, a	1.444 m
COG to Rear Axle Distance, b	1.529 m

Table 1.2: Vehicle data.

Parameter	**Value**
Proportional Gain, k_p	0.025
Derivative Gain, k_d	0.004
Preview Time, T_p	0.5 s
Delay, τ	0.2 s
Maximum Steering Angle, δ_{sat}	16.7°
Maximum Steering Angular Speed, $\dot{\delta}_{sat}$	25.7 °/s

Table 1.3: Driver data.

2 | Local Stability Analysis

The first, fundamental step when approaching the extensive topic of vehicle stability is to study the response of the system to small perturbations with respect to one equilibrium state. This is what can be defined as the *local* stability problem: the analysis concerns only one of the many equilirbia that a nonlinear system can possess, and the behaviour of the system is studied locally, i.e. in a restricted neighbourhood of the chosen equilibrium. The most used concept of stability for dissipative systems is the definition of *asymptotic stability* [1]. An equilibrium point $\boldsymbol{x} \in \mathbb{R}^n$ of an n-dimensional system is asymptotically stable if there exists a domain $G \subseteq \mathbb{R}^n$, $\boldsymbol{x} \in G$ such that all the trajectories that start inside G will come arbitrarily close to $\boldsymbol{x}$, i.e. they will eventually converge to the equilibrium.

The main result in theoretical studies on asymptotic stability is the well-known *Lyapunov theorem* [5]: the equilibrium $\boldsymbol{x}$ is locally (asymptotically) stable if and only if all the eigenvalues λ_i, $i = 1, ..., n$, of the Jacobian matrix of the system evaluated at $\boldsymbol{x}$ satisfy the condition $\Re(\lambda_i) < 0$, i.e. if all the eigenvalues have negative real part. The local stability analysis is entirely based on the Lyapunov theorem: it is not concerned with the definition of G (and in particular of its extension), but merely focuses on guaranteeing its existence. This is the biggest limitation of a local approach to the stability problem when dealing with nonlinear systems.

In this chapter, the local stability of the vehicle-and-driver models (1.29), (1.30) and of the bare vehicle (1.9) will briefly be studied, observing how the eigenvalues of the linearized systems change as function of the forward velocity u. Basic concepts and nomenclature related to nonlinear dynamical systems can be found in [5, 7]; throughout this thesis, it will be assumed that the reader is familiar with the classification of equilibrium points (nodes, foci, saddles) and with the notions of phase space, phase portrait, orbits and invariant manifolds. Since the primary focus of this thesis work is to characterize large motions of vehicle-and-driver, the results of the local stability analysis will be directly reported and commented without delving into details about the linearized model of the system, which the interested reader can find in any academic book on vehicle dynamics (e.g. [1, 3, 4, 8]).

2.1. Rectilinear Motion

The simplest (yet not at all trivial) equilibrium condition that can be defined for the vehicle, either with or without the driver control, is the straight-line motion at constant forward velocity u. The next two sections will be dedicated to studying the local stability of both systems in correspondence of this equilibrium, for different values of u.

2.1.1. Fixed Control

The straight-line motion of the bare vehicle (1.9) is identified by the state vector $\boldsymbol{z}_E = \{v_E, r_E\}^{\mathrm{T}} = \{0, 0\}^{\mathrm{T}}$, which can only be obtained if the steering angle is set to $\delta = 0$. Computing the eigenvalues of the Jacobian matrix of the system evaluated at $\boldsymbol{z}_E$ for multiple values of the forward velocity u, one can obtain the root locus pictured in Fig. 2.1a. We observe that the system always has two real eigenvalues; one of them crosses the imaginary axis as the speed is increased, thus the equilibrium becomes unstable. The *critical speed* at which this event occurs is shown in Fig. 2.1b, where the maximum real part of the eigenvalues is plotted. The analysed vehicle is oversteering at low lateral acceleration levels (see the handling curve in Fig. 1.4), and it is a well-known fact that the straight-line motion may become unstable at high speeds for vehicles that possess this characteristic. Since the imaginary part of the eigenvalues is always zero, the system never shows an oscillatory behaviour in the neighborhood of the equilibrium.

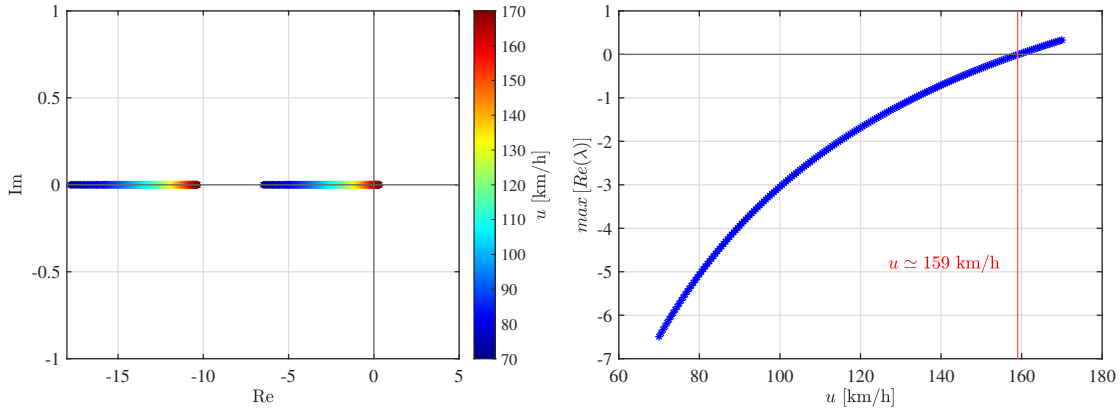

(a) Root locus. (b) Maximum real part.

Figure 2.1: Local stability analysis of the vehicle with fixed control. Rectilinear motion: eigenvalues as function of the forward velocity u.

The stability for speeds lower than the critical value, which in this case is about $u_{crit} \simeq 159$ km/h, is *local*: nothing can be stated about the magnitude of the disturbances that

the bare vehicle is able to absorb. In the same way, the linear analysis does not give any information about how the motion evolves when stability is lost: we know that the equilibrium is a stable node for $u < u_{crit}$ and becomes a saddle at higher speeds, but are there any other attractors in the phase space for $\delta = 0$? The answer will be given in Section 3.2, by means of a nonlinear analysis.

2.1.2. Driver Control

The straight-line motion of the vehicle-and-driver system is identified by the state vector $\boldsymbol{z}_E = \{v_E, r_E, \psi_E, y_{G_E}, \delta_E, \dot{\delta}_E, \ddot{\delta}_E\}^{\mathrm{T}} = \{0, 0, 0, 0, 0, 0, 0\}^{\mathrm{T}}$. The Jacobian of the system has 7 eigenvalues, which are shown in the root locus of Fig. 2.2a. We observe again that a critical velocity exists, but now the eigenvalues that cross the imaginary axis are complex conjugates. From Fig. 2.2b it can be noticed that their real part becomes positive at about $u_{crit} \simeq 124.5$ km/h, which is lower than the value observed for the bare vehicle (159 km/h). The analysis reveals that the straight line equilibrium for the vehicle-and-driver system is a stable focus for speeds up to u_{crit}, then it becomes unstable.

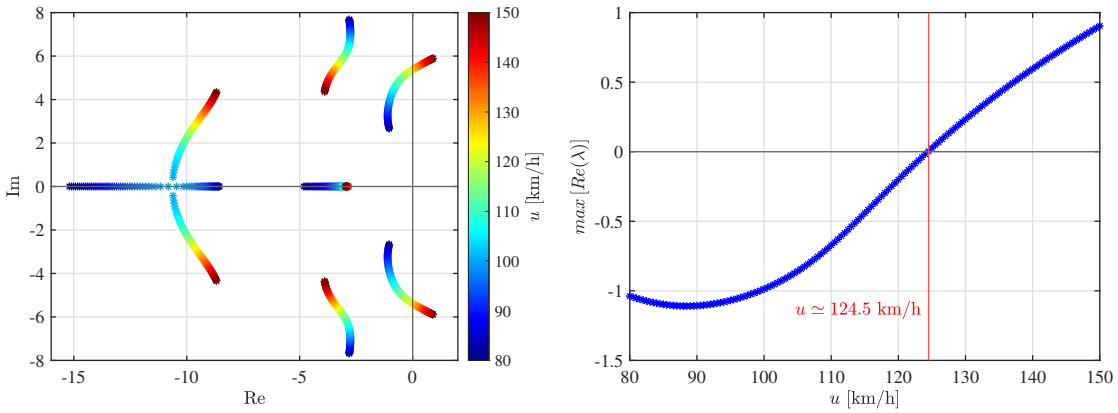

(a) Root locus. (b) Maximum real part.

Figure 2.2: Local stability analysis of the vehicle-and-driver system. Rectilinear motion: eigenvalues as function of the forward velocity u.

Once again, large motions of the system cannot be characterised with this analysis: one can only state that the system exhibits an oscillatory behaviour *in the neighbourhood* of the equilibrium.

2.2. Circular Motion

The analysis is now repeated to assess the local stability of the steady-state motion along a circular path of radius ρ. The forward speed u is still considered the main parameter to vary, while the effect of ρ will be evaluated by comparing results obtained for two discrete values.

2.2.1. Fixed Control

The input parameters of the bare vehicle (1.9) are the forward speed u and the steering angle δ: the radius of curvature of the trajectory assumed by the vehicle depends directly on the vehicle's state and can therefore only be regulated by a closed-loop controller (i.e. by the driver), which indeed acts on u and δ to maintain the desired state. Nonetheless, to compare more directly the results of the stability analysis performed on the vehicle with fixed control to those observed for the vehicle-and-driver system (in which ρ is effectively an independent parameter), it results convenient to compute the fixed steering angle input δ as function of a chosen value of ρ. Doing so requires solving the following system:

$$\begin{cases} \dot{v} = \dfrac{1}{m}(F_{y_f} + F_{y_f}) - ur = 0 \\ \dot{r} = \dfrac{1}{J}(F_{y_f}a - F_{y_f}b) = 0 \\ \rho = \dfrac{\sqrt{u^2 + v^2}}{r} \end{cases} \tag{2.1}$$

which not only gives the steering angle input necessary to run along a curve of radius ρ, but also provides the state vector $\boldsymbol{z}_E = \{v_E, r_E\}^{\mathrm{T}}$ at steady-state (system (2.1) only has one solution for $\delta < \delta_{sat}$). It is important to remark that ρ is only involved momentarily to solve the above system and by no means can be considered a fixed parameter of the bare vehicle.

The Jacobian of the system evaluated at $\boldsymbol{z}_E$ has two real eigenvalues. Figure 2.3 shows that the steady-state cornering condition for the vehicle with fixed control becomes unstable when one of the two real eigenvalues crosses the imaginary axis and becomes positive. As one would expect, tighter turns correspond to lower critical speeds: $u_{crit} \simeq 86.6$ km/h for a turn of radius $\rho = 80$ m, while $u_{crit} \simeq 103.4$ km/h for $\rho = 130$ m.

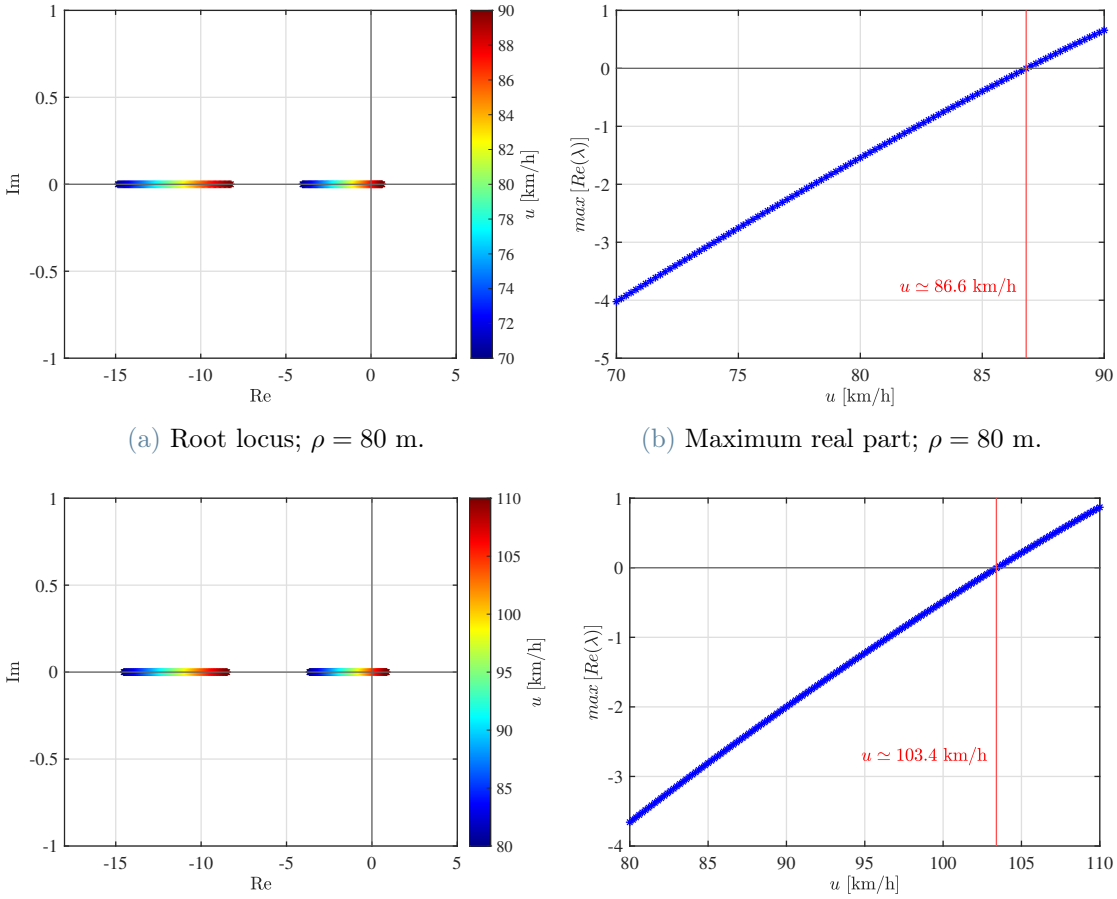

(a) Root locus; $\rho = 80$ m.

(b) Maximum real part; $\rho = 80$ m.

(c) Root locus; $\rho = 130$ m.

(d) Maximum real part; $\rho = 130$ m.

Figure 2.3: Local stability analysis of the vehicle with fixed control. Circular motion: eigenvalues as function of the forward velocity u, for turn radii of $\rho = 80$ m and $\rho = 130$ m (constant steering angle set accordingly for each condition).

2.2.2. Driver Control

Excluding non-regular driving conditions, such as powerslide and severe undesteer, the vehicle-and-driver system has only one equilibrium for every combination of (u, ρ). The state vector $\boldsymbol{z}_E = \{v_E, r_E, \psi_E, y_{G_E}, \delta_E, \dot{\delta}_E, \ddot{\delta}_E\}^{\mathrm{T}}$ at said equilibrium can be computed by solving (1.30) with $\dot{\boldsymbol{z}}_E = \boldsymbol{0}$ (obtaining $\dot{\delta}_E = \ddot{\delta}_E = 0$ is trivial). The Jacobian matrix of the system evaluated at $\boldsymbol{z}_E$ has 7 eigenvalues and, analogously to what was observed for straight line motion, the equilibrium becomes unstable as soon as one pair of complex conjugate eigenvalues crosses the imaginary axis (Figure 2.4). The critical speed is $u_{crit} \simeq 81.5$ km/h for a turn of radius $\rho = 80$ m and $u_{crit} \simeq 96.5$ km/h for $\rho = 130$ m.

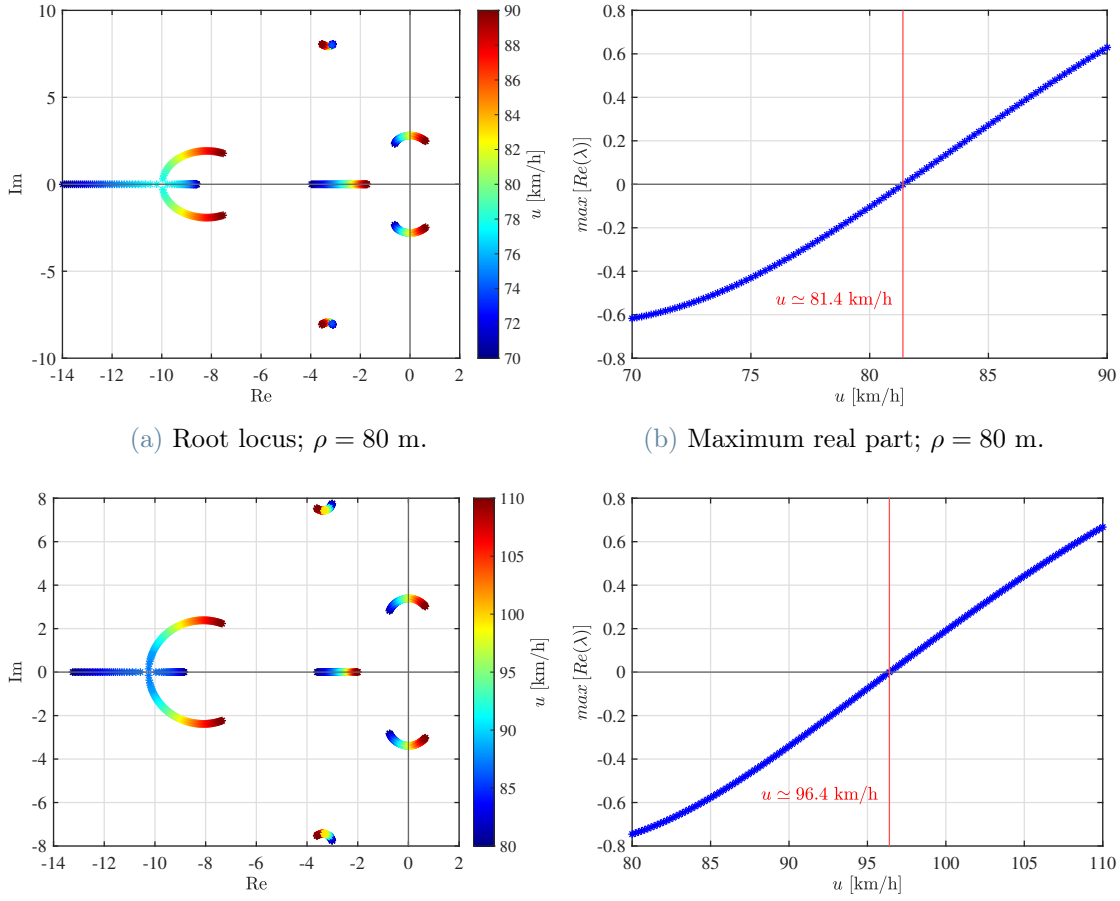

(a) Root locus; $\rho = 80$ m.

(b) Maximum real part; $\rho = 80$ m.

(c) Root locus; $\rho = 130$ m.

(d) Maximum real part; $\rho = 130$ m.

Figure 2.4: Local stability analysis of the vehicle-and-driver system. Circular motion: eigenvalues as function of the forward velocity u, for turn radii of $\rho = 80$ m and $\rho = 130$ m.

Table 2.1 below summarizes the results of the local stability analysis.

	Crit. Speed	**Equil. Type**
Straight line, w/o Driver	159 km/h	Node
Straight line, w/ Driver	124.5 km/h	Focus
Curve $\rho = 80$ m, w/o Driver	86.6 km/h	Node
Curve $\rho = 80$ m, w/ Driver	81.4 km/h	Focus
Curve $\rho = 130$ m, w/o Driver	103.4 km/h	Node
Curve $\rho = 130$ m, w/ Driver	96.4 km/h	Focus

Table 2.1: Results of local stability analysis.

3 | Bifurcation Analysis

In the previous chapter, we analysed how the local stability of an equilibrium point of the system changes in response to the variation of a parameter, namely the forward speed of the vehicle u. In essence, this assessment is part of the much more comprehensive *bifurcation analysis*, which is the study and classification of all the possible behaviours exhibited by a dynamical system as its parameters are varied. Indeed, we can initially define a *bifurcation* as a structural change in the system behaviour; this concept will be clarified in the upcoming sections.

By observation of the eigenvalues alone, a value of the forward speed (the critical speed) that makes the equilibrium unstable was found, which for a steady-state cornering condition depends on the radius of the trajectory (ρ). While only two values of ρ were considered in Sections 2.2.1 and 2.2.2, if multiple values are considered one can obtain a discretization of the curve in the (u, r)-plane formed by all the parameter combinations which make the equilibrium of the system unstable, i.e. the representation in the parameter space of (part of) the *bifurcation diagram*.

The complete bifurcation diagram is traditionally obtained employing a software which implements a *continuation* algorithm. The analysis starts by computing an equilibrium of the dynamical system; the software is then able to identify how its coordinates evolve in response to the variation of one parameter of the system, chosen by the user for the continuation, keeping all the remaining parameters fixed. During the continuation of equilibria some test functions (the *bifurcation functions*), each built to change sign at the occurrence of a specific bifurcation, are monitored. For example, it will be seen in the following that a test function may involve the eigenvalues of the linearized dynamical system, depending on the type of bifurcation that the function was designed to detect.

Each bifurcation point identified during the continuation of equilibria can in turn be selected as a starting point for the continuation software, to trace the corresponding bifurcation curve. To continue a bifurcation, the user now generally has to select more than one parameter of the system that the algorithm is free to vary; the exact number depends on the *codimension* of the bifurcation, which simply put is the number of test

functions that are necessary to detect the bifurcation. The most important bifurcations have codimension 1 or 2: dynamical systems are more likely to exhibit them since their occurrence requires the alteration of only 1 (resp. 2) of the many parameters that the system can depend upon. The continuation of a bifurcation with codimension p necessitates the simultaneous variation of $p+1$ parameters. When following the curve traced during the continuation, bifurcations with codimension $p+1$ may then be detected using specialized test functions. Generally, the analysis stops at codimension 3 bifurcations.

In this thesis work, we analyse the bifurcations of the vehicle with fixed control and of the vehicle-and-driver system up to codimension 2, which are needed to characterize the most relevant dynamical behaviours that might actually be observed in the real world. The first sections of this chapter will be dedicated to introducing the fundamental notions that are necessary to interpret the results obtained from the bifurcation analysis of road vehicle-and-driver. For a complete formal treatment on bifurcation theory and continuation techniques, the interested reader is invited to consult [5–7].

3.1. Basic Concepts

Bifurcation theory revolves around the key concept of *structural stability*. In essence, a dynamical system is structurally stable for a given combination of parameters if the phase portrait of the system does not qualitatively change under all sufficiently small perturbations of the parameters (topological equivalence). Altering the parameters of the system may cause the latter to become structurally unstable, meaning that its behaviour undergoes some structural change: a *bifurcation* occurs. Examples of such changes include the birth or disappearance of equilibria or the alteration of their stability, but it is important to remark that the concept of structural stability is not restricted to the observation of equilibrium points and is much broader than the definition of local stability introduced in Chapter 2.

The simplest way in which a system can become structurally unstable is if at least one of the eigenvalues of the Jacobian matrix computed at a given equilibrium point of the system reaches the imaginary axis of the complex plane, i.e. if an eigenvalue λ exists for which $\Re(\lambda) = 0$. This is exactly what was observed by performing the local stability analysis: equilibria of the bare vehicle become unstable when $\lambda = 0$, those of the vehicle-and-driver system instead lose stability when there is a pair of complex conjugate eigenvalues $\lambda_{1,2} = \pm i\omega_0$ ($\omega_0 \in \mathbb{R}^+$) on the imaginary axis. In both cases, the bifurcation is *local*: the behaviour of the system changes in a restricted neighbourhood of the equilibrium point (and indeed, the bifurcation can be detected by monitoring the eigenvalues).

Among the possible local bifurcations observed in dynamical systems, in the following we describe the *Hopf* bifurcation (codim. 1) and the *Bautin* bifurcation (codim. 2), which are the most relevant for the vehicle-and-driver model under analysis. We anticipate that the bare vehicle considered in this work also undergoes a *saddle-node* bifurcation (codim. 1) and a *Homoclinic* bifurcation (i.e. a *Global* bifurcation, which involves a much more extensive region of the phase space). Since the present thesis is mainly focused on characterizing the behaviour of vehicle-and-driver, these bifurcations will not be described in this introductory section; they are thoroughly addressed in [5] and more concisely in the appendix of [11], which the unfamiliar reader is invited to consult. The sofware utilized in this work to perform bifurcation analysis is MatCont [28, 29], a continuation toolbox developed in the MATLAB environment.

3.1.1. Hopf Bifurcation and Limit Cycles

Let us consider an n-dimensional dynamical system ($n \geq 2$) which depends on at least one parameter $\alpha \in \mathbb{R}$ and that has at $\alpha = \alpha_H$ an equilibrium point $\bar{\boldsymbol{z}}_H$. Assume that for all sufficiently small perturbations $|\alpha - \alpha_H|$ the position of said equilibrium point in the phase space can be described by the state vector $\boldsymbol{z}_H(\alpha) \in \mathbb{R}^n$, $\boldsymbol{z}_H(\alpha_H) = \bar{\boldsymbol{z}}_H$, and that the Jacobian matrix computed at the equilibrium has one pair of complex conjugate eigenvalues

$$\lambda_{1,2} = \mu(\alpha) + i\omega(\alpha)$$

that become purely imaginary when $\alpha = \alpha_H$, i.e. $\mu(\alpha_H) = 0$ and $\omega(\alpha_H) = \omega_0 > 0$. Then, if the following *nondegeneracy* conditions hold:

$$\begin{cases} l_1(\alpha_H) \neq 0 & \text{(3.1a)} \\ \dfrac{d\mu(\alpha_H)}{d\alpha} \neq 0 & \text{(3.1b)} \end{cases}$$

the system undergoes a *Hopf* bifurcation at $\alpha = \alpha_H$.

The coefficient $l_1(\alpha_H)$ in Eq. (3.1a) is the *first Lyapunov coefficient*; it can be computed starting from a third-order Taylor expansion of the system and performing a nonlinear coordinate transformation to express the equations into the Hopf normal form [5]. The *normal form* of a local bifurcation is a system that is locally topologically equivalent to the main system under analysis, near the equilibrium that undergoes the bifurcation. In essence, it contains all the necessary information to study the bifurcation while still being much more manageable in terms of complexity with respect to the main system.

The only Hopf bifurcation condition is $\mu(\alpha_H) = 0$, which can be met by altering one parameter of the system: the Hopf bifurcation has codimension 1 and can be detected during continuation of equilibria. The inequalities (3.1) are necessary to allow the representation of the system in the Hopf normal form. (3.1b) is also called *transversality* condition and is needed to guarantee that the eigenvalues effectively cross the imaginary axis.

If the equilibrium $\boldsymbol{z}_H(\alpha)$ is locally stable for $\alpha < \alpha_H$, then it becomes unstable after the bifurcation occurs, i.e. for $\alpha > \alpha_H$ (or viceversa). Moreover, since $\omega(\alpha) > 0$ for small perturbations around α_H, we can affirm that the equilibrium affected by the bifurcation is a focus. These results can also be obtained with a simple linear analysis (see for example Sections 2.1.2 and 2.2.2). What cannot be inferred if the analysis is restricted to the linearized system is instead the stability of $\boldsymbol{z}_H(\alpha_H)$, because the Lyapunov theorem (Chapter 2) is only valid for hyperbolic equilibrium points, i.e. equilibria which correspond to eigenvalues with non-zero real part (nodes, saddles and foci).

Reducing the system to the Hopf normal form, thus considering the third-order Taylor expansion of the system rather than its linear component only, it can be shown that the equilibrium $\boldsymbol{z}_H(\alpha_H)$ is stable (resp. unstable) if and only if $l_1(\alpha_H) < 0$ (resp. $l_1(\alpha_H) > 0$). The stability is *nonlinear*: the rate of convergence (resp. divergence) is not exponential, unlike what is observed for hyperbolic equilibria; sometimes $\boldsymbol{z}_H(\alpha_H)$ is called a weakly attracting (resp. repelling) focus. We can then distinguish two types of Hopf bifurcation, based on the stability of $\boldsymbol{z}_H(\alpha_H)$: if $l_1(\alpha_H) < 0$, a *supercritical* Hopf bifurcation occurs; if instead $l_1(\alpha_H) > 0$, the bifurcation is *subcritical*.

The normal form of the Hopf bifurcation expressed in polar coordinates unveils the presence of a closed, isolated orbit in the proximity of the equilibrium point that undergoes the bifurcation. In correspondence of this solution, the system exhibits self-sustained periodic oscillations of constant amplitude. The closed orbit is *isolated*, in the sense that it is sufficiently far from trajectories of the same type. A closed orbit which meets this requirement is called *limit cycle*. Analogously to equilibrium points, limit cycles can be classified based on their stability, which can be studied by linearizing the equations of motion of the system in the neighbourhood of the cycle. Trajectories near a stable limit cycle, by definition, are attracted to the cycle, while trajectories close to an unstable cycle are repelled by it. Saddle-type limit cycles should be distinguished among unstable cycles: nearby trajectories move towards the cycle along certain directions and then move away from it along other directions. The stability analysis of limit cycles and the characterization of motions along nearby orbits will be argument of Chapter 6.

An unstable limit cycle originates from a subcritical Hopf bifurcation (or equivalently it

shrinks on it, depending on the chosen direction of parameter variation), and exists when the equilibrium $\boldsymbol{z}_H(\alpha)$ is stable; a stable limit cycle instead generates from a supercritical Hopf bifurcation, and exists when the equilibrium $\boldsymbol{z}_H(\alpha)$ is unstable. The amplitude of the cycle generally increases as the bifurcation parameter (α) is varied and the system operates away from the bifurcation, as shown in Fig. 3.1 for a second-order system.

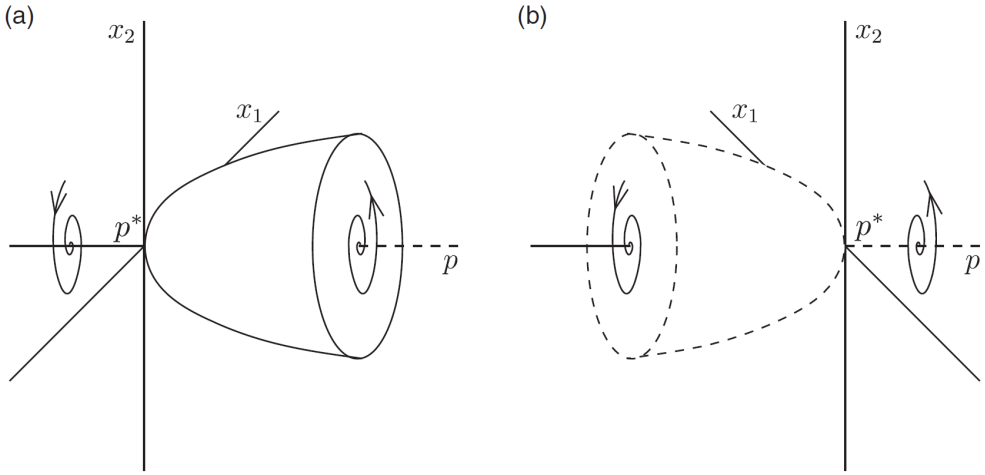

Figure 3.1: (a) Super- and (b) sub-critical Hopf bifurcations in second-order systems. Reproduced from [11].

The loss of stability of the equilibrium $\boldsymbol{z}_H(\alpha)$ caused by a subcritical hopf bifurcation is defined *catastrophic*: the system departs from the neighbourhood of the equilibrium as soon as the bifurcation parameter crosses the critical value, since no attractors are present in the immediate proximity of $\boldsymbol{z}_H(\alpha)$. In practice, this means that even if the parameter is reset to a value which would normally correspond to local stability of the equilibrium, it is not guaranteed that stability will be recovered, since the state of the system may already be excessively far from the equilibrium. If $\boldsymbol{z}_H(\alpha)$ loses stability through a supercritical Hopf bifurcation, the event is defined *non-catastrophic*, since the stable limit cycle keeps the system close to the equilibrium. It should then be clear that from a safety standpoint a subcritical bifurcation is much more dangerous. In Section 3.3, it will be seen that the Hopf bifurcation is the mechanism that leads to the loss of stability of equilibria of the vehicle-and-driver system.

3.1.2. Bautin Bifurcation

Let us now consider an n-dimensional dynamical system ($n \geq 2$) which depends on at least two parameters, collected in the vector $\boldsymbol{\alpha} \in \mathbb{R}^2$, and that has at $\boldsymbol{\alpha} = \boldsymbol{\alpha}_H$ an equilibrium

point $\bar{\boldsymbol{z}}_H$. Assume that for all sufficiently small perturbations $\|\boldsymbol{\alpha} - \boldsymbol{\alpha_H}\|$ the position of said equilibrium point in the phase space can be described by the state vector $\boldsymbol{z}_H(\boldsymbol{\alpha}) \in \mathbb{R}^n$ ($\boldsymbol{z}_H(\boldsymbol{\alpha}_H) = \bar{\boldsymbol{z}}_H$), and that the Jacobian matrix computed at the equilibrium has one pair of complex conjugate eigenvalues

$$\lambda_{1,2} = \mu(\boldsymbol{\alpha}) + i\omega(\boldsymbol{\alpha})$$

that become purely imaginary when $\boldsymbol{\alpha} = \boldsymbol{\alpha}_H$, i.e. $\mu(\boldsymbol{\alpha}_H) = 0$ and $\omega(\boldsymbol{\alpha}_H) = \omega_0 > 0$. Further assume that, under the same condition, the first Lyapunov coefficient vanishes: $l_1(\boldsymbol{\alpha}_H) = 0$. Then, if the following nondegeneracy conditions hold:

$$\begin{cases} l_2(\boldsymbol{\alpha}_H) \neq 0 \\ \text{the map } \alpha \mapsto (\mu(\boldsymbol{\alpha}),\ l_1(\boldsymbol{\alpha})) \text{ is regular at } \boldsymbol{\alpha} = \boldsymbol{\alpha}_H \end{cases} \tag{3.2a}$$

the system undergoes a *Bautin* bifurcation (or *generalized Hopf* bifurcation) at $\boldsymbol{\alpha} = \boldsymbol{\alpha}_H$.

The Bautin bifurcation represents the switch from a catastrophic stability loss ($l_1(\boldsymbol{\alpha}_H) > 0$) to a non-catastrophic one ($l_1(\boldsymbol{\alpha}_H) < 0$) or viceversa, and is therefore quite meaningful for road vehicles. It can be detected during the continuation of a Hopf bifurcation, i.e. by freeing an additional system parameter (codimension 2 bifurcation); indeed, $l_1(\boldsymbol{\alpha}_H) = 0$ is a supplementary bifurcation condition. The same condition also implies that the Bautin bifurcation cannot be detected by merely monitoring the eigenvalues, as a third-order Taylor expansion of the system is needed to compute the first Lyapunov coefficient. $l_2(\boldsymbol{\alpha}_H)$ in Eq. (3.2a) is the *second Lyapunov coefficient*, whose evaluation requires instead a fifth-order Taylor expansion of the equations of motion [5].

3.2. Bifurcations of the Vehicle Model

After a brief overview of the main concepts related to bifurcation theory, we initially perform the bifurcation analysis of the vehicle model with fixed control, varying the longitudinal speed u and the steering angle δ. Parameters related to the vehicle and tyres are considered fixed to their reference values, listed in Tables 1.2 and 1.1, as their effect on vehicle dynamics will not be investigated in the present work. A broad classification of instability modes for various vehicle typologies, distinguished on the basis of tyre characteristics and with fixed control, is available in [11]. The analysis will be conducted considering the simple single-track vehicle model (1.9).

Continuation of equilibria is the first phase of the study. In this case, we select the steering

angle δ as the continuation parameter and fix the forward speed to $u = 30$ km/h. The equilibrium curve (Fig. 3.2a) can be obtained starting from a known equilibrium point: the most trivial choice is to start from the steady-state motion along a rectilinear path, although in principle any point on the handling diagram is adequate for the scope. As one would expect (see the handling curve in Fig. 1.4), the vehicle has multiple equilibrium points for the same value of δ.

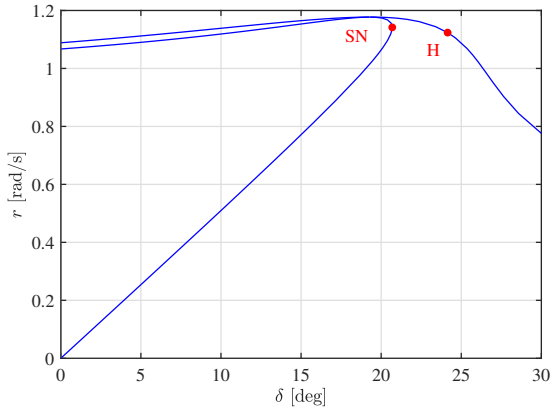

(a) Equilibrium curve ($u = 30$ km/h).

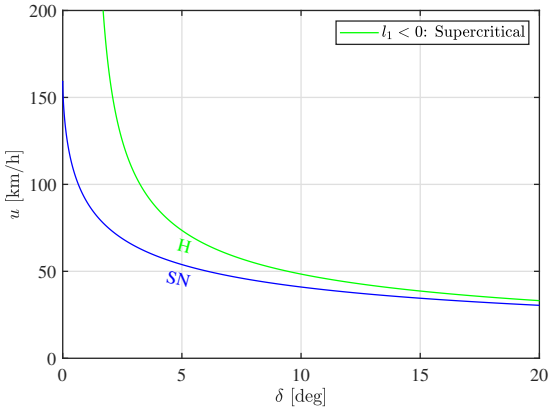

(b) Supercritical Hopf (H) and Saddle-Node (SN) bifurcation curves.

Figure 3.2: Vehicle with fixed control: bifurcations of equilibria.

Along the equilibrium curve, a supercritical Hopf bifurcation (label "H" in Fig. 3.2a) and a saddle-node bifurcation (label "SN") are detected. Both bifurcation can be continued in the (δ, u)-plane, obtaining the corresponding curves visualized in Fig. 3.2b. We can now select a point on the supercritical Hopf curve and start the continuation of stable limit cycles, by varying for example the forward speed u; in this case, a steering angle $\delta = 5°$ is chosen, for which the Hopf bifurcation occurs at $u \simeq 73.5$ km/h. Observing Fig. 3.3a, one can notice that the cycle starts to assume a teardrop-like shape as the speed decreases, which is typical of homoclinic orbits that depart from - and return to - the same saddle equilibrium. Indeed, Fig. 3.3b shows that the period of the limit cycle drastically increases at about $u \simeq 50.8$ km/h, signaling the occurrence of a homoclinic bifurcation for nearby values of the parameters. The last cycle of the family can be selected to start the continuation of the homoclinic bifurcation and to compute the corresponding curve in the (δ, u)-plane, thus completing the bifurcation diagram of the bare vehicle (Fig. 3.4).

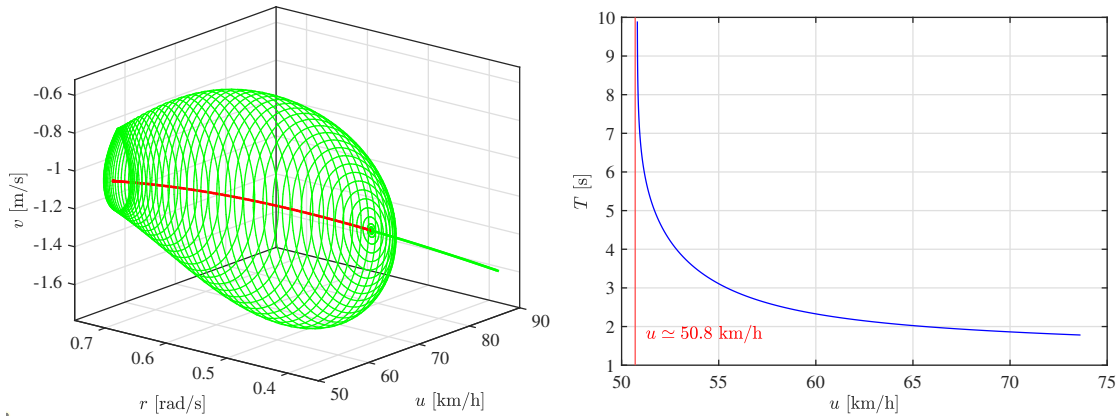

(a) Family of u-parametrized cycles. (b) Period of the cycles.

Figure 3.3: Vehicle with fixed control: continuation of stable limit cycles from the Hopf bifurcation at $(u, \delta) = (73.5 \text{ km/h}, 5°)$. The thick line in (a) indicates the equilibrium affected by the bifurcation (red: unstable equilibrium, green: stable equilibrium). The sharp increase of the cycle period at $u \simeq 50.8$ km/h and the teardrop shape of the cycle signal the occurrence of a homoclinic bifurcation.

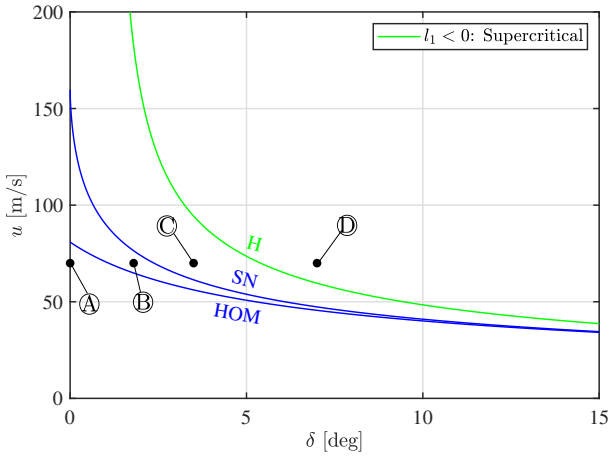

Figure 3.4: Vehicle with fixed control: complete bifurcation diagram. H: supercritical Hopf bifurcation; SN: Saddle-Node bifurcation; HOM: homoclinic bifurcation. The vehicle exhibits 4 different types of dynamical behaviours (from Ⓐ to Ⓓ). The corresponding phase portraits are illustrated in Fig. 3.5.

The analysis is finalized with the representation of the trajectories of the dynamical system in the phase plane for parameter combinations (δ, u) selected in distinct regions of the bifurcation diagram, delimited by the bifurcation curves obtained earlier. Referring to Fig. 3.4, we distinguish 4 unique types of dynamical behaviours that the vehicle can exhibit; the corresponding phase portraits are visible in Fig. 3.5:

- Case Ⓐ; the system has five equilibria: one stable node (e_1), two saddles (e_2, e_3) and two unstable foci (e_4, e_5). All the trajectories in the phase plane ultimately converge to the only stable equilibrium: e_1 is *globally* stable, i.e. the system is able to absorb perturbations of any amplitude;
- Case Ⓑ; the local stability of each equilibria remains unchanged, but a stable limit cycle originates from the homoclinic bifuration and surrounds e_4. The stable node (e_1) is still *locally* stable, but *global* stability is lost: trajectories contained in the gray region of the phase portrait (bounded by the stable manifold of the saddle e_2) are attracted to the cycle instead of eventually converging to the node. We define this region as the *basin of attraction* of the stable cycle, while its complement is the basin of the attraction of e_1;
- Case Ⓒ; The saddle e_2 and the node e_1 collide and disappear at the saddle-node bifurcation: the system now has no stable equilibrium points, and all trajectories are attracted to the stable limit cycle. At the saddle-node bifurcation, one eigenvalue of the Jacobian matrix of the system evaluated at e_1 becomes null: this was already observed in Sections 2.1.1 and 2.2.1;
- Case Ⓓ; the stable limit cycle progressively shrinks on e_4 and disappars as the latter undergoes a supercritical Hopf bifurcation. All the trajectories in the phase plane converge to e_4, which has become a globally stable focus. Observing the handling diagram, one can notice that only the front axle is saturated in this condition.

It should be noted that even when an equilibrium is globally stable, some trajectories might explore regions of the phase plane that are far outside what would be considered safe operating conditions on road. Regardless, the concept of global stability is extremely important because it considerably enlarges the classical definition of local stability, which instead concerns only small perturbations in a restricted neighbourhood of the equilibrium. While a more in-depth treatment of global stability is reserved to the next chapters of this thesis, it should already be evident from the bifurcation analysis of the bare vehicle that this kind of analysis is the only viable option to capture a wide range of dynamic behaviours exhibited by the vehicle, that would otherwise be missed were the study only focused on observing the eigenvalues of the linearized system.

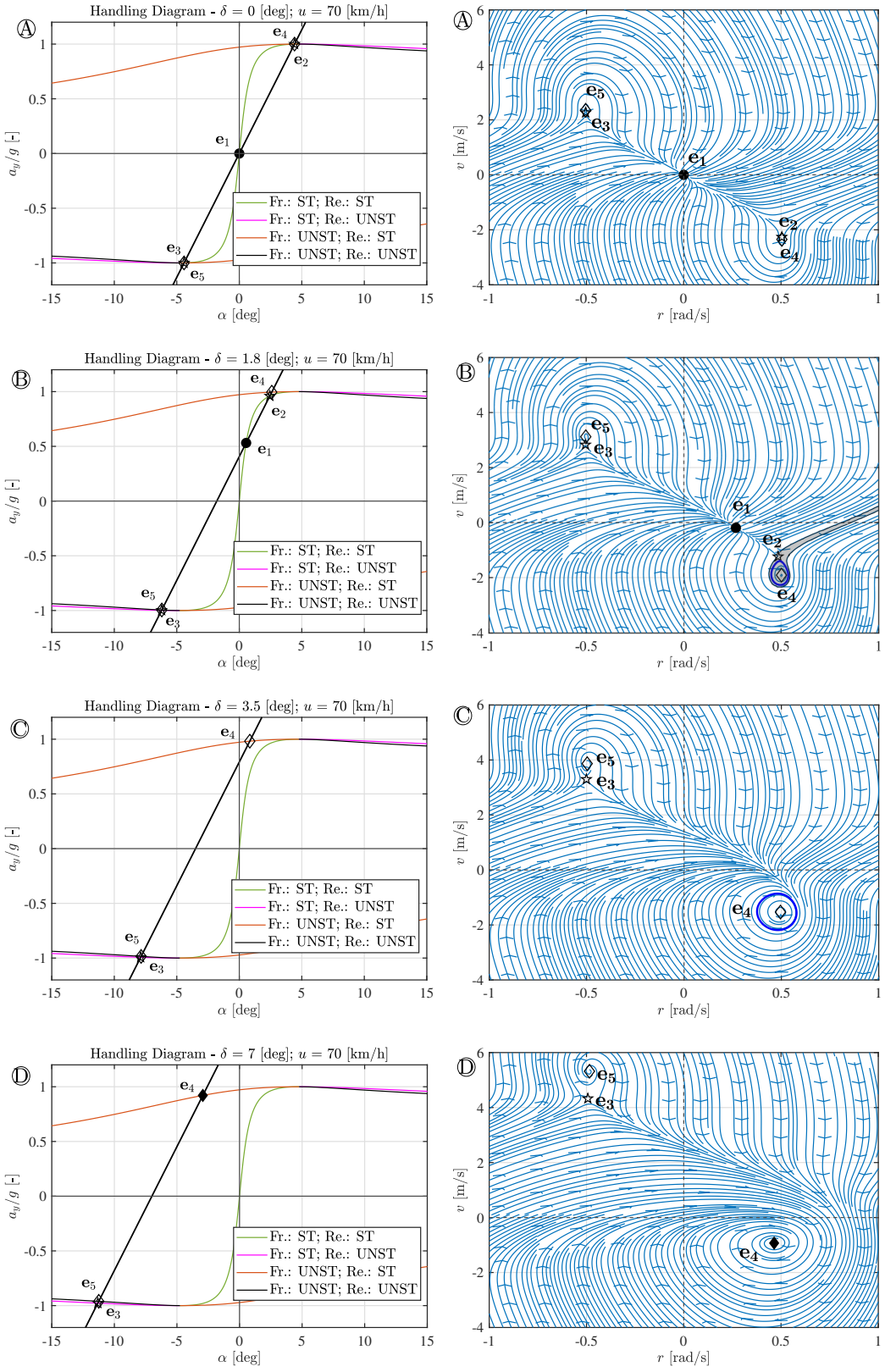

Figure 3.5: Vehicle with fixed control: phase portraits for different input parameters (u, δ). Alphabetical labels refer to Fig. 3.4.

3.3. Bifurcations of the Vehicle-and-Driver Model

Now that the wide range of behaviours exhibited by the vehicle with fixed control has been explored, it is time to effectively introduce the control action of the driver and repeat the analysis to assess how this coupling affects the dynamics of the system and in particular its stability. In the following sections, the bifurcations of the 7 DoF vehicle-and-driver model will be analysed considering initially a reference straight path (1.29) and subsequently the motion along a circular trajectory (1.30). Nonlinear behaviours will be characterized by varying:

- The forward speed of the vehicle u;
- The curve radius ρ
- The steering actuation delay τ;
- The proportional and derivative gains k_p, k_d (only in the case of rectilinear motion).

Parameters related to the tyres and vehicle are again considered fixed to their reference values (Tables 1.1 and 1.2); their effect on the dynamics of a 5DoF vehicle-and-driver system was investigated in [15], considering a first-order approximation of the delayed steering dynamics; analogous studies on more complex systems (7 DoF and up) are currently lacking: this gap should be addressed in future researches.

3.3.1. Rectilinear Motion

In this section, bifurcation analysis is performed on the vehicle-and-driver system considering the motion along a rectilinear path (1.29), which is an extremely significant starting point to formally describe highly nonlinear behaviours typically observed on road. As usual, the analysis starts with the continuation of equilibria. In this case, it should be easy to understand that the unique equilibrium possessed by the system does not change its location in the phase space when the parameters are varied: after a disturbance has acted, the driver will control the steering wheel in an attempt to return to the original rectilinear path, and the only state vector compatible with this steady-state solution is $\boldsymbol{z}_E = \{v_E, r_E, \psi_E, y_{G_E}, \delta_E, \dot{\delta}_E, \ddot{\delta}_E\}^{\mathrm{T}} = \{0, 0, 0, 0, 0, 0, 0\}^{\mathrm{T}}$. Performing the continuation by selecting the forward speed u as the only free parameter, a subcritical Hopf bifurcation is detected at $u = 124.4$ km/h, through which $\boldsymbol{z}_E$ loses stability.

The existence of a critical speed for the motion of vehicle and driver along a straight path was already observed in Sect. 2.1.2, but the current analysis unveils that the bifurcation is *subcritical* (the first Lyapunov coefficient is automatically computed by the continuation

software). Therefore, we can conclude that the loss of stability is *catastrophic*: for speeds higher than the critical value, the perturbed system exhibits oscillations of increasing amplitude until the vehicle spins as soon as the rear axle reaches the traction limit, regardless of the amplitude of the initial disturbance.

Perhaps more relevant is observing the behaviour of the system before the equilibrium becomes unstable. Since the bifurcation is subcritical, we can state that an unstable limit cycle exists when the equilibrium is still locally stable. The family of u-parametrized unstable limit cycles obtained by continuation from the Hopf bifurcation is visualized in Fig. 3.6. The cycle is of the saddle type: in general, for a given initial state located in a region of the phase space sufficiently close to the cycle, the motion of the system evolves along an orbit which gets closer to the cycle, completes one or more oscillations and eventually starts to move away from the periodic solution. It will be seen in Chapter 4 that not all orbits that depart from the cycle converge to the equilibrium: the latter is *locally* - but not *globally* - stable due to the underlying presence of the saddle-type limit cycle. The procedure to actually assess the stability of a limit cycle will be given in Chapter 6.

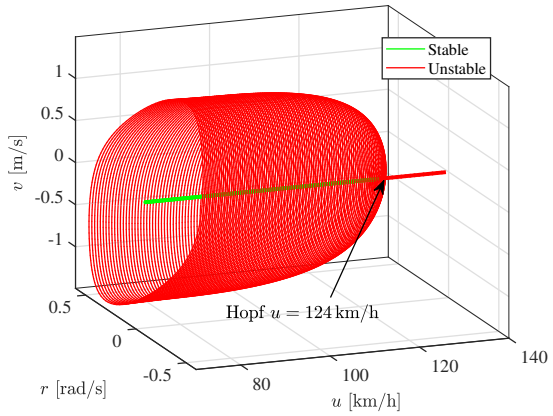

Figure 3.6: Vehicle-and-driver system, rectilinear motion: u-parametrized family of saddle-type limit cycles projected on the (v, r)-plane. At the Hopf bifurcation ($u = 124.4$ km/h), the cycle shrinks on the equilibrium (thick line), which loses stability (green: stable equilibrium, red: unstable equilibrium).

The analysis reveals that the mechanism causing equilibria of the vehicle-and-driver system to become unstable differs significantly from the behavior observed when driver control is absent. Even large motions before the actual loss of stability are noticeably dissimilar (see cases Ⓐ and Ⓑ in Fig. 3.5). It is clear that the driver plays a major role in characterizing the behaviour of the system, and the effect of the control parameters that regulate the steering action should be investigated.

Effect of Control Gains

To assess how the behaviour of the vehicle-and-driver system transforms as the steering control parameters are varied, the Hopf bifurcation is initially continued in the (u, k_p)-plane for three discrete values of k_d. The resulting curves are visible in 3.7a; the equilibrium is locally stable for parameters selected in the leftmost region of the plane and becomes unstable when the Hopf curve is crossed from left to right. Increasing the proportional gain leads to a reduction of the critical velocity: a driver whose steering response is more aggressive for the same value of the path error tends to destabilize the vehicle, as the rear axle of the vehicle has to sustain higher peak yaw moments. The effect of k_d is instead shown in 3.7b. For each value of k_p, there exists a value of k_d which maximizes the critical speed.

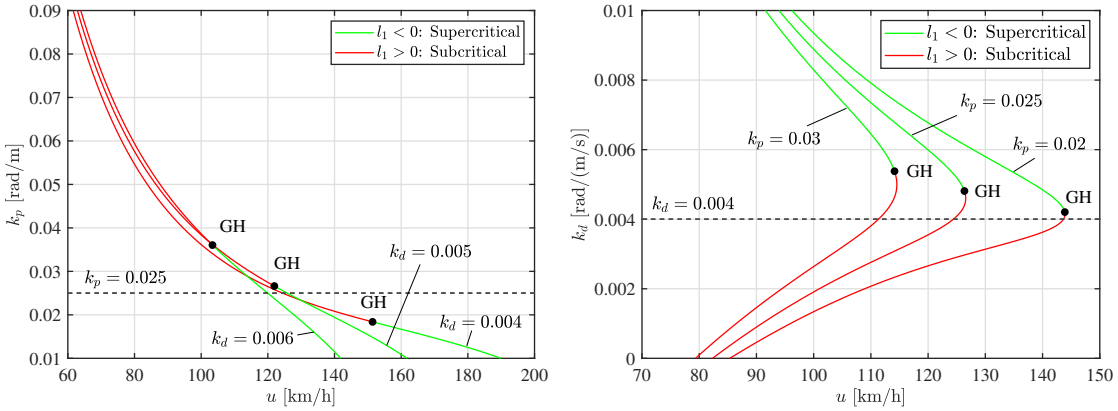

(a) Continuation in the (u, k_p)-plane.

(b) Continuation in the (u, k_d)-plane.

Figure 3.7: Vehicle-and-driver system, rectilinear motion: effect of the driver PD-control gains on the Hopf bifurcation curve. Gains of the reference driver: $k_p = 0.025$, $k_d = 0.004$. The equilibrium becomes unstable as the forward speed u is increased, i.e. crossing the Hopf curve from left to right. The green branch of each curve indicates a non-catastrophic event, with the consequent birth of stable limit cycles; the red branch indicates a catastrophic event which generates unstable limit cycles (as in Fig. 3.6). The Bautin bifurcation (GH) separates the two behaviours.

Following the Hopf curve, we notice that a Bautin bifurcation has been detected during continuation, indicating the switch from a subcritical to a supercritical bifurcation or viceversa. In this case, the loss of stability becomes non-catastrophic for lower values of k_p (Fig. 3.7a), or equivalently for higher values of k_d (Fig. 3.7b). For example, fixing the value of the proportional gain to the reference value $k_p = 0.025$ and increasing the derivative gain up to about $k_d \simeq 0.005$ (the reference value is $k_d = 0.004$), the equilibrium of the

system becomes unstable through a non-catastrophic event, at a slightly increased critical speed of $u \simeq 125.8$ km/h. For $k_d > 0.005$ the Hopf bifurcation remains supercritical, but occurs at lower speeds (see Fig. 3.7b).

The u-parametrized family of stable limit cycles generated from the supercritical Hopf bifurcation, considering $(k_p, k_d) = (0.025, 0.005)$, is shown in Fig. 3.8a. A fold bifurcation of limit cycles in correspondence of which a stable cycle collides with an unstable cycle occurs at a forward speed $u \simeq 126$ km/h, that is only slightly higher than the critical value. Therefore, an unstable limit cycle still exists when the equilibrium of the system is locally stable, even if the Hopf bifurcation is supercritical. In any case, the amplitude of the unstable cycle is considerably higher than what is observed for the subcritical case (at least at high speeds); as a result, it becomes a relevant feature of the motion of the system only for severe perturbations. At the same time, obtaining a motion influenced by the stable cycle would be quite difficult, since the latter exists only for an extremely limited speed range. Increasing the derivative gain to $k_d = 0.006$, the Hopf bifurcation occurs at $u \simeq 120$ km/h, further away from the Bautin bifurcation: the fold bifurcation of cycles is pushed to a higher speed ($u \simeq 128$ km/h) and the stable cycle acquires greater relevance since it persists for a wider speed range, as visible in Fig. 3.8b.

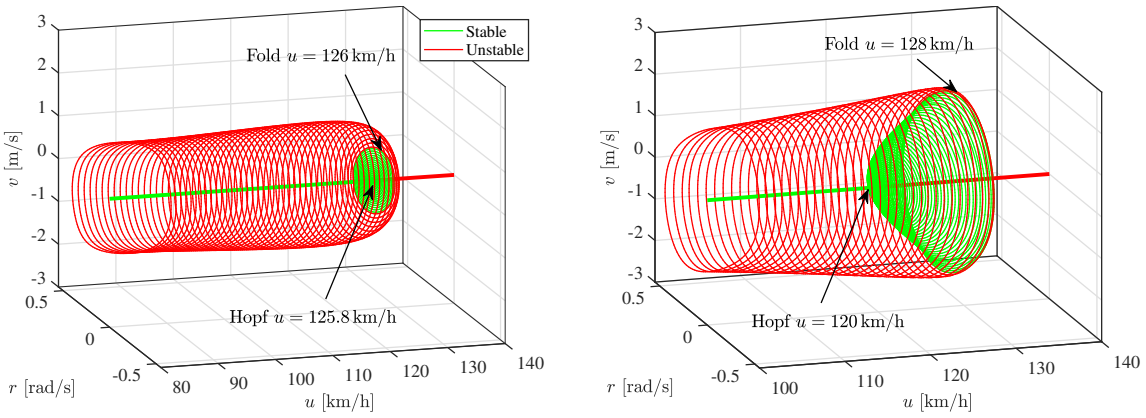

(a) $k_d = 0.005$. (b) $k_d = 0.006$.

Figure 3.8: Vehicle-and-driver system, rectilinear motion: u-parametrized family of limit cycles generated from a supercritical Hopf bifurcation (green: stable cycles), for two values of k_d (fixed $k_p = 0.025$). Projections on the (v, r)-plane. In both cases, a fold bifurcation of cycles occurs: a saddle-type cycle (in red) still exists when the equilibrium is stable, although it has high amplitude. At $k_d = 0.005$ the stable cycle is present only for a very limited speed range.

It must be remarked that the above results are specific to the considered vehicle and the effect of the control parameters on the behaviour of the system does vary if the analysis is repeated on a vehicle with different tyre characteristics (see for example [15]).

Effect of Steering Delay

The continuation of the Hopf bifurcation in the $(u,\ k_p)$-plane is now performed for different values of steering actuation delay τ. Results are shown in Fig. 3.9. A substantial increase of the critical speed is obtained by halving the delay from 0.2 s to 0.1 s, and the bifurcation becomes supercritical for every reasonable combination of k_p and k_d (a Bautin bifurcation still occurs at high values of k_p). Further reducing the delay pushes the Hopf bifurcation above the maximum speed of the vehicle, so that the system is stable at whichever speed considered. Moreover, due to the absence of low amplitude saddle-type limit cycles, the equilibrium condition is recovered even if the state of the system is severely perturbed (within reasonable limits). If $\tau = 0$, the hopf bifurcation vanishes: the delay τ of the driver is the primary cause of the generation of the limit cycle.

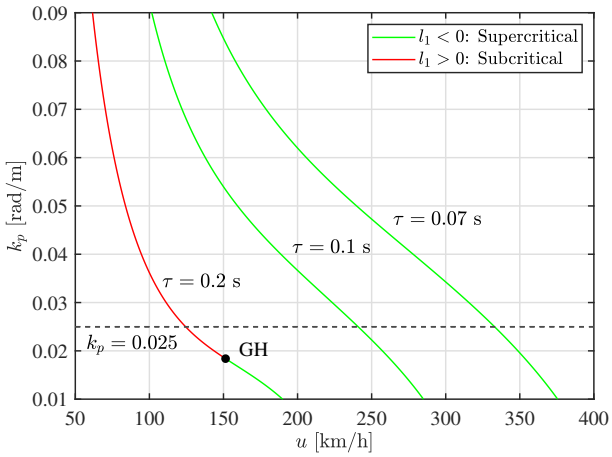

Figure 3.9: Vehicle-and-driver system, rectilinear motion: effect of the steering delay τ on the Hopf bifurcation curve. The Hopf bifurcation vanishes if the steering request is met by the driver without any delay.

3.3.2. Circular Motion

The bifurcation analysis is now repeated considering the motion along a circular path (1.30). To the author's knowledge, there are no other works in literature in which bifurcation theory is applied to mathematically describe the nonlinear behaviour of the cornering vehicle with driver control, probably because the importance of such analysis has not been realized yet.

Excluding non-regular driving conditions, such as powerslide (motion at large vehicle slip angle, described in [10]) and severe undesteer, which are in any case not accurately described by the model utilized in this work, the vehicle-and-driver system has only one equilibrium for every combination of (u, ρ). The other steady-state cornering conditions mentioned are located far from the region of the phase space that is of interest for the present analysis, so they can be disregarded. The equilibrium curve obtained using the corner radius ρ as free parameter for the continuation, with the forward speed fixed at $u = 100$ km/h, is pictured in Fig. 3.10a.

Along the equilibrium curve a subcritical Hopf bifurcation is detected, at $\rho = 145.6$ m for the considered forward speed. This was to be expected, since in essence the rectilinear motion previously analysed is equivalent to driving along a reference trajectory of infinite radius of curvature. The Hopf bifurcation can be continued in the (u, ρ)-plane; the resulting curves for different values of steering delay τ are visible in Fig. 3.10b. No Bautin bifurcations were observed in this case: the Hopf bifurcation remains subcritical. As suggested, following the curve obtained for $\tau = 0.2$ s it is possible to notice that the critical speed gets arbitrarily close to the value observed for straight-line motion ($u = 124.4$ km/h) as ρ increases.

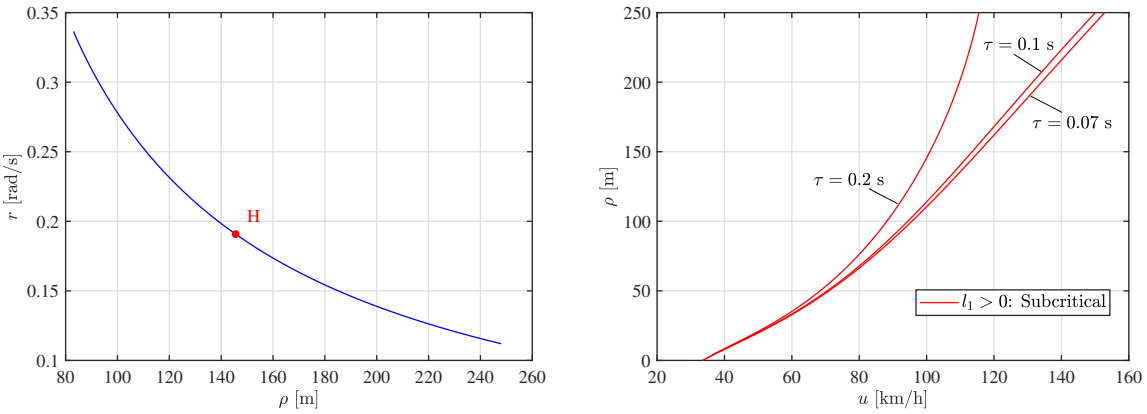

(a) Equilibrium curve ($u = 100$ km/h). H: subcritical Hopf bifurcation.

(b) Subcritical Hopf curve, for different values of steering delay τ.

Figure 3.10: Vehicle-and-driver system, circular motion: bifurcation diagram.

If the steering delay is decreased, the critical speed increases for any given value of ρ, but the improvement becomes marginal as the delay is further reduced. Variations of τ are also observed to have less impact for lower values of ρ. In practice, it is not possible to avoid the loss of stability of the equilibrium, meaning that in this case the onset of unstable behaviour might be predominantly determined by the oversteering character of

the vehicle (although the mechanism through which stability is lost is still typical of the driver). Analogously to the straight-line case, the Hopf bifurcation is subcritical and therefore an unstable limit cycle exists when the equilibrium is still locally stable. Fig. 3.11 illustrates the u-parametrized families of cycles obtained for $\rho = 80$ m and for $\rho = 130$ m. Also in this case, it can be demonstrated (Chapter 6) that the limit cycles are of the saddle-type.

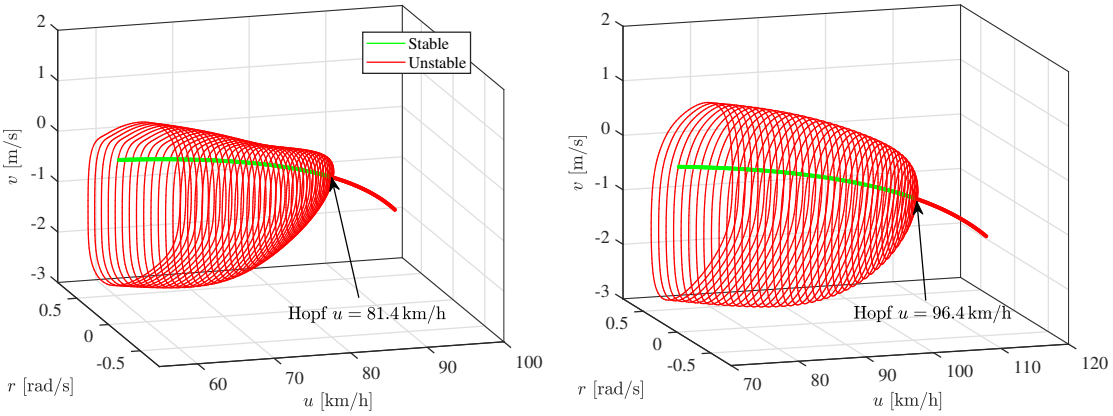

(a) $\rho = 80$ m. (b) $\rho = 130$ m.

Figure 3.11: Vehicle-and-driver system, circular motion: u-parametrized family of saddle-type limit cycles generated from the subcritical Hopf bifurcation. Projections on the (v, r)-plane. The thick line indicates the equilibrium affected by the bifurcation (red: unstable equilibrium, green: stable equilibrium).

4 | Global Stability of the Vehicle-and-Driver System

In the previous chapter, bifurcation theory was exploited to mathematically describe highly nonlinear behaviours exhibited by the vehicle, with and without driver control. In particular, regions of attraction of stable limit cycles and equilibria were discovered in the phase portrait of the bare vehicle, by qualitatively observing whether trajectories converged to one attractor in particular. This was possible only because the system is two-dimensional, thus orbits can conveniently be represented on a plane. In any case, it is clear that the exact basins of attraction should be computed mathematically.

The *basin of attraction* $G(\bar{\boldsymbol{z}}) \subseteq \mathbb{R}^n$ of a stable equilibrium $\bar{\boldsymbol{z}} \in \mathbb{R}^n$ is the set of all initial states $\boldsymbol{z}(0) \in \mathbb{R}^n$ from which trajectories eventually converge to $\bar{\boldsymbol{z}}$, i.e. [11]

$$B(\bar{\boldsymbol{z}}) = \left\{ \boldsymbol{z}(0) | \lim_{t \to \infty} \boldsymbol{z}(t) = \bar{\boldsymbol{z}} \right\}$$

The equilibrium $\bar{\boldsymbol{z}}$ is globally stable if $G(\bar{\boldsymbol{z}}) = \mathbb{R}^n$ (with the exception of isolated points and/or lines). More tangibly, $\bar{\boldsymbol{z}}$ could be considered globally stable if $G(\bar{\boldsymbol{z}})$ sufficiently encompasses all operational conditions realistically encountered by the system. A system with a globally stable equilibrium is thus capable of absorbing perturbations of whichever magnitude. This definition is more stringent than the classic notion of local stability derived from the Lyapunov theorem (Chapter 2): a globally stable equilibrium is also locally stable, but not viceversa. Instead of merely proving the existence of a region of asymptotic stability (considering small perturbations around the equilibrium), now the issue lies in computing its actual boundaries.

In this chapter, the basins of attraction of stable equilibria of the simple vehicle-and-driver model is exactly defined, exploiting a kinetic energy-based Lyapunov function. A correlation with the results obtained utilizing the Milliken Moments Method (MMM) is also established. The effective existence of a domain of attraction for the vehicle-and-driver system was already proven by the authors of [2] through experiments at the driver simulator with a human in the loop and on track, focusing on rectilinear motion only.

4.1. Milliken Moment Method

One of the earliest studies concerning global stability of road vehicles can be attributed to the Milliken brothers [4]. While not directly addressing the subject in a formal way, their work was driven by the desire of analysing the stability, control and maneuvering performance of the vehicle in a concise manner, with particular relevance for racing applications. The culmination of this research effort is the MRA Milliken Moment Method (MMM), which is based on the study of steady-state forces and moments on the vehicle.

The original approach, thoroughly described in [4], consisted in measuring the forces and moments during a constrained test while varying the steering angle and the vehicle slip angle, to reproduce different operating conditions. In reality, the test requires the vehicle to be constrained also in the longitudinal direction so that braking or traction forces can be accounted for and a wider range of maneuvering characteristics can be explored. Nonetheless, since the vehicle model used in this thesis work is built on the assumption of constant longitudinal velocity, this additional aspect is not relevant for the present analysis and will not be covered here.

The output of the analysis is the Milliken diagram: all the operating points obtained through testing are represented in the lateral force-yaw moment plane. Despite the inherent static nature of the testing procedure, the measured forces and moments can be used to characterize the vehicle behaviour also during a dynamic maneuver. Indeed, the D'Alambert's principle states that the acceleration of a body can be represented by applying a reversed effective inertia force (or moment) to it, thus bringing it in a static equilibrium condition. Each point on the Milliken diagram then corresponds to a specific combination of lateral acceleration and yaw acceleration. Assuming the absence of external forces acting on the vehicle, all the lateral force generated by the tyres is used to balance the centrifugal force. The Milliken diagram can thus be constructed by measuring the front and rear tyre lateral forces for different values of vehicle slip angle (β) and steering angle (δ). The coordinates (FM, MM) of each point of the diagram can be calculated as:

$$\begin{cases} FM = F_{y_f} + F_{y_r} \\ MM = F_{y_f} a - F_{y_r} b \end{cases} \tag{4.1}$$

The diagram obtained by simulating the constrained test using the simple single-track vehicle model (1.9) is represented in Fig. 4.1. The ranges of values considered for δ and β are listed in Table 4.1. Since the model used does not account for rolling resistance and aerodynamic forces, the shape of the diagram is in this case not affected by the longitudinal speed.

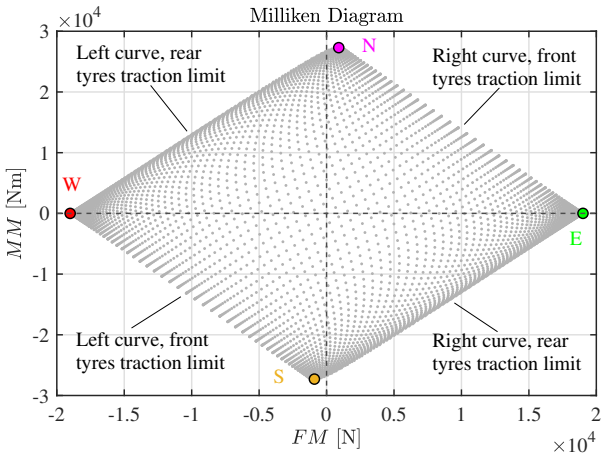

Figure 4.1: Milliken diagram, simple single-track model (data in Tables 1.1 and 1.2).

	Min	**Max**
Vehicle slip angle, β	-15°	15°
Steering angle, δ	-9.3°	9.3°

Table 4.1: Data considered to build the Milliken diagram, using the simple single-track vehicle model.

The Milliken diagram makes clear the limits of a vehicle's handling capability: the front axle traction limit is found in correspondence of the upper right edge of the diagram for a right turn; the lower right edge represents instead the traction limit at the rear axle, once again for a right turn. The situation is reversed for a left turn, with saturation of the front (resp. rear) axle happening at the lower (resp. upper) left edge. That is, adopting the SAE vehicle axis system (Sect. 1.1.1). In correspondence of the right corner (labelled "E" for East in Fig. 4.1) and left corner ("W" for West) of the diagram, both axles reach saturation and the front and rear axle lateral forces act in the same direction; therefore, the absolute value of the total force FM and the yaw moment MM are respectively the maximum and the minimum encountered along the border of the diagram. The upper ("N" for North) and lower ("S" for south) corners represent situations wherein both axles reach again saturation, but the front and rear axle lateral forces act in opposite directions: the absolute value of the yaw moment is maximum while the forces tend to balance out.

The location of the cardinal points with respect to the coordinate axes depends on the axle characteristics. In this case, the peak values of the front and rear effective axle characteristics are equal (see Fig. 1.4); consequently, when the two axles reach saturation

in the same direction, a quick calculation using Eq. (4.1) reveals that the residual yaw moment is null. One can then conclude that points E and W must lie exactly on the horizontal axis. For what concerns points N and S, it suffices to note that the maximum lateral force that the front axle can generate is higher than the maximum lateral load supported by the rear axle (see Fig. 1.2); when the axles reach saturation in opposite directions, a residual lateral force will then necessarily act on the vehicle in the direction determined by F_{y_f}, so that point N (resp. S) must lie in the half-plane of positive (resp. negative) FM values.

In the next sections of this chapter, it will be shown that for a vehicle running at low longitudinal velocity, i.e. far from the Hopf bifurcation, the domain of attraction of the stable equilibrium in the (v, r)-plane is surprisingly well approximated by the Milliken diagram, despite the latter not taking into consideration the effect of the driver on dynamics.

4.2. Kinetic Energy-Based Lyapunov Function

Following the same approach proposed in [2], we exploit a Lyapunov function to define the basin of attraction of stable equilibria of the vehicle-and-driver system. As stated in [30], according to Zubov's theorem a Lyapunov function can be used to describe the necessary and sufficient conditions for a certain subspace of the phase space to be the region of asymptotic stability for a particular equilibrium of a nonlinear system. While the application in [2] was limited to the motion along a rectilinear path (1.29), in the upcoming sections we also focus on circular motion (1.30).

Let us assume that the initial state of the system is the stable equilibrium $\bar{\boldsymbol{z}} \in \mathbb{R}^n$. Further assume that the system is perturbed at $t = 0^+$, and that the motion of vehicle-and-driver after the perturbation can be described by the state vector $\boldsymbol{z}(t) \in \mathbb{R}^n$, where $\boldsymbol{z}(0^-) = \bar{\boldsymbol{z}}$. Then, the expression of the first derivative $\dot{V}(t)$ of the scalar Lyapunov function V is:

$$\dot{V}(t) = -|\Delta E_k(t)| = -|E_k(\boldsymbol{z}(t)) - E_k(\bar{\boldsymbol{z}})|$$

i.e. minus the absolute value of the variation of kinetic energy with respect to the equilibrium condition. The complete expression of $\dot{V}(t)$ should include the steering energy, although in [2] it is noted that this contribution is negligible, at least in the case of rectilinear motion. Here we assume that the same result holds true also for circular motion. Moreover, to extend the analysis to the circular path model we had to introduce the absolute value of ΔE_k, due to the requirement that $\dot{V}(\boldsymbol{z}(t)) < 0$, $\forall\, \boldsymbol{z}(t) \in \Omega \neq \bar{\boldsymbol{z}}$, where Ω is an open set that contains $\bar{\boldsymbol{z}}$. Using the fundamental theorem of calculus, we can now

write for a generic disturbance $\boldsymbol{z}(0^+)$:

$$V(\boldsymbol{z}(\bar{t})) - V(\boldsymbol{z}(0^+)) = \int_{0^+}^{\bar{t}} \dot{V}(t)dt$$

The key is to understand that if $\boldsymbol{z}(0^+)$ belongs to the basin of attraction of the equilibrium $\bar{\boldsymbol{z}}$, then $\lim_{t\to\infty} \boldsymbol{z}(t) = \bar{\boldsymbol{z}}$, so that by definition $V(\boldsymbol{z}(\bar{t})) \simeq 0$ when $\bar{t}$ is large enough. Then, the following final expression is obtained:

$$V(\boldsymbol{z}(0^+)) = -\int_{0^+}^{\bar{t}} \dot{V}(t)dt = \int_{0^+}^{\bar{t}} |\Delta E_k(t)|dt > 0 \tag{4.2}$$

Since the main assumption behind the vehicle model considered in this work is that the throttle is controlled to keep the longitudinal velocity constant, $\Delta E_k(t)$ is simply the sum of a linear contribution due to the change of lateral velocity v and a rotational contribution associated to the yaw rate r:

$$\begin{aligned}\Delta E_k(t) &= \Delta E_k(t)_{lat} + \Delta E_k(t)_{rot} = \\ &= \frac{1}{2}m\left[v^2(t) - v^2(0^-)\right] + \frac{1}{2}J\left[r^2(t) - r^2(0^-)\right]\end{aligned} \tag{4.3}$$

Eqs. (4.2) and (4.3) can be used to compute the domain of attraction of the stable equilibrium $\bar{\boldsymbol{z}}$. Indeed, an initial disturbance $\boldsymbol{z}(0^+)$ is controlled if and only if the variation of kinetic energy (4.3) eventually goes to zero along the trajectory:

$$\lim_{t\to\infty} \Delta E_k(t) = 0 \iff V(\boldsymbol{z}(0^+)) < \infty \tag{4.4}$$

This suggests that the stability of the vehicle-and-driver system can be studied by referring to the state variables v and r only, and that monitoring the variation of the kinetic energy during the motion of the vehicle might be an effective strategy for advanced control algorithms to detect whether the motion is becoming unstable [2]. To further solidify this concept, let us integrate the power balance equation (1.12) for the vehicle:

$$\begin{aligned}\Delta E_k(t) = &\int_{0^-}^{\bar{t}} F_{y_f}(\delta, v, r)\left[v + ra\right]dt + \int_{0^-}^{\bar{t}} F_{y_r}(v, r)\left[v - rb\right]dt + \\ &- \int_{0^-}^{\bar{t}} muvr\,dt + \int_{0^-}^{0^+} Fv\,dt + \int_{0^-}^{0^+} Mr\,dt\end{aligned}$$

The above equation remarks the importance of the kinetic energy variation, since $\Delta E_k(t)$ conveys information about all the forces acting on the vehicle.

Fig. 4.2 helps visualize how the evolution of $\Delta E_k(t)$ differs between a controlled maneuver and an uncontrolled maneuver. In the first case, the system is able to absorb the initial energy input associated to the perturbation and the kinetic energy eventually returns to the steady state value; in the second case, the driver loses vehicle control and the energy grows steeply.

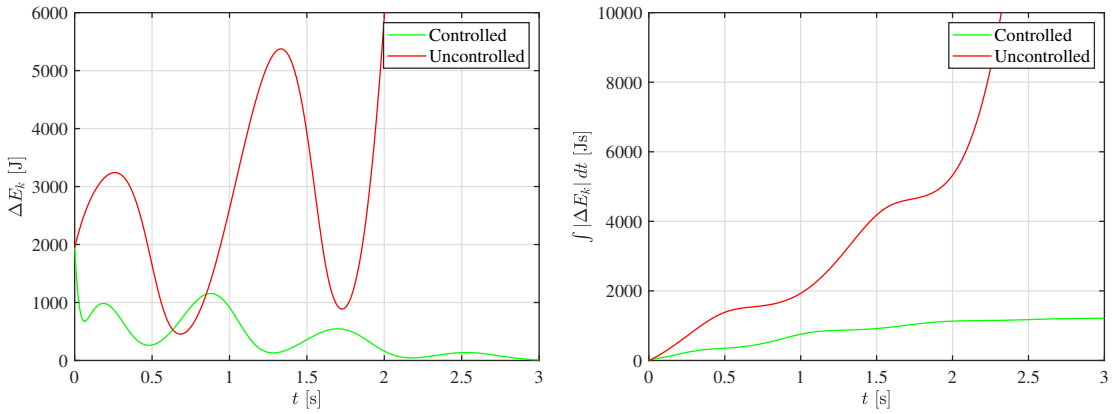

Figure 4.2: Example of time history of the variation of kinetic energy with respect to the equilibrium condition (on the left) and its integral (on the right) for a controlled and an uncontrolled maneuver. At $t = 0$ a disturbance is applied (instantaneously) while vehicle and driver are running along a rectilinear path (simple vehicle-and-driver model).

4.2.1. Basin of Attraction - Rectilinear Motion

The introduced concepts are first applied to study the global stability of vehicle and driver running along a rectilinear path. To define the basin of attraction of the equilibrium, which is locally stable for values of u lower than the critical speed, we start by defining a set of $N = 10^4$ disturbances $\boldsymbol{z}_i(0^+)$, $i = 1, 2, ..., N$, uniformly distributed in the phase space, using a Sobol sequence. In particular, only perturbations that belong to the (v, r)-plane are considered; they are associated to the action of external impulses F and M, which is a common and relevant load case for a road vehicle (e.g. side-wind). The two state variables are also physically relevant since they are involved in the expression of the kinetic energy of the vehicle.

Once a set of initial disturbances is chosen, the response of the simple vehicle-and-driver model is simulated for each $\boldsymbol{z}_i(0^+)$, computing at each instant the kinetic energy variation (4.3). In this case $v(0^-) = 0$ and $r(0^-) = 0$ since rectilinear motion is being considered as steady-state. The simulation end time must be selected to ensure that trajectories starting from initial states which belong to the domain of attraction ultimately

converge to the equilibrium, as the effectiveness of the presented method is based on condition (4.4). Considering that the period of the saddle-type limit cycle which characterizes large motions of the system is between 1 and 2 seconds, choosing a simulation end time upwards of 10 seconds should guarantee an accurate estimation of the basin of attraction.

The kinetic energy variation $\Delta E_{k_i}(t)$ is used to compute the Lyapunov function $V(\boldsymbol{z}_i(0^+))$ through Eq. (4.2), for each i-th simulation. Disturbances which excite unstable motions can easily be distinguished from the rest: since the variation of kinetic energy does not vanish during an unstable motion (as in Fig. 4.2), we have $\lim_{t\to\infty} V(\boldsymbol{z}(0^+)) = \infty$ and therefore the necessary and sufficient condition (4.4) for asymptotic stability is not met. On the contrary, stable motions produce finite values of the Lyapunov function: the kinetic energy of the system eventually returns to the steady-state value and the integral term in (4.2) converges. Since the simulation time is not infinite, operatively this means that a threshold V_{thr} must be selected to distinguish controlled ($V(\boldsymbol{z}(0^+)) \leq V_{thr}$) and uncontrolled ($V(\boldsymbol{z}(0^+)) > V_{thr}$) maneuvers. This step is sensitive to the extension of the simulation time interval. If the simulations are stopped too early, the gap in energy content between stable and unstable motions might not be pronounced enough to accurately define the border of the basin of attraction. Defining the threshold might then reveal to be a trial and error procedure.

Since a two-dimensional set of disturbances in the phase space was considered, the magnitude of the Lyapunov function $V(\boldsymbol{z}_i(0^+))$ calculated for each i-th simulation can be conveniently visualized with a heatmap in the (v, r)-plane. In Fig. 4.3 the heatmap obtained with the vehicle running at $u = 90$ km/h is pictured, alongside the scattered representation of the basin of attraction of the stable equilibrium at the same speed. Repeating the analysis increasing the vehicle speed to 120 km/h yields the results reported in Fig. 4.4. In both cases, the simulation end time was set to $t = 50\,\mathrm{s}$.

A quick comparison between the domains calculated at the two forward speeds unveils one of the most relevant issues concerning the global stability of road vehicles: the basin of attraction of the stable equilibrium shrinks as the vehicle speed increases, i.e. as the system operates closer to the Hopf bifurcation. This means that the system is less capable of absorbing perturbations of higher amplitude, which is reasonable since the equivalent damping decreases.

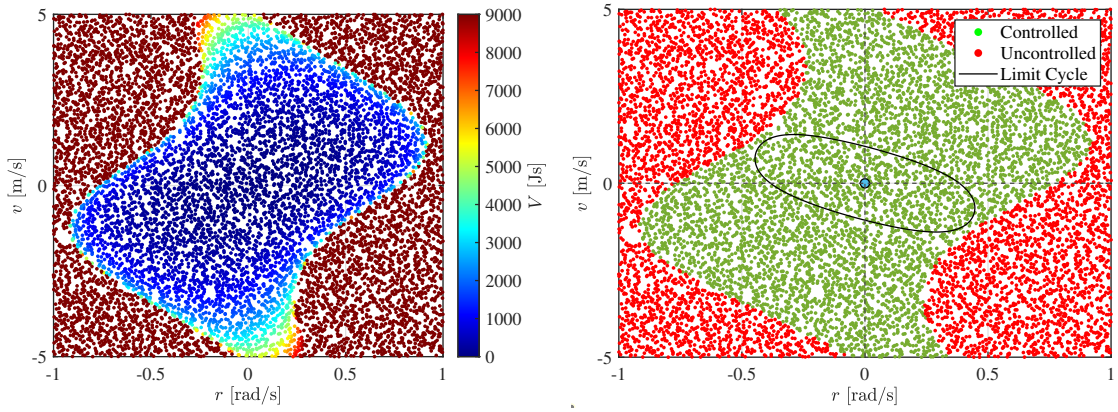

(a) Heatmap of Lyapunov function. Stable motion below $V_{thr} = 9 \cdot 10^3$ Js.

(b) Basin of attraction.

Figure 4.3: Straight-line motion: computation of the basin of attraction of the stable equilibrium at $u = 90$ km/h in the (v, r)-plane.

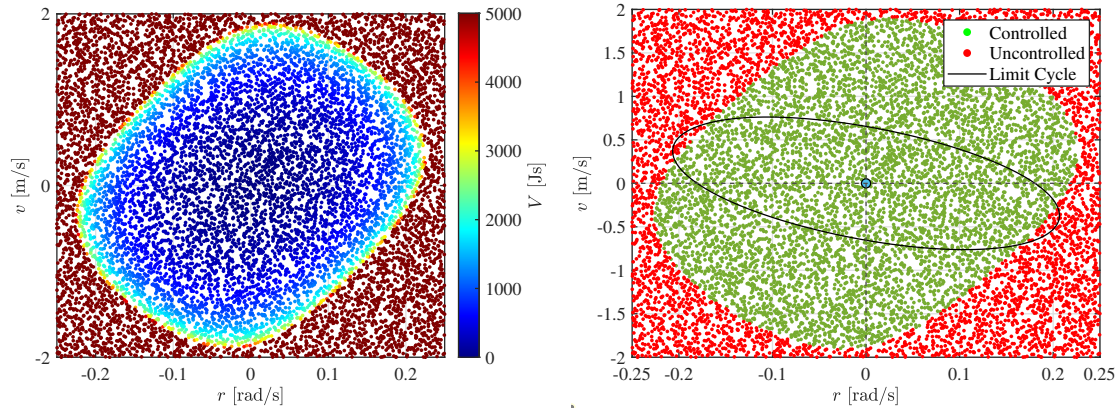

(a) Heatmap of Lyapunov function. Stable motion below $V_{thr} = 5 \cdot 10^3$ Js.

(b) Basin of attraction.

Figure 4.4: Rectilinear motion: computation of the basin of attraction of the stable equilibrium at $u = 120$ km/h in the (v, r)-plane.

Correlation with Milliken

To understand whether the tyre forces play a significant role in the definition of the stability region, we now aim at establishing a connection between the results obtained in this section and the results by Milliken (Sect. 4.1). A disturbance in the (v, r)-plane can easily be represented as one point in the (FM, MM)-plane, since the axle lateral forces depend on the slip angles (Sect. 1.1.2) and consequently on v and r. F_{y_f} also depends

on δ, but for the motion along a straight line $\delta(0^+) = \delta(0^-) = 0$ if the perturbation is not applied on the steering angle. In Fig. 4.5, the basin of attraction at $u = 90$ km/h in the (v, r)-plane is represented alongside its transposition to the (FM, MM)-plane. The same plots are visible in Fig. 4.6 for $u = 120$ km/h.

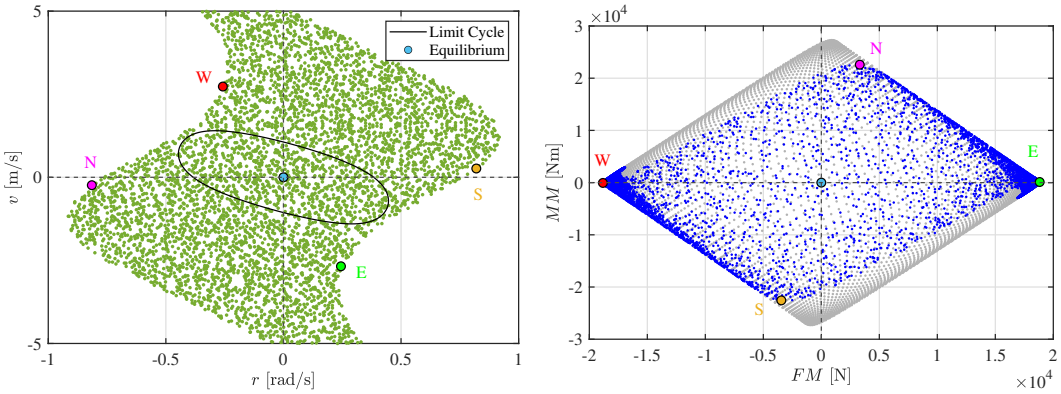

(a) (v, r)-plane. (b) (FM, MM)-plane.

Figure 4.5: Rectilinear motion: comparison between the basin of attraction and the Milliken diagram at $u = 90$ km/h. Blue dots in (b) refer to initial states that belong to the basin of attraction; grey dots are the output of the MMM, as in Fig. 4.1. At low speed, the Milliken diagram explains well the results of the stability analysis.

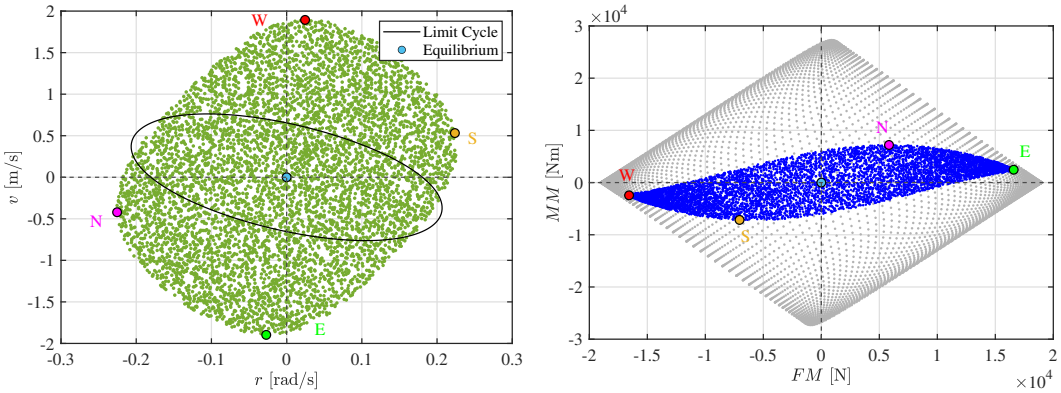

(a) (v, r)-plane. (b) (FM, MM)-plane.

Figure 4.6: Rectilinear motion: comparison between the basin of attraction and the Milliken diagram at $u = 120$ km/h. At high speed, the basin of attraction (green and blue dots) shrinks considerably and covers a limited portion of the Milliken diagram (grey dots).

At low speed, i.e. far from the Hopf bifurcation (which occurs at $u = 124.4$ km/h), there is a remarkable matching between the basin of attraction in the (v, r)-plane calculated with the Lyapunov function and the results of the Milliken Moment Method (MMM), which is surprising since no direct reference is made in [4] to the global stability problem. Additionally, this correlation indicates that the influence of the driver on vehicle stability is relatively insignificant at lower speeds, since the MMM is performed considering the vehicle with fixed control. As a consequence, far from the Hopf bifurcation a force-based stability threshold could be defined. The reader may refer to [16] for a more detailed explanation on how the tyre forces can be measured in real time to improve vehicle stability. In the cited work it is also verified that the effect of the driver on the extension of the Milliken diagram (intended as stability region) is negligible, and that the diagram is primarily determined by the tyre characteristics, if a human driver is considered.

The representation of the basin of attraction on the (FM, MM)-plane also highlights that rear axle saturation is the most critical condition from the point of view of vehicle stability. At $u = 90$ km/h, the upper right and lower left edges of the diagram, which indicate front axle saturation, are populated by points that belong to the border of the stability region; notice instead how the traction limit at the rear (lower right and upper left edges of the diagram) is never reached along the border of the stability region, except when the front axle is also at the limit (points E and W). In short, we can conclude that if the rear axle reaches saturation and the front axle does not, the driver will most likely be unable to maintain control of the vehicle; reaching the traction limit at the front axle constitutes instead a less dangerous condition in comparison. This is a well-known result in vehicle dynamics. In any case, one can expect that the Milliken diagram will more accurately represent the stability region if the speed is lowered further.

The story is quite different at higher speed, i.e. closer to the Hopf bifurcation. Fig. 4.6 shows that at $u = 120$ km/h the portion of the Milliken diagram covered by the stability region is much more limited in comparison to what was observed at lower speed. This implies that relying solely on measurements of tyre forces may not provide consistent information about the vehicle's stability until the driver has completely lost control.

Role of the Saddle-Type Limit Cycle

The influence of the saddle-type limit cycle on large motions of vehicle-and-driver and therefore its direct involvement in determining the region of attraction of stable equilibria of the system still remains unclear after the analysis. While the issue will be formally addressed in Chapter 6, we can already derive some qualitative insights by observing the

behaviour of orbits that originate from initial states near the boundary of the basin of attraction in the (v, r)-plane. In Fig. 4.7 the orbit of a simulation wherein the driver successfully returns to the straight path is compared with the orbit obtained for an uncontrolled maneuver. Results are reported for $u = 90$ km/h and $u = 120$ km/h. Notice how the orbits evolve towards the cycle and then, after some oscillations, either diverge towards a spin condition or converge to the stable equilibrium, depending on whether the initial state is inside or outside the basin of attraction. Initial states that lie *exactly* on the border of the stability region correspond to trajectories which converge to the limit cycle for $t \to \infty$: the boundary of the basin of attraction is the stable manifold of the saddle-type limit cycle.

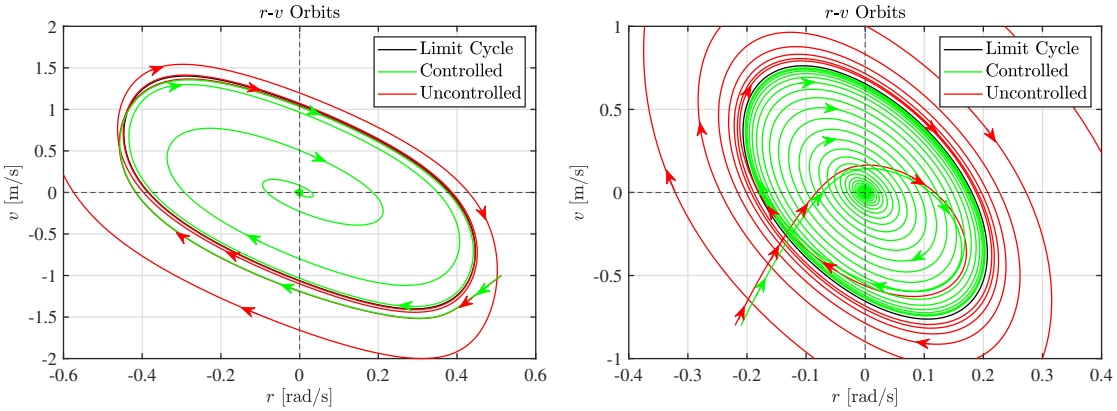

Figure 4.7: Rectilinear motion: comparison between the orbits of a controlled and an uncontrolled maneuver. Projections on the (v, r)-plane. Orbits that start from initial states near the border of the basin of attraction approach the saddle-type limit cycle and after some oscillations they are repelled, either towards the stable equilibrium (controlled maneuver) or towards a spin condition (uncontrolled maneuver).

While convergence to the limit cycle is in reality a quite unusual occurrence since the disturbance must be tuned very accurately, this is a key concept to understand since it tells us that the saddle cycle is directly involved in defining the basin of attraction of equilibria of the system, and thus that it plays a pivotal role in the assessment of global stability of road vehicle and driver. The intersection of the stable manifold of the cycle with the (v, r)-plane is considered of particular interest since, as already commented, the two state variables are the most relevant within the realm of vehicle stability; following the nomenclature proposed in [2], we will be referring to it using the acronym of ISMaVeR (Intersection of the Stable Manifold with the lateral-Velocity/yaw-Rate plane).

4.2.2. Basin of Attraction - Circular Motion

In this section, we aim to show that a stability region exists also when considering the steady-state motion along a circular trajectory, using the simple vehicle-and-driver model (1.30). The basin of attraction is calculated again using Eq. (4.2), defining a threshold V_{thr} on the Lyapunov function V to distinguish controlled ($V(\boldsymbol{z}(0^+)) \leq V_{thr}$) and uncontrolled ($V(\boldsymbol{z}(0^+)) > V_{thr}$) maneuvers.

As before, a uniform distribution of $N = 10^4$ perturbations $\boldsymbol{z}_i(0^+)$ in the (v, r)-plane is generated using a Sobol sequence. The response of the system to each $\boldsymbol{z}_i(0^+)$ is then simulated. The variation of kinetic energy (4.3) with respect to the steady-state condition is computed at each time step and is integrated along the entire duration of the maneuver to express the Lyapunov function (4.2). One could also think about directly using the kinetic energy variation itself to define the stability region, considering the left side of condition (4.4): it is sufficient to check whether $\Delta E_k(t)$ settles to a near-zero value towards the end of the simulation, provided that the end time is set high enough to allow near-convergence to the equilibrium in case the motion is stable.

The basins of attraction of four different steady-state cornering conditions are pictured in Fig. 4.8, where the red dots indicate initial states of the basin that were captured only by directly checking $\Delta E_k(t)$. This discrepancy indicates that the simulation was stopped too early. As one can deduce from Fig. 4.9, the system is in fact able to absorb disturbances located in this additional region of the basin, but only after a massive increase in kinetic energy. Accordingly, the Lyapunov function V easily surpasses the defined threshold V_{thr} and as a result this set of initial states gets filtered out from the basin of attraction. Directly monitoring $\Delta E_k(t)$ permits instead to correctly identify that the resulting motion is in fact stable, since instead of integrating the energy variation over the complete duration of the maneuver, we are just checking that it eventually settles to zero.

Of course, classifying these solutions as stable is meaningful only from a purely mathematical standpoint: in reality, they involve excessive excursion in lateral velocity (see Fig. 4.9a) and cannot be considered safe conditions on road, nor are they realistic (the ESP would immediately intervene, but is not included in the model). In this regard, we can conclude that using the Lyapunov function V is the more realistic approach to the global stability problem. Increasing the simulation end time would definitely improve the accuracy of the method, but the higher computational cost would not be worth it.

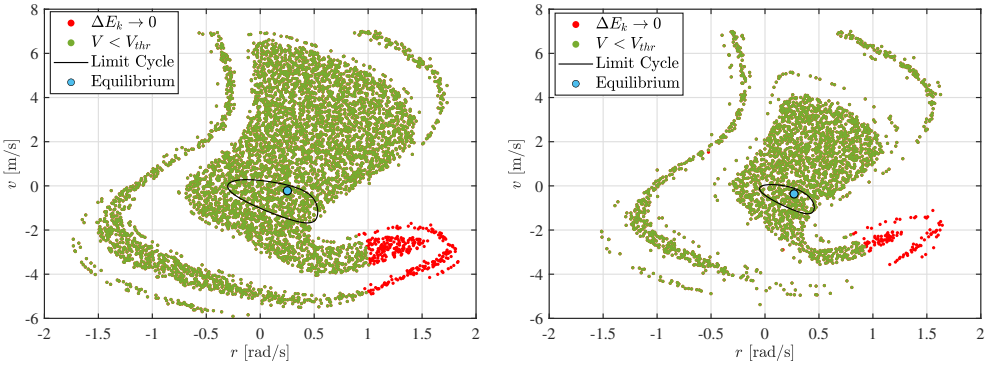

(a) $\rho = 80$ m, $u = 73$ km/h. (b) $\rho = 80$ m, $u = 78$ km/h.

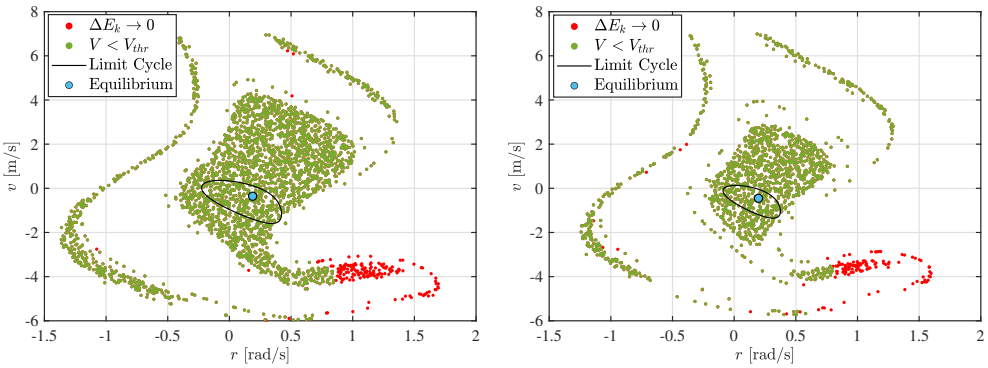

(c) $\rho = 130$ m, $u = 88$ km/h. (d) $\rho = 130$ m, $u = 92$ km/h.

Figure 4.8: Circular motion: basin of attraction for different combinations of (u, ρ). Red dots indicate additional initial states belonging to the basin of attraction that could not be obtained with the Lyapunov function (V) as they provoke a big excursion in lateral velocity (v) and thus surpass the threshold set for V ($V_{thr} = 7 \cdot 10^4$ Js, simulation end time $t = 50$ s in all cases). The basin appears as a multitude of discrete regions, due to the interaction between multiple saddle-type limit cycles. The Hopf bifurcation for a fixed turn radius of $\rho = 80$ m occurs at $u = 81.4$ km/h; for $\rho = 130$ m, at $u = 96.4$ km/h.

Finally, we note that the onset of motions similar to the one described could be detected by monitoring the tyre forces, since the traction limit of the tyres is quickly overcome after the application of the disturbance, as shown in Fig. 4.9c. Remembering that the vehicle can become understeering at high lateral accelerations (see the handling curve in Fig. 1.4), this could explain why the driver is ultimately able to regain control of the vehicle. Selecting a disturbance in the red regions of any of the basins pictured in Fig. 4.8 and repeating the analysis would yield similar results; the precise characterization of these type of motions is therefore not important if the ultimate goal is to define a strategy to recognize the onset of a dangerous operating condition.

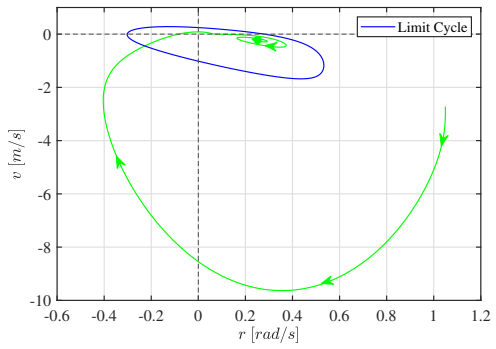

(a) Projection of the orbit in the (v, r)-plane.

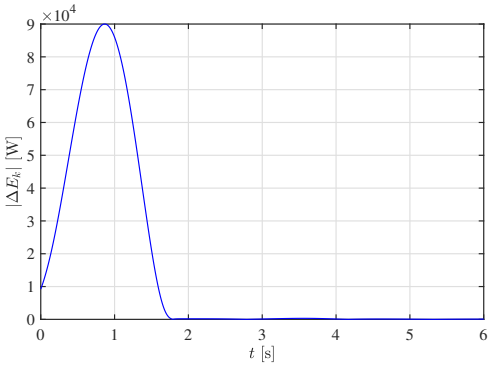

(b) Evolution of the absolute variation of kinetic energy.

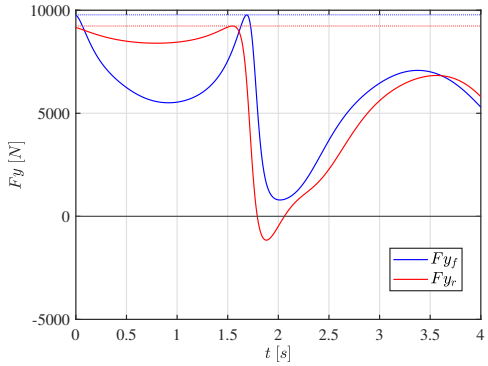

(c) Evolution of the front (F_{y_f}) and rear (F_{y_r}) axle lateral forces.

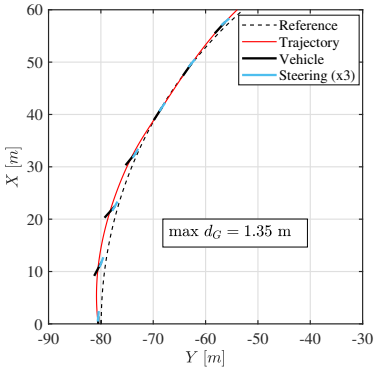

(d) Vehicle trajectory.

Figure 4.9: Circular motion: response of the system to an initial disturbance $(\Delta v, \Delta r) = (-2.5\,\text{m/s}, 0.8\,\text{rad/s})$ with respect to the steady state cornering condition at $u = 73$ km/h, $\rho = 80$ m (the green dot in (a)). The initial state belongs to the region of red dots in Fig. 4.8a and is associated with big excursion in v, high variation of kinetic energy and tyre saturation: the motion is asymptotically stable, but it is not safe.

Existence of Multiple Limit Cycles

Having explored a more specific aspect of the stability region to highlight possible difficulties associated with its definition, let us now return to a more general description. A quick glance at the scatter plots of Fig. 4.8 reveals that the basin of attraction of the steady state cornering condition is not a continuous region, differently from what was observed for rectilinear motion. Identifying the reason for this apparently strange behaviour requires going back to the bifurcation analysis of the vehicle-and-driver model performed in Section 3.3.2, in particular to the continuation of limit cycles from the subcritical Hopf bifurcation (Fig. 3.11).

Repeating the continuation with an increased maximum number of continuation steps reveals that multiple saddle-type limit cycles may exist for a given combination of the system parameters (u, ρ). Fig. 4.10 illustrates the orbits obtained from three different initial states, considering $u = 73$ km/h and $\rho = 80$ m. Similar results can be observed for other combinations of (u, ρ), but they are not reported here for the sake of space. The limit cycles that characterize the motion of the system are highlighted in each plot, for a total of three saddle-type cycles; they are labeled L_0, L_1, L_2 in ascending order of amplitude. More than three cycles were in fact identified during continuation runs, but it was chosen not to include them in the analysis since already L_1 and L_2 are much less relevant compared to L_0.

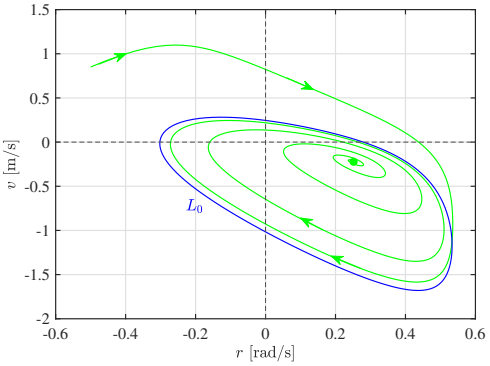

(a) $(\Delta v, \Delta r) = (1.1\,\text{m/s}, -0.75\,\text{rad/s})$.

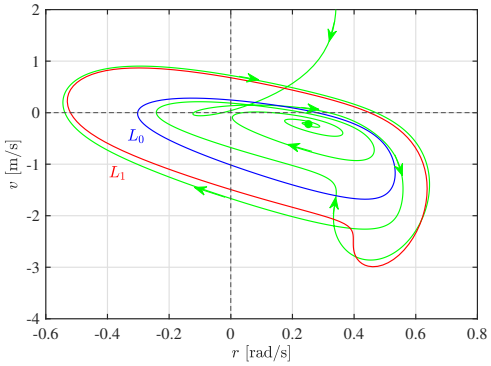

(b) $(\Delta v, \Delta r) = (7.15\,\text{m/s}, -0.2\,\text{rad/s})$.

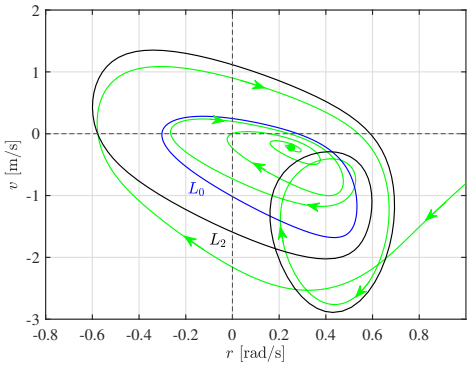

(c) $(\Delta v, \Delta r) = (4.1\,\text{m/s}, 1.45\,\text{rad/s})$.

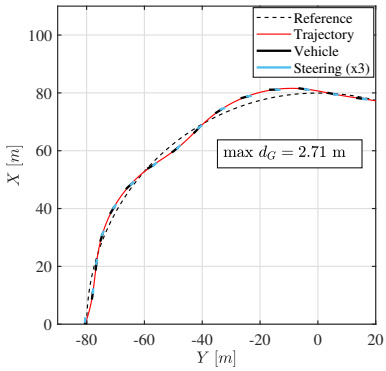

(d) Trajectory corresponding to the motion on L_1.

Figure 4.10: Circular motion: interaction between high amplitude limit cycles (L_1, L_2) and the low amplitude cycle L_0, all of the saddle type, at $\rho = 80$ m, $u = 73$ km/h. Three disturbances with respect to the steady-state cornering condition (green dot) are applied to simulate the response of the system. The resulting motions are asymptotically stable, but the ones represented in (b) and (c) involve big excursion in lateral position and are only provoked by severe perturbations, so they are unsafe.

In Fig. 4.10a, the system behaves as usual: the orbit is attracted to a saddle-type cycle and repelled by it shortly after, in this case towards the stable equilibrium. The cycle that characterizes the motion is the lowest amplitude one (L_0), discovered in Section 3.3.2. Things get more intricate in Fig. 4.10b. The orbit is attracted to an outer saddle-type cycle (L_1), then it gets repelled towards L_0 and finally converges to the equilibrium. The same behaviour is observed in Fig. 4.10b, but a different outer cycle (L_2) gets involved.

We can now understand why the ISMaVeR appears as a multitude of discrete regions: there is a strong interaction between multiple saddle-type limit cycles near the stable equilibrium. The effect becomes less evident as the system approaches the Hopf bifurcation, since L_0 shrinks while L_1 and L_2 do not. Nevertheless, the presence of the outer saddle-type limit cycles will be neglected for the remainder of this thesis work, for two main reasons:

- The outer cycles may represent motions that are unique to the simple vehicle-and-driver model utilized for the analysis and that do not translate effectively to a more complex model, especially considering the uncertainties related to how the control action of a human driver should be replicated in the mathematical model.
- Motions over the outer cycles involve high amplitude and long lasting oscillations (see Fig. 4.10d), and are observed only for disturbances which cause the tyres to quickly reach saturation. These solutions therefore constitute unsafe operating conditions that should be relatively easy to detect, and can be considered on par with mathematically unstable solutions.

In any case, being conscious of the fact that there could possibly be interactions between multiple saddle-type limit cycles could result useful for future studies.

Correlation with Milliken

The basin of attraction in the (v, r)-plane can easily be represented in the (FM, MM)-plane along with the Milliken diagram, as seen in the previous section. In this case, we consider only the main (central) portion of the stability region, as the remaining areas contain initial states that lead to motions influenced by the outer limit cycles. The results of this coordinate transformation are visible in Fig. 4.11 for multiple combinations of parameters (u, ρ).

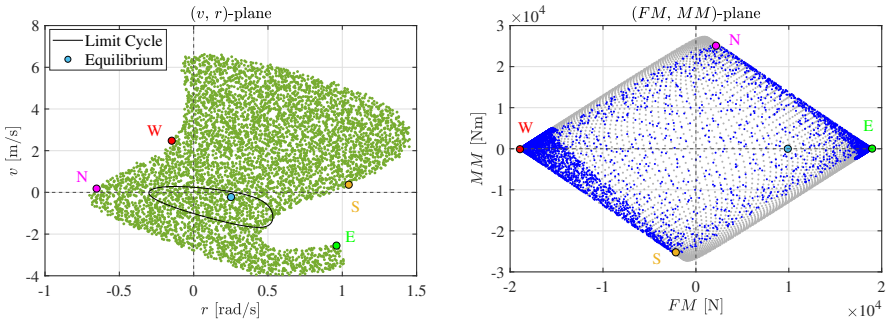

(a) $\rho = 80$ m, $u = 73$ km/h.

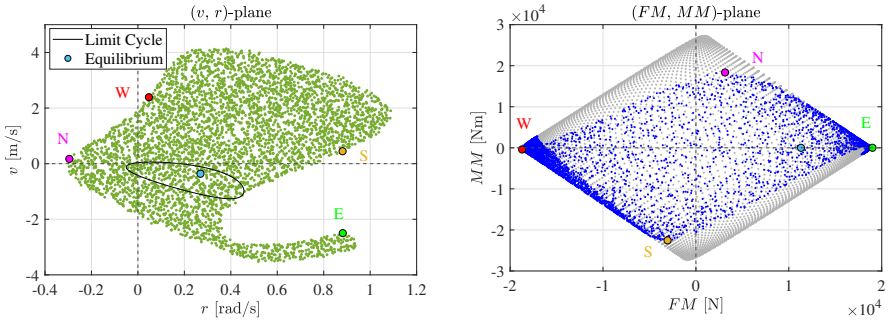

(b) $\rho = 80$ m, $u = 78$ km/h.

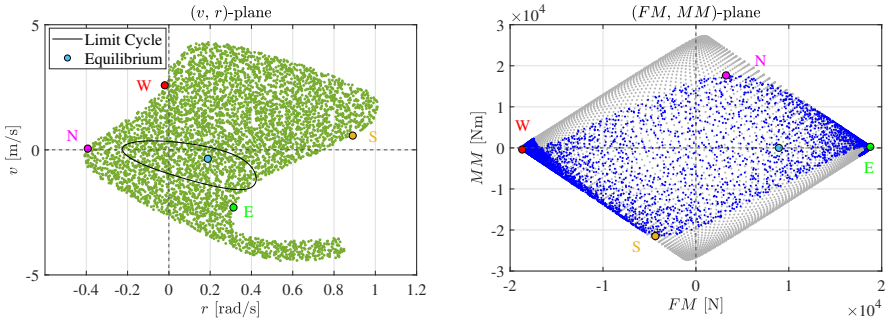

(c) $\rho = 130$ m, $u = 88$ km/h.

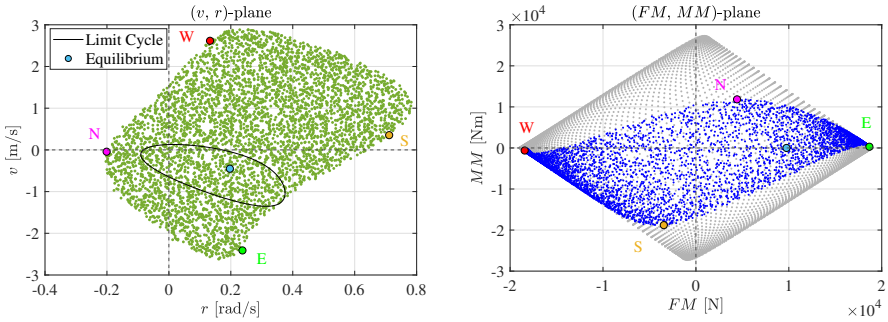

(d) $\rho = 130$ m, $u = 92$ km/h.

Figure 4.11: Circular motion: stability region and Milliken diagram as function of the radius ρ and speed u. The basin (green and blue dots) shrinks near the Hopf bifurcation, which occurs at $u = 81.4$ km/h for $\rho = 80$ m and at $u = 94.4$ km/h for $\rho = 130$ m.

We observe that the basin of attraction shrinks when approaching the Hopf bifurcation also when the vehicle moves along a circular trajectory. The forward speed u still has a great impact on the extension of the stability region, which reduces considerably for both values of ρ when u is increased. The basins calculated at $\rho = 130$ m are generally smaller than their counterparts at $\rho = 80$ m, again due to the overall higher speeds reached. In all cases, one can notice that the ISMaVeR is closer to the upper right and lower left edges of the Milliken diagram, indicating the increased tolerance of the system to absorb perturbations that cause saturation of the front axle. The rear axle can instead "safely" reach the traction limit only if the front is also saturated (points E and W), with the ISMaVeR never fully extending to the upper left and lower right edges of the Milliken diagram. Nonetheless, it remains true that at low speed there is a remarkable correlation between the ISMaVeR and the Milliken diagram, as it was observed in the previous section when analysing the perturbed rectilinear motion.

It is also interesting to note that the ISMaVeR extends further towards the lower left edge of the Milliken diagram in comparison to the upper right one. The two cardinal points W and S in the (v, r)-plane are placed below the region of the basin of attraction which extends into the first quadrant, where v and r are both positive. Remembering that the vehicle-and-driver model used for the analysis describes the motion along a right curve, disturbances in this part of the (v, r)-plane tend to push the vehicle towards the inside of the curve; it is then reasonable that this condition is compatible with a stable motion, assuming of course that the road is wide enough to accomodate high excursions in lateral position. Nonetheless, if the perturbation is overly strong the deviation with respect to the desired path becomes excessive, so that the countersteering action of the driver creates an opposing yaw moment that ultimately saturates the rear axle, making the motion unstable even if v and r are both positive.

5 | Kinematic/Energy Analysis

In the previous chapter, the common perception that a vehicle can become uncontrollable under the action of strong perturbations was made rigorous by computing the threshold above which the motion of the simple vehicle-and-driver model becomes unstable, i.e. the border of the basin of attraction of the stable equilibrium of the system. Once the existence of a stability region has been acknowledged, the issue becomes defining a strategy to sense the state of the vehicle in real-time during the motion and determine whether it is operating inside or outside this region, so that a corrective action can be taken, if necessary, to avoid the complete loss of vehicle control. In this regard, we observed how the Milliken Moment Method is able to explain stability only if the system operates far from the Hopf bifurcation, meaning that monitoring the tyre forces might not be the most suitable option to immediately detect the onset of an unstable behaviour at high speeds, when the stability threshold is quite lower than tyre saturation and the loss of stability occurs with less violence.

In this chapter, we introduce some significant kinematic quantities that could provide an early indication of the loss of vehicle control. Focus is placed primarily on the practical usefulness of these indices, whose derivation is thoroughly addressed in [3]. Kinematic analyses are traditionally based solely on an instantaneous representation of the vehicle during cornering, with quantities that offer an indication of how the motion is evolving being left out. The concepts here introduced have apparently never been employed before in vehicle dynamics, although they are useful tools that can be considered by vehicle engineers to design a vehicle that negotiates corners the proper way, requiring only data acquired with telemetry sensors.

5.1. Inflection Circle

Analogously to what was shown for the velocity field and the velocity centre C in Section 1.1.1, the coordinates of a body point K with zero acceleration can be calculated at any time instant during the planar motion of the vehicle. Point K is called *acceleration centre*. The displacement vector from the centre of mass G to point K assumes the

following expression in the vehicle reference system:

$$(K-G) = \frac{r^2 a_x - a_y \dot{r}}{\dot{r}^2 + r^4}\mathbf{i} + \frac{a_y r^2 + \dot{r} a_x}{\dot{r}^2 + r^4}\mathbf{j}$$

Point K is in general different from C; indeed, the velocity centre possesses a non-zero acceleration:

$$\mathbf{a}_C = \left(a_x - \dot{r}R - r^2 S\right)\mathbf{i} + \left(a_y + \dot{r}S - r^2 R\right)\mathbf{j} \tag{5.1}$$

For ease of reading, we also report here the expressions of the coordinates of the velocity centre (R and S) in the vehicle reference system and the explicit forms of a_x and a_y (see Section 1.1.1):

$$R = \frac{u}{r}$$
$$S = -\frac{v}{r}$$
$$a_x = \dot{u} - vr$$
$$a_y = \dot{v} + ur$$

Once the acceleration centre K and the velocity centre C have been located, one can think about identifying at each instant during the motion the locus of points for which the velocity and acceleration vectors are collinear. In other words, these points are characterized by vanishing centripetal acceleration at that particular instant, meaning that their trajectory has null curvature; this is the definition of *inflection point*. A locus that satisfies the given requirement does indeed exist in general and its points are always arranged on a circumference, the *inflection circle*. One trivial point of the circumference is the acceleration centre K, since its property is to have null acceleration and non-zero velocity: point K thus follows (instantaneously) a trajectory with zero curvature. The position and size of the inflection circle are completely defined by the acceleration vector $\mathbf{a}_C$. With reference to Fig. 5.1, the following relation always holds true:

$$(H-C) = \boldsymbol{d} = \frac{1}{r^2}\mathbf{a}_C \tag{5.2}$$

The vector $\boldsymbol{V}_{\hat{C}}$ is the velocity of the geometrical point $\hat{C}$ which represents the motion of the velocity centre in the plane; the expression of $\boldsymbol{V}_{\hat{C}}$ is:

$$\boldsymbol{V}_{\hat{C}} = \dot{S}\mathbf{i} + \dot{R}\mathbf{j} = \frac{\dot{r}v - r\dot{v}}{r^2}\mathbf{i} + \frac{r\dot{u} - \dot{r}u}{r^2}\mathbf{j}$$

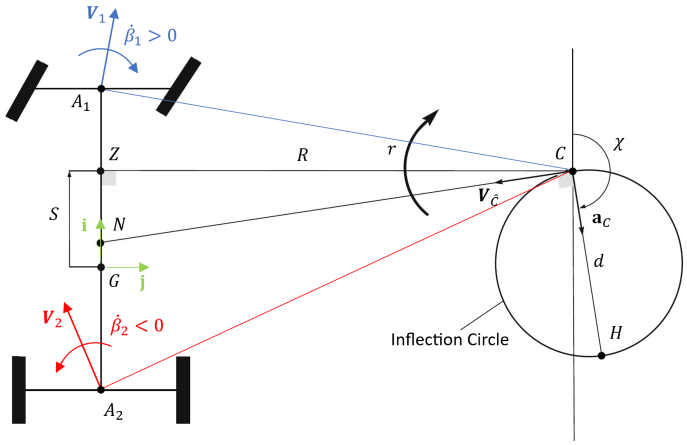

Figure 5.1: Inflection circle of a vehicle entering a right corner. Point C is the velocity centre. The geometrical point $\hat{C}$ corresponds to C (but does not belong to the body) and moves with velocity $\boldsymbol{V}_{\hat{C}}$. $\mathbf{a}_C$ is the acceleration of C, always perpendicular to $\boldsymbol{V}_{\hat{C}}$. $\dot{\beta}_N = 0$, $\beta_Z = 0$. Adapted from [3].

The velocity $\boldsymbol{V}_{\hat{C}}$ is always tangent to the inflection circle. Indeed, by manipulating Eq. (5.1) it can be shown that the acceleration of the velocity centre is always perpendicular to $\boldsymbol{V}_{\hat{C}}$:

$$\mathbf{a}_C = r\left(\dot{R}\mathbf{i} - \dot{S}\mathbf{j}\right) \tag{5.3}$$

It follows that the diameter (d) and orientation (χ) of the inflection circle can be compactly written as:

$$d = \sqrt{\frac{\dot{S}^2 + \dot{R}^2}{r^2}}$$

$$\tan(\chi) = -\frac{\dot{S}}{\dot{R}}$$

Monitoring how d and χ change during cornering enables a deep understanding of the vehicle performance [3], as both quantities contain important information about how the velocity field is evolving in time.

5.1.1. Inflection Circle Orientation

Changes in the direction of the velocity vector of any given point of the vehicle body are immediately conveyed by the orientation of the inflection circle. Indeed, the position of the velocity centre C for successive time instants can be inferred by observing the direction of $\boldsymbol{V}_{\hat{C}}$, or equivalently the magnitude of the angle χ. Points that lie on this direction at a given instant have the peculiarity of preserving the same slip angle at the successive

instant (e.g. $\dot{\beta}_N = 0$ in Fig. 5.1), since the velocity field is always rotational around the velocity centre; points above and below the CN segment will instead have opposite rates of change of the slip angle. In particular, it is relevant to understand how the front and rear axle slip angles evolve in time, since they are directly related to the lateral forces (see Section 1.1.2). Referring to Fig. 5.1, if one imagines to "slide" point C along the direction identified by $\boldsymbol{V}_{\hat{C}}$, it becomes clear that it must be $\dot{\beta}_1 > 0$ and $\dot{\beta}_2 < 0$. With a bit of reasoning, it can also be concluded that in general the axle closest to point N presents the lowest variation of slip angle. The lateral velocity instead vanishes for points along the CZ segment ($\beta_Z = 0$). Z and N should be close to each other and not far from the front axle to achieve good handling [3].

Including transient quantities such as $\dot{\beta}_1$ and $\dot{\beta}_2$ in the kinematic analysis conveys information about the performance of the vehicle during cornering, that would otherwise be missed. An example of desirable and undesirable behaviours of the vehicle during the entry phase of a cornering maneuver are shown in Fig. 5.2. The vehicle in Fig. 5.2b is not enering the curve properly as the front and rear slip angles are both tending to positive values and $|\dot{\beta}_2| > |\dot{\beta}_1|$, meaning that the vehicle is starting to drift. The situation is mirrored for what concerns the corner exit phase, as depicted in [3].

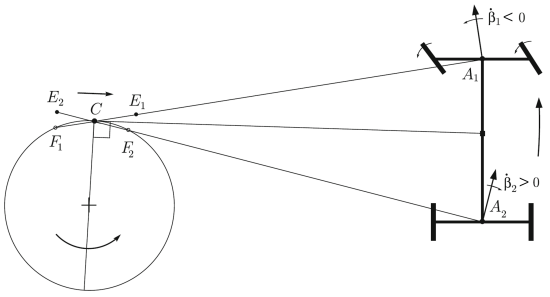

(a) "Good" behaviour.

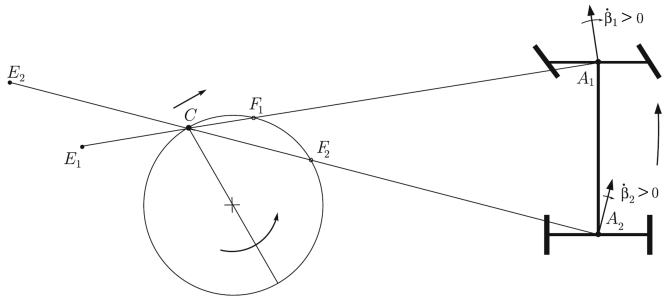

(b) "Bad" behaviour.

Figure 5.2: Examples of desirable (a) and undesirable (b) kinematics during the entry phase of a left corner. In (b), the longitudinal displacement of the velocity centre C signals that the vehicle is starting to drift ($\dot{\beta}_2 > \dot{\beta}_1 > 0$). Adapted from [3].

The angle χ can then be considered a kinematic index which condenses most of the information necessary to understand how the front and rear slip angles are evolving during the maneuver: monitoring the position of the velocity centre and the orientation of the inflection circle could help detect the onset of handling misbehaviour before the complete loss of vehicle control. In short, it can be said that χ should remain close to integer multiples of 180°, signaling that the velocity centre C is mostly traveling along the lateral direction with respect to the vehicle; longitudinal travel of C indicates instead an excessive variation of the slip angles.

It is also quite interesting to notice how the position and orientation of the inflection circle immediately convey the relationship between the velocity cetntre C and the curvature centres E_1 and E_2, also depicted in Fig. 5.2. Indeed, tracing the straight line through a given point of the vehicle P and the velocity centre C, the following relation must be fulfilled:

$$|PC|^2 = |PE|\,|PF| \tag{5.4}$$

where E is the centre of curvature of the trajectory followed by P and F is the intersection point of the straight line with the inflection circle; points E and F are always on the same side with respect to P. While computing the coordinates of point F is impractical, Eq. (5.4) is still useful to qualitatively identify the location of the centre of curvature E with respect to C. For instance, if $|PF| < |PC|$ then necessarily $|PE| > |PC|$; this is the case of E_2 in Fig. 5.2a, as well as E_1 and E_2 in Fig. 5.2b. Shorter PF correspond to longer PE, resulting in a smaller curvature.

5.1.2. Inflection Circle Diameter

The diameter of the inflection circle (d) is also a kinematic index worthy of consideration. In general, the inflection circle shrinks when the vehicle is entering the corner, then d reaches a minimum value mid-corner ($d = 0$ in the ideal case) and increases again during the exiting phase, following an inverse trend with respect to the yaw rate r. Remembering Eq. (5.2), the condition $d = 0$ can be achieved if and only if $\mathbf{a}_C = 0$. Only in this case, the velocity centre C and the acceleration centre K are coincident. Considering Eq. (5.3), the conditions for this occurrence read:

$$\begin{cases} \dot{R} = 0 \iff r\dot{u} - \dot{r}u = 0 \\ \dot{S} = 0 \iff \dot{r}v - r\dot{v} = 0 \end{cases} \tag{5.5}$$

which are also equivalent to stating that the location of the velocity centre must remain unvaried after an infinitesimal amount of time has passed, so that the condition $\dot{\beta}_P = 0$ is

satisfied for any point P of the vehicle. It is worth noting that considering the mid-corner point, in correspondence of which the yaw rate r is at its maximum absolute value during the turn ($\dot{r} = 0$), Eqs. (5.5) simplify to:

$$\begin{cases} \dot{u} = 0 \\ \dot{v} = 0 \end{cases}$$

Further assuming that the throttle is adjusted to keep the longitudinal speed of the vehicle constant during the maneuver, the only nontrivial condition left to satisfy is $\dot{v} = 0$, meaning that also the lateral velocity v should reach its peak absolute value mid-corner in order to achieve $d = 0$.

Based on the previous considerations, we can expect a V-like shaped plot for the time history of the inflection circle diameter d when traveling along a bend, with the minimum in correspondence of the mid-corner point; departure from the described shape can be interpreted as a warning of handling misbehaviour. For example, if d remains quite low after the mid-corner point it could mean that the vehicle is oversteering while exiting the turn, as the yaw rate r is not decreasing as rapidly as it should.

5.2. Centrodes

The *centrode* of a body is defined as the locus of velocity centres of the body in motion. Depending on the reference system considered when tracing the trajectory of the velocity centre C (or rather, the trajectory of the geometrical point $\hat{C}$), one can distinguish between *moving* and *fixed* centrode. The moving centrode σ_m is obtained by following the velocity centre C in the body-fixed reference system, while the fixed centrode is the curve that represents the trajectory of C in the global reference frame. The two centrodes can be represented together in the ground-fixed axis system, considering that σ_m moves rigidly with the vehicle. The moving centrode rolls without slip on the fixed centrode, as the two meet in correspondence of the velocity centre C at any given instant. An example of how the centrodes may appear during the entry phase of a left corner is visible in Fig. 5.3a.

The shape of the two centrodes reflects the intrinsic kinematics of cornering: both curves can be divided into two main parts, one corresponding to the entry phase (C moves towards the vehicle) and one representing the exit phase (C moves away from the vehicle); this is most clear observing the fixed centrode, while the moving centrode is closer to being a straight line, at least in the case of a well driven curve. As visible in Fig. 5.3a, the inflection circle is always tangent to the two centrodes in correspondence of the ve-

locity centre C, since the vector $\boldsymbol{d}$ which defines the orientation of the circle is always perpendicular to the velocity vector $\boldsymbol{V}_{\hat{C}}$ (Section 5.1.1).

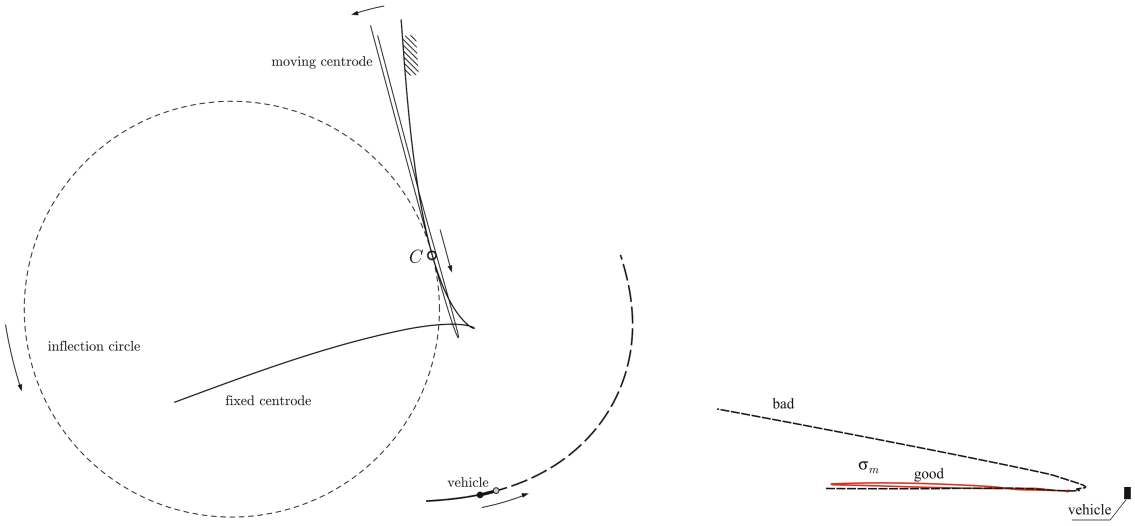

(a) Centrodes at the entrance of the corner.

(b) Comparison between a "good" and a "bad" moving centrode.

Figure 5.3: Centrodes of a vehicle during a cornering maneuver. The moving centrode moves rigidly with the vehicle and rolls on the fixed centrode. The Inflection circle is always tangent to the centrodes at the velocity centre C. In (b), the "bad" centrode presents excessive longitudinal travel of C, which is undesirable. Adapted from [3].

The centrodes are a graphical representation of all the geometric aspects of the kinematics of the cornering vehicle covered in the previous sections: it is then natural to conclude that the centrodes themselves can be used as a warning of handling misbehaviour. In Fig. 5.3b the moving centrode of a vehicle making a curve properly is compared to the centrode obtained when the vehicle is negotiating the same curve, but showing "bad" behaviour: indeed, we observe that in the latter case the velocity centre is displacing quite a lot in the longitudinal direction, which is not desirable as commented before.

5.3. Analysis of Perturbed Rectilinear Motion

The introduced concepts are now applied to investigate whether there are major kinematic differences between stable and unstable motions of the vehicle within the initial few seconds that follow the application of a preturbation. Two simulations are performed at a forward speed of $u = 90$ km/h, considering the simple vehicle-and-driver model for driving along a rectilinear path (1.29). The system is perturbed by intoducing a distur-

bance that only affects the lateral speed (v) and the yaw rate (r) of the vehicle, starting from steady-state conditions. The two disturbances are selected close to the ISMaVeR: the unstable motion is excited by a disturbance which is precisely strong enough to exceed the stability threshold. The projection of the trajectory undergone by the system on the (v, r)-plane is visible in Fig. 5.4, both for controlled and uncontrolled maneuver.

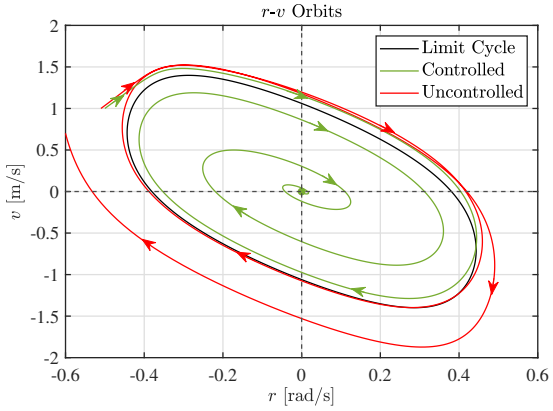

Figure 5.4: Orbits of the controlled and uncontrolled maneuver considered for the kinematic analysis. Simple vehicle-and-driver model, forward speed $u = 90$ km/h, rectilinear motion.

As expected, the system exhibits an oscillatory behaviour in response to both disturbances, which is typical of motions influenced by a limit cycle. Since the cycle is of the saddle-type, the trajectories are eventually repelled towards the stable equilibrium (controlled maneuver) or towards a spin condition (uncontrolled maneuver). The time histories of the kinematic indices d, χ and their derivatives are depicted in Fig. 5.5, along with the moving centrodes obtained at each half-oscillation during the maneuver. One can see that:

- If the motion is unstable, the diameter of the inflection circle (d) tends to increase less rapidly after the mid-corner point, meaning that at the beginning of the corner exit phase the yaw rate remains close to the peak value; this effect is indeed also visible, perhaps less clearly, in the time history of r plotted in Fig. 5.6. The V-shaped curve of the diameter appears progressively flatter at each consecutive turn when the maneuver is uncontrolled, while it gets sharper when the disturbance is being successfully absorbed by the system (i.e. the yaw rate assumes a more sinusoidal shape);
- The inflection circle "flips" mid-corner with respect to the y-axis of the vehicle reference system, transitioning from the entry phase (the velocity centre C gets

closer to the vehicle) to the exit phase (C moves away from the vehicle); examining the shape of the moving centrodes should help visualize this concept, remembering that the inflection circle remains tangent to the centrode at all instants. The time history of χ for a single turn therefore appears as a step-like shape between integer multiples of 180°. The transition becomes progressively slower if the maneuver is uncontrolled, until the shape of the moving centrode becomes the one observed at turn 4: the velocity centre remains close to the vehicle, which undergoes a spin;

- With reference to Fig. 5.3b, we observe that the shape of the moving centrode is never "good", even if the driver ultimately manages to recover from the disturbance; indeed, the velocity centre is travelling also longitudinally. The main difference between the centrodes of the controlled and uncontrolled maneuver is that the velocity centre remains closer to the vehicle in the latter case, but this is obvious since the amplitude of the oscillations of the yaw rate does not decay. If one relies solely on the observation of the centrode without any supplementary data, distinguishing between stable and unstable motion becomes unambiguous only when the vehicle is on the verge of spinning, at turn 4.

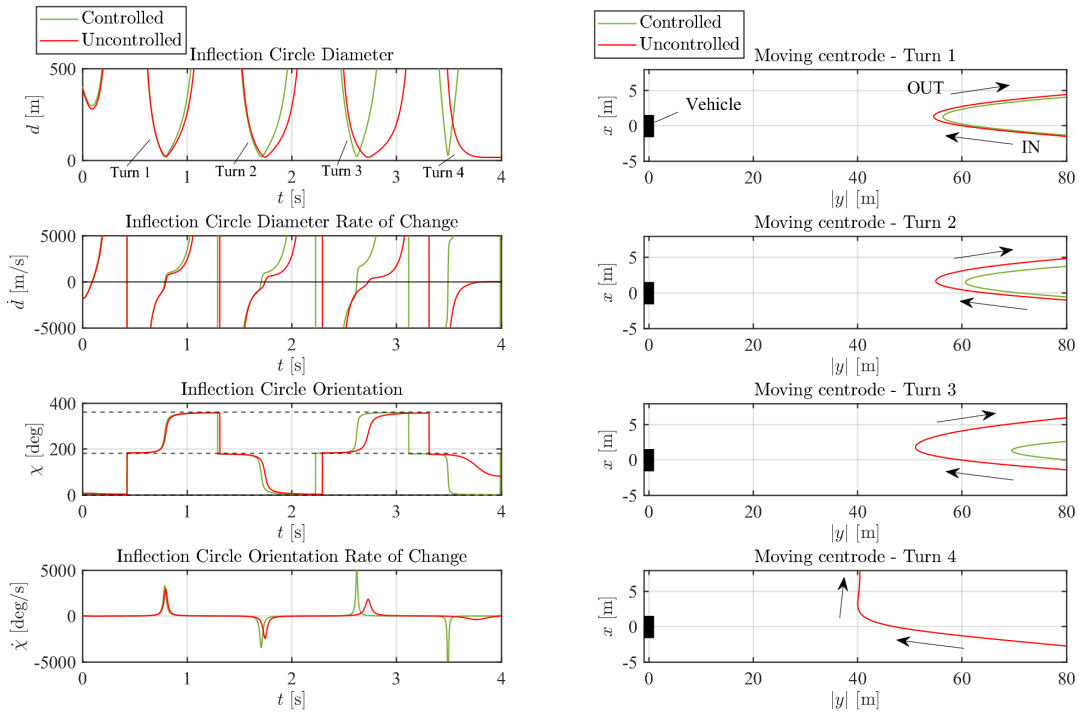

Figure 5.5: Kinematic indices and moving centrodes.

With reference to Fig. 5.6, the following qualitative observations can then be made:

- The motions excited by both disturbances are quite close for the first 2 seconds of the maneuver, making the early detection of unstable motion challenging if one relies solely on monitoring the state variables and the tyre forces;
- We can divide the time history of all quantities into "turns". A turn is essentially one complete half-oscillation of the yaw rate (r). Although these are not actual turns since the base motion is rectilinear, this step is necessary to correctly define the centrodes and to impart significance to the kinematic indices;
- If the disturbance is inside the stability region, the system is able to absorb it: the amplitude of the oscillations decays and after about 4 turns the system returns to the steady-state condition. On the contrary, if the magnitude of the perturbation exceeds the stability threshold the amplitude of the oscillations slightly increases at each turn, until the axles finally reach saturation at about $t \simeq 3.8\,\mathrm{s}$ and the driver loses control of the vehicle (the vehicle spins and y_G, ψ, v diverge);
- Stable and unstable motions differ markedly in terms of kinetic energy and powers. Indeed, in the unstable case the kinetic energy increases substantially at turn 3 when the axles have not reached saturation yet; as pointed out in the previous chapter, monitoring how the kinetic energy evolves during the maneuver could prove to be fundamental to detect the imminent loss of vehicle control;
- As anticipated in Section 1.1.4, the power of the rear axle lateral force is always dissipative; the steering action of the driver instead makes the power at the front axle positive during the entry phase of each turn, i.e. until the peak yaw rate is reached. Nonetheless, the overall contribution of the front axle lateral force to the energy content of the system is dissipative since the peak positive power is lower than the peak negative power;
- The power of the longitudinal forces is predominantly positive: as stated in [2], the energy that is used to make the system unstable is taken from the forward motion, through the driver's action. The motion becomes unstable when the tyres are not able to dissipate enough energy.

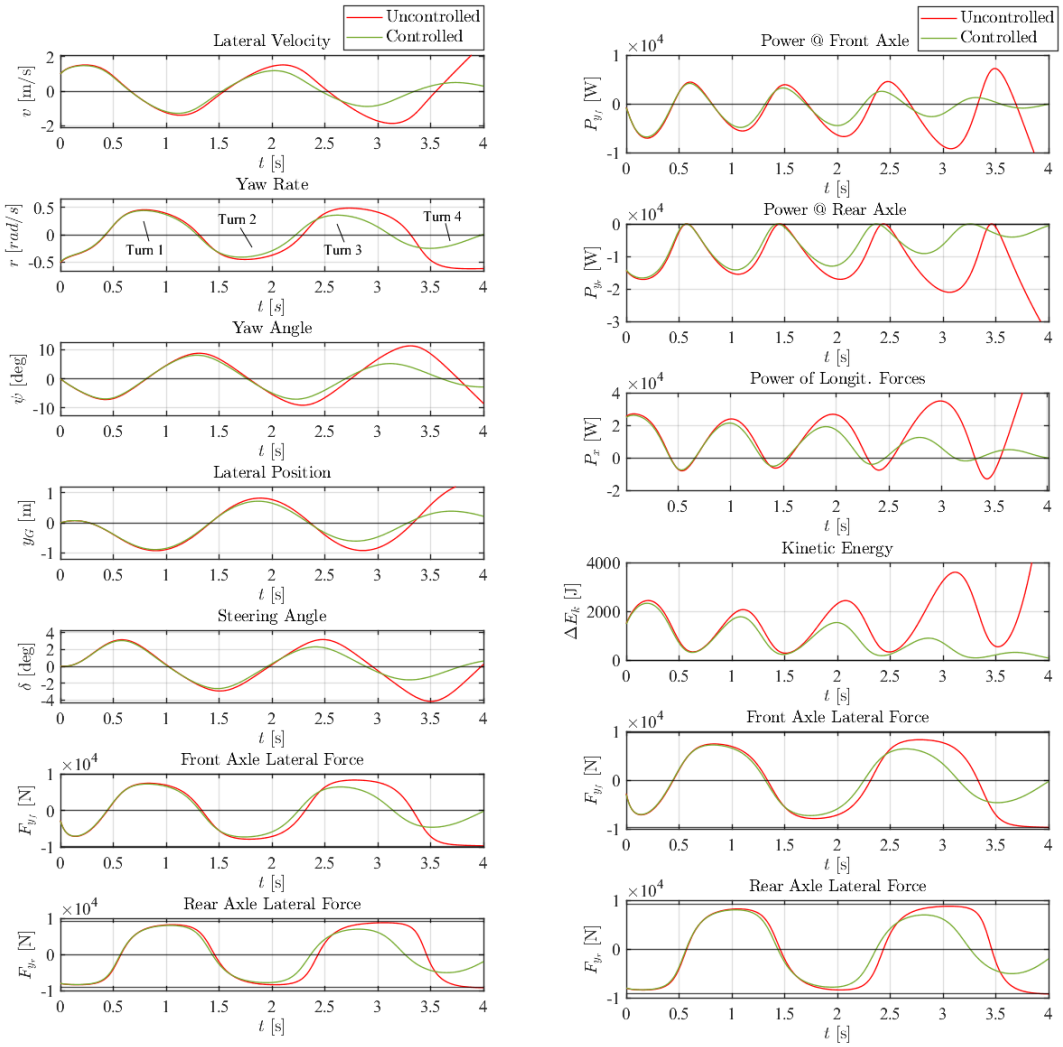

Figure 5.6: State variables, axle lateral forces and powers.

To obtain more conclusive results, the analysis should be repeated considering the vehicle running along a bend. Indeed, the theory developed in [3] was originally intended to classify the kinematic behaviour of the vehicle as either "good" or "bad" when negotiating a corner, even more so without factoring in the action of a disturbance which provokes oscillations around the desired trajectory. The application of these concepts to study the disturbed rectilinear motion might be quite forced, considering that the lateral motion and the yaw rotation are merely consequences of the disturbance rather than a voluntary action of the driver that wants to steer the vehicle into a proper turn. A more refined study is also needed to precisely understand how the instability occurs from an energy standpoint.

6 | Floquet Theory

In the previous chapter, we gave some insights into how an unstable motion may be characterized from a kinematic/energy standpoint. Still, in the present work we were not able to define a precise criterion to recognize as soon as the disturbance has acted whether the system is evolving towards an unstable condition. Moreover, while at this stage it should be evident that the saddle-type limit cycle plays a fundamental role in defining the basin of attraction of stable equilibria of the vehicle-and-driver system, a formal proof of how the motion becomes unstable in the neighbourhood of the cycle has not been given yet. In the following, we propose a novel methodology for vehicle stability sensing based on the mathematical analysis of trajectories near the saddle-type limit cycle, addressing both issues.

6.1. Introductory Example

To understand the fundamentals of the method, it might be beneficial to refer to a much simpler scenario. Let us then consider a two-dimensional dynamical system which has one saddle equilibrium and one stable node or focus as minimum requirements. The phase portrait for one such system is visible in Fig. 6.1; it has one saddle equilibrium at (1, 1), one unstable node at (0, 0) and two stable nodes at (0, 2) and (3, 0) respectively.

The trajectories which constitute the stable and unstable manifolds of the saddle equilibrium are also visible in Fig. 6.1. The two manifolds are commonly called *separatrices*, since they divide the phase space into independent sectors. Referring again to Fig. 6.1, it is perhaps easy to perceive that orbits contained in the rightmost region of the phase plane with respect to the stable manifold converge to the stable node in (3, 0), while orbits to the left of the stable manifold converge to the stable node in (0, 2), which for the sake of argument will be regarded as an unstable solution. Given a generic point $\bar{\boldsymbol{z}}$ in the phase plane, a necessary and sufficient condition for asymptotic stability can then be formulated considering the relative position between $\bar{\boldsymbol{z}}$ and the stable manifold of the saddle.

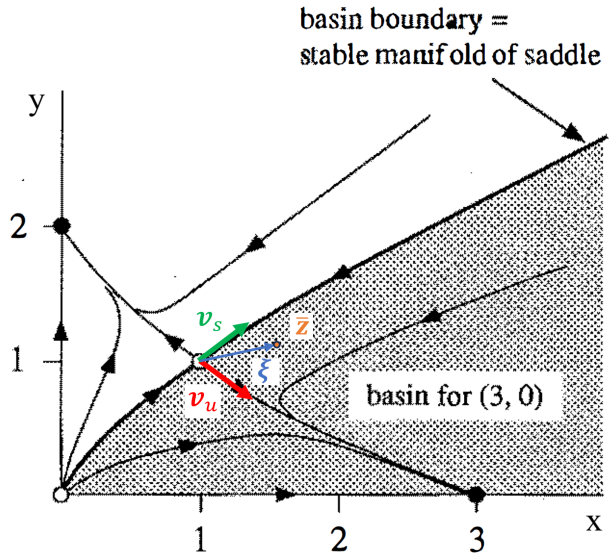

Figure 6.1: Phase portrait of a simple 2D system in the neighbourhood of a saddle equilibrium. The eigenvectors of the system at the saddle point are highlighted ($\boldsymbol{v}_s$: stable, $\boldsymbol{v}_r$: unstable); they locally approximate the corresponding manifolds of the saddle. Adapted from [7].

But how can this position be defined in practice? The most basic information needed are obviously the coordinates of the saddle and of the stable equilibrium in the phase plane. Next, it is necessary to introduce one important concept related to the manifolds of saddle-type equilibria of a dynamical system: the stable (resp. unstable) manifold is always tangent to the stable (resp. unstable) eigenspace of the system linearized at the saddle equilibrium [5]. The linear approximation of each manifold is therefore the hyperplane defined by the corresponding eigenvectors. In the simple case considered, the saddle is two-dimensional and therefore both of its manifolds are necessarily one-dimensional (one eigenvalue of the system linearized about the saddle point is stable, the other is unstable). The stable ($\boldsymbol{v}_s$) and unstable ($\boldsymbol{v}_u$) eigenvector are visualized in Fig. 6.1 in green and in red respectively. It is important for our analysis that the unstable eigenvector is oriented towards the stable equilibrium; fixing the direction of the stable eigenvector is instead not relevant.

Since different eigenvalues correspond to different eigenvectors, the latter are linearly independent and thus define a basis in the phase space. The position of a generic point $\bar{\boldsymbol{z}}$ in the phase space relative to the saddle separatrices can be evaluated by computing the deviation $\boldsymbol{\xi}$ from the saddle and expressing it in this eigenbasis, since the separatrices are locally approximated by the corresponding eigenvector. The decomposition of $\boldsymbol{\xi}$ for the

considered 2D system reads:

$$\boldsymbol{\xi} = c_s \boldsymbol{v}_s + c_u \boldsymbol{v}_u$$

where c_s, $c_u \in \mathbb{R}$. The necessary and sufficient condition for asymptotic stability is $c_u > 0$, i.e. the coefficient that multiplies the unstable eigenvector must be positive. The unstable eigenvector is indeed oriented towards the stable equilibrium: only in this case the orbit passing through $\bar{\boldsymbol{z}}$ moves away from the saddle along the "correct" direction, ultimately converging to the stable equilibrium. It is important to note that for a nonlinear system this condition is only rigorously valid if the initial state $\bar{\boldsymbol{z}}$ is near the saddle equilibrium, since the curvature of the manifolds is not accounted for.

The whole described procedure is still valid, with some variations, also when the saddle equilibrium is substituted by a saddle-type limit cycle. The upcoming sections of this chapter will be dedicated to applying the introduced notions to the global stability analysis of road vehicles, exploiting the main results of Floquet theory. As always, we will not delve into the more theoretical aspects of the covered topics, which the interested reader can find in [6, 31].

6.2. Variational Equation

As stated in Section 6.1, exploiting the properties of the saddle separatrices to quickly understand if a disturbance can lead to an unstable motion requires knowing the coordinates of the saddle itself in the phase space. Likewise, the procedure illustrated in the following is only viable if the periodic solution that describes the motion of the system along the saddle-type limit cycle is known. This could represent one of the main limitations of this method, since a numerical model which completely describes the dynamics of the physical, real-life model (a *digital twin*) is not always available, not to mention the complexity involved in accurately reproducing the driver's action. Nonetheless, this procedure still remains significant especially in the context of motorsport applications, where a fairly complete characterization of vehicle and driver is generally possible with the aid of a driving simulator.

The first step of the analysis is to linearize the equations of motion of the vehicle-and-driver system in the neighbourhood of the limit cycle, exactly as one would proceed if the cycle were an equilibrium point. At the moment, it is irrelevant to the treatment that the limit cycle is of the saddle-type. Indeed, the stability of the cycle will be assessed during the analysis itself. Considering an n-dimensional system, let $\boldsymbol{z}(t) \in \mathbb{R}^n$ denote a generic orbit in the neighbourhood of a limit cycle represented by the T-periodic solution $\boldsymbol{z}_0(t) \in \mathbb{R}^n$: $\boldsymbol{z}_0(t+T) = \boldsymbol{z}_0(t)$. Considering a small deviation $\boldsymbol{\xi}(t) \in \mathbb{R}^n$ from the periodic

solution, we can write:

$$\boldsymbol{z}(t) = \boldsymbol{z}_0(t) + \boldsymbol{\xi}(t)$$

The first-order Taylor expansion of the system about $\boldsymbol{z}_0(t)$ then yields:

$$\dot{\boldsymbol{\xi}}(t) = \boldsymbol{A}(t)\boldsymbol{\xi}(t) \tag{6.1}$$

where $\boldsymbol{A}(t)$ is the T-periodic Jacobian of the system, computed in $\boldsymbol{z}_0(t)$: $\boldsymbol{A}(t+T) = \boldsymbol{A}(t)$. Eq. (6.1) is called the *variational equation* about the limit cycle and governs the evolution of perturbations near the cycle, assuming that the effect of higher order terms can be neglected.

The variational equation admits n linearly independent solutions $\boldsymbol{\xi}^{(i)}(t)$: every other solution to the system can be written as a linear combination of these fundamental solutions. Introducing the time-dependent $n \times n$ matrix $\boldsymbol{\phi}(t)$ whose n columns are the *fundamental solutions* to the variational equation:

$$\boldsymbol{\phi}(t) = \begin{bmatrix} \boldsymbol{\xi}^{(1)}(t) & \boldsymbol{\xi}^{(2)}(t) & \dots & \boldsymbol{\xi}^{(n)}(t) \end{bmatrix}$$

we can then write:

$$\boldsymbol{\xi}(t) = \boldsymbol{\phi}(t)c$$

where c is some constant $n \times 1$ vector. One can easily verify that the matrix $\boldsymbol{\phi}(t)$, which is traditionally called the *fundamental matrix* of Eq. (6.1), satisfies the following differential equation:

$$\dot{\boldsymbol{\phi}}(t) = \boldsymbol{A}(t)\boldsymbol{\phi}(t) \tag{6.2}$$

To ensure that the columns of $\boldsymbol{\phi}(t)$ are linearly independent, we can set:

$$\boldsymbol{\phi}(0) = \begin{bmatrix} \xi_1^{(1)}(0) & 0 & \dots & 0 \\ 0 & \xi_2^{(2)}(0) & \dots & 0 \\ \vdots & \vdots & \ddots & \vdots \\ 0 & 0 & \dots & \xi_n^{(n)}(0) \end{bmatrix}$$

where $\xi_i^{(j)}(0)$ is an arbitrarily selected small initial deviation with respect to the periodic orbit, imposed on the i-th state variable of the j-th fundamental solution ($\boldsymbol{\phi}_{i,j}(0) = 0$ only if $i \neq j$). To numerically integrate Eq. (6.2), we first need to manipulate it as numerical solvers usually work with state vectors rather than state matrices. The equation can be

rewritten as:

$$\begin{Bmatrix} \dot{\boldsymbol{\xi}}^{(1)}(t) \\ \dot{\boldsymbol{\xi}}^{(2)}(t) \\ \vdots \\ \dot{\boldsymbol{\xi}}^{(n)}(t) \end{Bmatrix} = \begin{bmatrix} \boldsymbol{A}(t) & 0 & \dots & 0 \\ 0 & \boldsymbol{A}(t) & \dots & 0 \\ \vdots & \vdots & \ddots & \vdots \\ 0 & 0 & \dots & \boldsymbol{A}(t) \end{bmatrix} \begin{Bmatrix} \boldsymbol{\xi}^{(1)}(t) \\ \boldsymbol{\xi}^{(2)}(t) \\ \vdots \\ \boldsymbol{\xi}^{(n)}(t) \end{Bmatrix} \tag{6.3}$$

The fundamental matrix $\boldsymbol{\phi}(t)$ is the central element of *Floquet theory*, which will be introduced in the next subsection.

6.3. Limit Cycle Stability

Were the analysis focused on an equilibrium point of an n-dimensional system, the next stage after the linearization of the system around the equilibrium would be to compute the n eigenvectors and eigenvalues of the (constant) Jacobian matrix. The evolution of any small deviation $\boldsymbol{\xi}(t)$ with respect to the equilibrium point would then be (approximately) described by:

$$\boldsymbol{\xi}(t) = \alpha_1 \boldsymbol{v_1} e^{\lambda_1 t} + \alpha_2 \boldsymbol{v_2} e^{\lambda_2 t} + ... + \alpha_n \boldsymbol{v_n} e^{\lambda_n t} \tag{6.4}$$

where $\boldsymbol{v}_1$, $\boldsymbol{v}_2$, ..., $\boldsymbol{v}_n \in \mathbb{C}^n$ are the eigenvectors that correspond to the eigenvalues λ_1, λ_2, ..., $\lambda_n \in \mathbb{C}$, and the coefficients α_1, α_2, ..., $\alpha_n \in \mathbb{C}$ depend on the initial deviation $\boldsymbol{\xi}(0)$. We are interested in translating this notion from equilibrium points to limit cycles. To clarify, in this initial stage of the analysis we want to find a set of possibly complex fundamental solutions to Eq. (6.1) in the form:

$$\boldsymbol{\xi}^{(i)}(t) = \boldsymbol{p}_i(t) e^{k_i t} \tag{6.5}$$

for $i = \{1,\ 2, ...,\ n\}$, where $\boldsymbol{p}_i(t) \in \mathbb{C}^n$ and $k_i \in \mathbb{C}$. This is indeed possible, following the main results of *Floquet theory* [31]. The theory gives a canonical form for each fundamental solution of linear systems of differential equations with periodic coefficients. The variational equation (6.1) belongs to the same family of differential equations, therefore the potential of Floquet theory can be exploited to the fullest in the present analysis.

Floquet's theorem states that if $\boldsymbol{\phi}(t)$ is a fundamental matrix solution of the T-periodic system (6.1), there is a possibly complex $n \times n$ constant matrix $\boldsymbol{B}$ such that:

$$e^{T\boldsymbol{B}} = \boldsymbol{\phi}^{-1}(0)\boldsymbol{\phi}(T) = \boldsymbol{M}(T) \tag{6.6}$$

Moreover, there is a possibly complex T-periodic $n \times n$ matrix $\boldsymbol{P}(t)$ such that:

$$\boldsymbol{\phi}(t) = \boldsymbol{P}(t)e^{t\boldsymbol{B}} \tag{6.7}$$

for all $t \in \mathbb{R}$. Eq. (6.7) represents the *Floquet normal form* of the fundamental matrix $\boldsymbol{\phi}(t)$. The $n \times n$ matrix $\boldsymbol{M}(T)$ is instead called the *monodromy matrix* of the limit cycle.

If the Jacobian $\boldsymbol{A}(t)$ is known at each point of the limit cycle, Eq. (6.3) can be numerically integrated over one period T to obtain $\boldsymbol{\phi}(t)$ and, in particular, the monodromy matrix $\boldsymbol{M}(T)$. Now, Eq. (6.6) can be used to compute the matrix $\boldsymbol{B}$, which is finally plugged into Eq. (6.7) to obtain $\boldsymbol{P}(t)$. We have therefore decomposed the fundamental matrix into a periodic part ($\boldsymbol{P}(t)$) and an exponential part ($e^{t\boldsymbol{B}}$).

The eigenvalues and eigenvectors of the monodromy matrix $\boldsymbol{M}(T)$ are the key missing elements to achieve expression (6.5). A fundamental result of Floquet theory states that for each eigenvalue m_i of $\boldsymbol{M}(T)$ there exists a possibly complex, nontrivial solution to Eq. (6.1) of the form:

$$\boldsymbol{\xi}^{(i)}(t) = \boldsymbol{P}(t)\boldsymbol{v}_i e^{k_i t} = \boldsymbol{p}_i(t)e^{k_i t} \tag{6.8}$$

where $\boldsymbol{v}_i$ is the eigenvector of $\boldsymbol{M}(T)$ that corresponds to the eigenvalue m_i. Moreover, m_i satisfies the relation:

$$m_i = e^{k_i T} \tag{6.9}$$

Solutions of the form (6.8) computed for different m_i are linearly independent, therefore they constitute a set of n fundamental solutions for the variational equation (6.1). The complete expression of a deviation $\boldsymbol{\xi}(t)$ from the periodic solution $\boldsymbol{z}_0(t)$ can thus finally be written as:

$$\boldsymbol{\xi}(t) = \sum_{i=1}^{n} \alpha_i \boldsymbol{\xi}^{(i)}(t) = \alpha_1 \boldsymbol{P}(t)\boldsymbol{v}_1 e^{k_1 t} + \alpha_2 \boldsymbol{P}(t)\boldsymbol{v}_2 e^{k_2 t} + ... + \alpha_n \boldsymbol{P}(t)\boldsymbol{v}_n e^{k_n t} \tag{6.10}$$

where $\alpha_1, \alpha_2, ..., \alpha_n \in \mathbb{C}$ depend on the initial deviation $\boldsymbol{\xi}(0)$. $k_1, k_2, ..., k_n \in \mathbb{C}$ are called *Floquet exponents* and determine the stability of the limit cycle. For example, if the limit cycle is unstable, nearby trajectories will be repelled, so that $\lim_{t\to\infty} \boldsymbol{\xi}(t) = \infty$. This condition requires that at least one of the exponential functions in Eq. (6.10) grows indefinitely, since $\boldsymbol{P}(t)$ is periodic and therefore bounded. A limit cycle is thus unstable if $\Re(k_i) > 0$ is verified for at least one of the Floquet exponents. If an unstable cycle also has one or more Floquet exponents with negative real part, the cycle is of the saddle type: orbits of the stable manifold will be attracted to the cycle, those of the unstable manifold repelled by it, analogously to what occurs for a saddle equilibrium point. The eigenvalues

m_i of the monodromy matrix $\boldsymbol{M}(T)$ are called *characteristic multipliers*. From Eq. (6.9) it follows that the cycle is unstable if $|m_i| > 1$ is satisfied for at least one multiplier. The cycle will always possess a unit multiplier (equivalent to a null Floquet exponent), representing initial deviations tangent to the cycle: the eigenvector associated to the unit multiplier is in fact tangent to the cycle at $\boldsymbol{z}_0(0) = \boldsymbol{z}_0(T)$.

At this stage, one question may arise: which point of the cycle should be chosen as the initial point $\boldsymbol{z}_0(0)$? This is not an issue when linearizing the system around an equilibrium, that is a single point fixed in the phase space. While different choices of $\boldsymbol{z}_0(0)$ correspond to different monodromy matrices $\boldsymbol{M}(T)$, it can be shown that all these matrices share the same characteristic multipliers: the selection of the initial cycle point is therefore irrelevant if the only purpose of the analysis is to evaluate the stability of the limit cycle.

6.4. Real-Time Stability Assessment of Vehicle-and-Driver Motion

With the aid of Floquet theory, we were able to decompose a deviation $\boldsymbol{\xi}(t)$ from the periodic solution $\boldsymbol{z}_0(t)$ into the linear combination of n eigenfunctions $\boldsymbol{p}_i(t)$, each scaled by an exponential function whose growth or decay is controlled by the respective Floquet exponent k_i. Such expression was then used to evaluate the stability of the limit cycle. Floquet theory also provides the essential instruments to derive a necessary and sufficient condition to assess whether motions close to a saddle-type limit cycle will converge to a stable equilibrium or diverge towards a spin condition. Remembering the 2D example presented in Section 6.1, what remains lacking in this case is a method for computing the position of orbits relative to the stable and unstable manifolds of the cycle, using the deviation $\boldsymbol{\xi}(t)$. Fortunately, the complexity of the problem can be reduced by essentially working on cross-sections of the cycle instead of considering the entire manifolds: by resorting to Poincarè maps constructed along the cycle, it is possible to refer again to the analysis of trajectories near a saddle equilibrium point.

Poincarè maps [5] for n-dimensional systems are typically defined on $(n-1)$-dimensional hypersurfaces orthogonal to a trajectory in the phase space, and they trace the intersection points of the trajectory with said hypersurface. Let us consider instead a *stroboscopic* Poincarè map in $\mathbb{R}^n$ for the variational equation (6.1), i.e. a map $\boldsymbol{\xi} \mapsto \tilde{\boldsymbol{\xi}} = \boldsymbol{P}_m(\boldsymbol{\xi})$ that traces the evolution of an initial deviation $\boldsymbol{\xi} \in \mathbb{R}^n$ at integer multiples of the period T of the cycle. In essence, the map moves $\boldsymbol{\xi}$ forward in time over one period of the cycle at each iteration. Fig. 6.2 is the graphical interpretation of this concept.

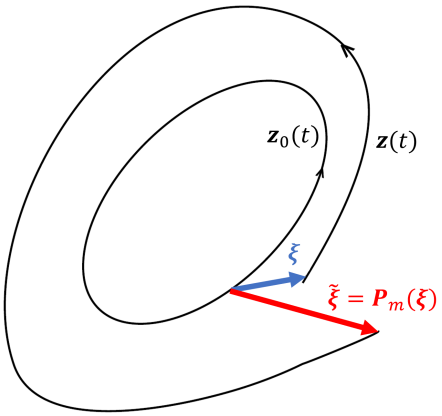

Figure 6.2: Geometrical meaning of the stroboscopic Poincarè map (monodromy operator). The map sends the deviation vector ($\boldsymbol{\xi}$) of the orbit ($\boldsymbol{z}$) from the cycle ($\boldsymbol{z}_0$) forward in time by one period T. Adapted from [32].

The monodromy operator

$$\boldsymbol{\xi} \mapsto \tilde{\boldsymbol{\xi}} = \boldsymbol{P}_m(\boldsymbol{\xi}) = \boldsymbol{\phi}(T)\boldsymbol{\phi}^{-1}(0)\boldsymbol{\xi} \tag{6.11}$$

is a stroboscopic Poincarè map for system (6.1) [31]. Since the fundamental matrix $\boldsymbol{\phi}(T)$ depends on the initial cycle point $\boldsymbol{z}_0(0)$ selected to start the integration of Eq. (6.3), different maps are obtained for different $\boldsymbol{z}_0(0)$. The initial cycle point $\boldsymbol{z}_0(0)$ is also the only fixed point of the map: from (6.11) we obtain $\boldsymbol{P}_m(\mathbf{0}) = \mathbf{0}$. If the cycle is stable, all neighbouring orbits will converge to the cycle as t increases, so that any small initial deviation $\boldsymbol{\xi}(0)$ from the cycle will eventually vanish after successive iterations of the Poincarè map; the opposite can instead be observed for an unstable cycle. If the cycle is of the saddle type, trajectories that belong to the stable (resp. unstable) manifold will converge to the cycle for $t \to \infty$ (resp. $t \to -\infty$). Analogously, the fixed point $\boldsymbol{z}_0(0)$ of the Poincarè map is a saddle with an unstable manifold and a stable manifold, i.e. the separatrices of the saddle.

The initial problem was thus successfully reduced to the more simple analysis of trajectories in the neighbourhood of a saddle fixed point, which was already tackled in Sect. 6.1: given a point $\bar{\boldsymbol{z}}$ in the phase space and a suitable cycle point $\bar{\boldsymbol{z}}_0$, by expressing the deviation $\bar{\boldsymbol{\xi}} = \bar{\boldsymbol{z}} - \bar{\boldsymbol{z}}_0$ in the basis of $\mathbb{R}^n$ formed by the eigenvectors of the map (6.11), it is possible to evaluate whether the orbit $\boldsymbol{z}(t)$ passing through $\bar{\boldsymbol{z}}$ is moving away from the saddle-type limit cycle in the "correct" direction, i.e. towards the stable equilibrium of the system (assuming that $\bar{\boldsymbol{\xi}}$ is sufficiently small to neglect the curvature of the separatrices). The only differences are that we are now considering an n-dimensional, discrete-time sys-

tem instead of a two-dimensional, continuous-time system, and that we need to select $\bar{\boldsymbol{z}}_0$ among a set of available cycle points.

The higher dimensionality could represent a problem, since if the unstable eigenspace of the saddle is spanned by complex conjugate eigenvectors only, orbits of the unstable manifold leave the fixed point of the map in an oscillatory manner instead of being organized into sectors as in Fig. 6.1. This could not have occurred for a two-dimensional saddle, given that the unstable eigenspace is necessarily one-dimensional and thus always spanned by one real eigenvector. Although this will not pose an issue for the simple vehicle-and-driver model utilized in the present work, it is important to consider this possible limitation when extending the analysis to more complex models.

6.4.1. Stability Criterion

Once the necessary theory has been covered, we can finally transition to the more practical phase in which a methodology to sense the imminent loss of vehicle control during the maneuver is derived. Let us start by considering the vehicle being driven at constant forward speed, maintaining a stable steady-state condition. Suppose also that the large motion of vehicle-and-driver is characterized by the presence of a saddle-type limit cycle which surrounds the equilibrium point; it does not matter whether the driver is following a rectilinear or circular trajectory. Keeping all the system parameters fixed (including the forward speed), let us perturb the system. The driver will try to return to the desired trajectory, tracing an orbit in the phase space described by the state vector $\boldsymbol{z}(t)$; the origin of the disturbance is not relevant for the present analysis, i.e. no restriction is posed on which state variables can be affected by the disturbance. Assuming that all the state variables of the system can either be directly measured or estimated and considering a reasonable sampling rate (e.g. $\Delta f = 100$ Hz), $\boldsymbol{z}(t)$ is known at each instant t during the motion. As commented in the previous sections, knowing the coordinates of individual points that belong to the limit cycle is a fundamental requirement to apply Floquet theory, which may limit the versatility of the methodology here introduced. In particular, to integrate the variational equation (6.3), it is necessary to compute the Jacobian $\boldsymbol{A}(t)$ at each point of the cycle, either analytically or numerically. The points considered should be spaced along the cycle at time intervals that are preferably equal to or smaller than $1/\Delta f$ and must complete the closed orbit.

Once all the fundamental elements have been laid out, we can begin formulating a criterion for asymptotic stability, segmenting the process into stages and describing the main issues that need to be tackled within each:

1. The assessment of stability is based on the construction of a stroboscopic Poincarè map corresponding to one point of the cycle, using the monodromy operator (6.11). A point $\bar{\boldsymbol{z}}_0$ must therefore appropriately be selected along the cycle at each instant during the motion of vehicle-and-driver, used both to compute the current deviation $\bar{\boldsymbol{\xi}}$ and to construct the monodromy operator ($\boldsymbol{\phi}(T)$ depends on the initial cycle point used to start the integration of (6.2));

2. The variational equation (6.1) was obtained by linearizing the vehicle-and-driver system in the neighbourhood of the periodic solution, therefore it does not approximate well the behaviour of the system at a considerable distance from the cycle. The trajectory of the system in the phase space during a maneuver is, in general, not in the immediate proximity of the cycle. Indeed, if the disturbance is quite strong the motion may even be completely unaffected by the underlying presence of the cycle, as the driver immediately loses control of the vehicle. A criterion to establish when it is meaningful to proceed with the assessment is therefore needed;

3. If it is detected that the motion of vehicle-and-driver is being influenced by the limit cycle, the current deviation $\bar{\boldsymbol{\xi}}$, computed referring to the cycle point $\bar{\boldsymbol{z}}_0$ identified at stage 1, can meaningfully be expressed in the eigenbasis of the Poincarè map to assess whether the orbit is leaving the saddle-type limit cycle towards the stable equilibrium or towards a spin.

Stages 1 and 2 are the most intricate: while the actual projection of the deviation $\bar{\boldsymbol{\xi}}$ in the eigenbasis of the Poincarè map (stage 3) has a sound theoretical background, which was covered in the previous sections, the criteria introduced in the following to determine *where* (with respect to which cycle point) and *when* (considering the proximity to the cycle) to compute the projection are mainly based on heuristic reasoning.

Since Eq. (6.1) is valid locally, i.e. for *small* deviations $\boldsymbol{\xi}$ from the cycle, one may be tempted to simply use the distance from the cycle itself to answer both the *where* (stage 1: select the cycle point that minimizes the distance from the current orbit point) and the *when* (stage 2: proceed if said distance becomes less than a specified threshold). This strategy is in general not the most ideal. Consider for instance the orbit portrayed in Fig. 4.10a. The orbit represents the perturbed motion of the vehicle-and-driver system around a steady-state cornering condition after the action of a disturbance. Please notice how in this case the cycle is "skewed", in the sense that the stable equilibrium does not lie in a central position with respect to the cycle. Neighbouring trajectories that converge to the equilibrium will then result closer to one side of the cycle, and this could negatively impact the selection of the cycle point used to construct the Poincarè map if the criterion is based

solely on minimizing the distance. For stage 2, considering a threshold on the maximum allowed deviation from the cycle to ascertain that the projection on the eigenbasis is only performed when the linear approximation of the system is rigorously valid presents no issues instead, at least in a theoretical framework. Operationally, implementing this strategy could be overly restrictive, in the sense that we would be able to infer the stability of the motion only for a limited set of perturbations distributed near the stable manifold of the saddle-type limit cycle, i.e. when the orbit nearly coincides with the cycle. In substance, the aim is to define a method that is accurate in defining the stability threshold, but also applicable to a relatively wide range of scenarios. Achieving this compromise is especially relevant when the system operates closer to the Hopf bifurcation point, for example when driving at higher speeds. Indeed, it was seen in Sections 4.2.1 and 4.2.2 how under these circumstances the borders of the Milliken diagram do not approximate well the ISMaVeR, with the loss of vehicle control being observed for disturbances that initially load the tyres well below their saturation limit. It is therefore of interest to provide a method that can detect an unstable condition at least until tyre saturation, in all circumstances.

Stage 1 - Selection of Cycle Point

Let us consider a set of N cycle points $\boldsymbol{z}_0^{(i)}$, $i = 1, ..., N$, and assume that the motion of vehicle-and-driver is being described by the state vector $\boldsymbol{z}(t)$. At each instant t, $\bar{\boldsymbol{z}}_0$ can be selected to be the solution of the following constrained maximization problem:

$$\begin{aligned} \max_{\boldsymbol{z}_0^{(i)}} \quad & f_{obj} = (1-w)DP[\boldsymbol{z}_0^{(i)}] + w\frac{D_{min}}{D[\boldsymbol{z}_0^{(i)}]} \\ \text{s.t.} \quad & DP[\boldsymbol{z}_0^{(i)}] > 0 \end{aligned} \tag{6.12}$$

with:

$$DP[\boldsymbol{z}_0^{(i)}] = \frac{\dot{\boldsymbol{z}}_0^{(i)} \cdot \dot{\boldsymbol{z}}}{\|\dot{\boldsymbol{z}}_0^{(i)}\| \, \|\dot{\boldsymbol{z}}\|},$$
$$\frac{D_{min}}{D[\boldsymbol{z}_0^{(i)}]} = \frac{\|\boldsymbol{z} - \boldsymbol{z}_0^{(i)}\|_{min}}{\|\boldsymbol{z} - \boldsymbol{z}_0^{(i)}\|}$$

where:

- "$\|\cdot\|$" indicates the vector norm;
- "$\cdot$" indicates the dot product of vectors;
- $\dot{\boldsymbol{z}}_0^{(i)}$, $\dot{\boldsymbol{z}}$ are respectively the vector tangent to the cycle at point $\boldsymbol{z}_0^{(i)}$ and the vector

tangent to the orbit at the current state $\boldsymbol{z}$;

- w is a constant weighting factor;
- D_{min} is the minimum distance between the orbit and the cycle.

The problem is easily solved by first checking the constraint on the normalized dot product $DP[\boldsymbol{z}_0^{(i)}]$ in correspondence of every available cycle point $\boldsymbol{z}_0^{(i)}$. Then, the distance $D[\boldsymbol{z}_0^{(i)}]$ is computed for each $\boldsymbol{z}_0^{(i)}$ that satisfies the constraint, and the minimum value D_{min} is identified. Finally, the objective function f_{obj} is computed and the cycle point $\bar{\boldsymbol{z}}_0$ which maximizes it at the current time instant can be identified. Prior to starting any of the above computations, each state variable is always normalized with respect to its maximum absolute value observed along the limit cycle; the same values are also used to normalize the derivative of the corresponding variable. We will refer to the phase space obtained through this coordinate transformation as *normalized phase space*. Working in the normalized phase space ensures that the above computations are not biased towards any state variable in particular, given that each of them has a different scale.

The formulation of (6.12) comes from observing that orbits near the limit cycle resemble the overall shape of the cycle (they are nearly concentric to it, see for example Figures 4.10a and 5.4): the cycle point $\bar{\boldsymbol{z}}_0$ that corresponds to the current orbit point (i.e. the most suitable for the construction of the Poincarè map and the computation of $\bar{\boldsymbol{\xi}}$) can be obtained by finding the best compromise between collinearity of tangent vectors (DP) and minimum distance (D). This compromise is regulated by the weighting factor w.

Stage 2 - Set Trigger Point for Decomposition

The collinearity between tangent vectors is also considered to understand whether it is meaningful to actually proceed with the decomposition of the deviation $\bar{\boldsymbol{\xi}}$. One can indeed infer that the motion of the system is being significantly influenced by the underlying presence of the cycle (i.e. the orbit is approaching the cycle) when $DP[\bar{\boldsymbol{z}}_0]$ settles to a near-unit value. In practice, this condition can be checked over a time window of specified length l, which collects the values of the dot product $DP[\bar{\boldsymbol{z}}_0(t_j)]$ computed for the latest l instants ($j = 1, 2, ..., l$), considering each time the cycle point $\bar{\boldsymbol{z}}_0(t_j)$ obtained by initially solving (6.12). The point $\bar{\boldsymbol{z}}_0(t_l)$ at the current time instant is utilized to construct the Poincarè map (6.11) only if

$$\begin{cases} DP[\bar{\boldsymbol{z}}_0(t_j)] > DP_{thr} \\ D[\bar{\boldsymbol{z}}_0(t_j)] < D_{thr} \end{cases} \quad \forall\ j = 1, 2, ..., l \tag{6.13}$$

where $DP_{thr} \sim 1$ ($DP_{thr} < 1$) and D_{thr} are specified thresholds. D_{thr} can be defined as a percentage of the cycle amplitude computed in the normalized phase space; it guarantees that the projection of the deviation $\bar{\boldsymbol{\xi}}$ on the eigenbasis of the map is not performed when the trajectory of the system is excessively far from the cycle, considering that the linear approximation of the saddle manifolds could lead to substantial errors in such cases.

Stage 3 - Decomposition

Let us assume that (6.13) is met at a certain time instant $\bar{t}$ during the motion of vehicle-and-driver, when the system state is represented by the vector $\bar{\boldsymbol{z}} = \boldsymbol{z}(\bar{t})$. We finally need to express the current deviation $\bar{\boldsymbol{\xi}} = \bar{\boldsymbol{z}} - \bar{\boldsymbol{z}}_0(\bar{t})$, computed without any normalization, in the basis of $\mathbb{R}^n$ formed by the unit eigenvectors $\boldsymbol{v}_1,\ \boldsymbol{v}_2, ...,\ \boldsymbol{v}_n \in \mathbb{C}^n$ of the Poincarè map (6.11), constructed by integrating (6.2) over one period of the cycle starting from $\bar{\boldsymbol{z}}_0(\bar{t})$ (rephrased $\bar{\boldsymbol{z}}_0$ for ease of reading). Since the computation of the map itself does not rely on any information about the orbit being traced during the maneuver, the map obtained starting from each available cycle point $\boldsymbol{z}_0^{(i)}$ can also be pre-computed at the very beginning of the analysis. If this were the case, only the actual projection of $\bar{\boldsymbol{\xi}}$ in the eigenbasis of the map that corresponds to $\bar{\boldsymbol{z}}_0$ would need to be carried out during stage 3. This would certainly constitute an advantage since it removes the numerical burden of a real-time integration, although computing the map for each cycle point may be overly time consuming.

Regardless of how the Poincarè map is obtained, expressing the deviation $\bar{\boldsymbol{\xi}}$ in the eigenbasis of the map means finding a column vector of constant values $\boldsymbol{c} = \{c_1,\ c_2, ...,\ c_n\}^{\mathrm{T}} \in \mathbb{C}^n$ which solves the following linear system:

$$\begin{aligned} \bar{\boldsymbol{\xi}} &= c_1\boldsymbol{v}_1 + c_2\boldsymbol{v}_2 + ... + c_n\boldsymbol{v}_n \\ &= [\boldsymbol{v}_1,\ \boldsymbol{v}_2, ...,\ \boldsymbol{v}_n]\,\boldsymbol{c} \\ &= \boldsymbol{V}\boldsymbol{c} \end{aligned} \tag{6.14}$$

In case the map possesses only one real unstable eigenvector $\boldsymbol{v}_u$, the necessary and sufficient condition for asymptotic stability is

$$c_u > 0$$

provided that the direction of $\boldsymbol{v}_u$ is chosen so that c_u is positive when projecting the vector $\boldsymbol{\xi}_E = \boldsymbol{z}_E - \bar{\boldsymbol{z}}_0$ onto the eigenbasis, with $\boldsymbol{z}_E$ being the stable equilibrium of the system. If $c_u < 0$, the orbit will instead be repelled away from the cycle towards a spin condition. If

$c_u = 0$, the orbit belongs to the stable manifold of the cycle and will ultimately converge to the periodic solution;

The saddle-type limit cycles observed for the simple vehicle-and-driver model considered throughout the present work indeed feature only one real positive Floquet exponent, therefore the Poincarè map always has only one real unstable eigenvector. It should be noted that in general if a cycle has n_+ stable exponents and n_- unstable exponents, the dimensions of its stable and unstable manifolds will respectively be $(n_+ + 1)$ and $(n_- + 1)$. Saddle-type cycles of the simple 7D vehicle-and-driver model therefore have a 6D stable manifold and a 2D unstable manifold, whose intersection is the cycle itself (hence the unit multiplier).

Table 6.1 collects the values of the parameters introduced in stages 1 and 2 that will be considered in the present work to test the Floquet theory-based stability criterion; the most important parameters are the dot product threshold DP_{thr} and the window length l, both utilized at stage 2. Increasing DP_{thr} and/or l provides a more accurate stability evaluation, but also reduces the flexibility of the criterion: unstable motions that do not follow well the shape of the cycle will not be captured. Fig. 6.3 shows examples of how the stability criterion is used to recognize stable and unstable motions.

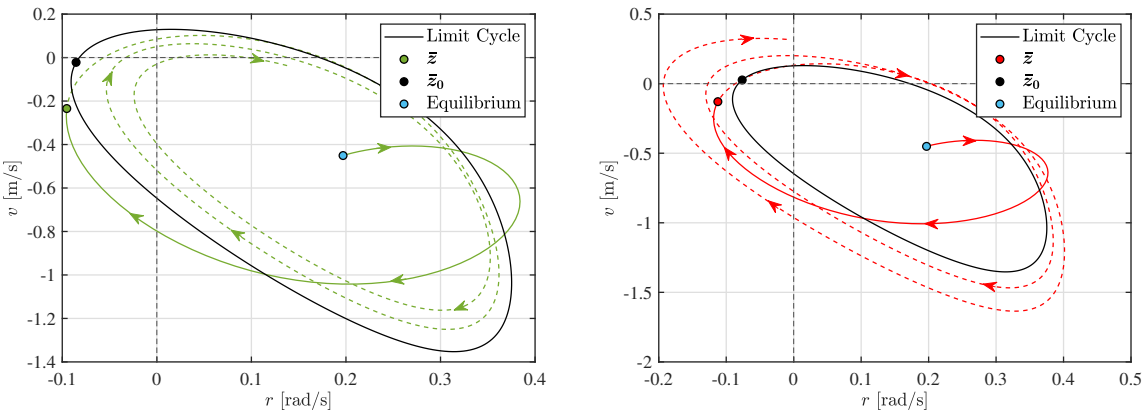

(a) Disturbance: $(\dot{\delta}, d_G) = (20\,\text{deg/s}, -0.1\,\text{m})$; stability detected at $t = 0.75\,\text{s}$ with coefficient $c_u = 0.074$.

(b) Disturbance: $(\dot{\delta}, d_G) = (20\,\text{deg/s}, -0.25\,\text{m})$; instability detected at $t = 0.75\,\text{s}$ with coefficient $c_u = -0.058$.

Figure 6.3: Examples of application of the stability criterion: perturbed circular motion, simple vehicle-and-driver model. $\rho = 130$ m, $u = 92$ km/h.

Parameter	Value
Dot product threshold, DP_{thr}	0.97
Distance threshold, D_{thr}	60% Cycle Amplitude
Window length (time), l (t_{win})	13 (0.12 s)
Weighting factor, w	0.25

Table 6.1: Parameters utilized for the criteria specified in stages 1 and 2.

Possible Limitations and Challenges

When analysing systems of higher dimensions, saddle-type limit cycles with more than one characteristic multiplier outside the unit circle (i.e. cycles with an unstable manifold of dimension ≥ 3) might be unveiled. Three situations can be distinguished:

- The unstable multipliers are all real. In this case, it is reasonable to expect that among the coefficients computed with (6.14), those who multiply the unstable eigenvectors must all be positive for the motion to be stable;
- The unstable multipliers are all complex. In turn, the coefficients that multiply the unstable eigenvectors are all complex, and the stability criterion cannot be applied;
- Some unstable multipliers are complex, while others are real. In this case, it is reasonable to expect that the coefficients that multiply the real unstable eigenvectors must all be positive for the motion to be stable.

Nonetheless, these considerations only represent conjectures regarding the potential implications of extending the proposed method beyond its current application. Further investigation is needed to ascertain its validity across a broader range of cases.

An additional issue to be addressed is perhaps the effective availability of the state variables and their derivatives in a real scenario. The derivatives are used to build the vector tangent to the orbit at each instant during the motion, as seen in stages 1 and 2. Since their involvement in the method is based mostly on heuristic reasoning (completely different criteria with respect to the proposed ones could even be chosen for stages 1 and 2), the tangent vectors can be computed employing a reduced state space approach, wherein only a subset of state variables are considered. Undoubtedly, the derivatives of the most relevant state variables must be included, provided that it is feasible to extract them from measurements. In the present work, the tangent vectors $\dot{\boldsymbol{z}}_0$ and $\dot{\boldsymbol{z}}$ are built relying only on $\dot{v}$, $\dot{r}$, $\dot{\delta}$ and $\ddot{\delta}$. The most critical to obtain are perhaps the first two. If the motion is

planar:

- $\dot{v}$ could be computed from the forward speed u, the yaw rate r and the lateral acceleration a_y, which are all commonly measured. Indeed, remembering Eq. (1.5) we have $\dot{v} = a_y - ur$;
- $\dot{r}$ could be computed by placing an additional accelerometer at the front or rear axle, remembering Eq. (1.6) and Eq. (1.7). For instance, if the lateral acceleration a_{1_y} at the front is known we have $\dot{r} = (a_{1_y} - a_y)/a$.

In reality, due to roll, yaw and pitching motions more than two accelerometers may be needed to extract the necessary data. As an alternative, one could measure the tyre forces and compute $\dot{v}$ and $\dot{r}$ via dynamic equilibrium equations.

On the contrary, all the state variables should in principle be utilized to compute the deviation $\bar{\boldsymbol{\xi}}$ from the periodic orbit, since to evaluate whether the maneuver is being controlled the presented method intrinsically relies on contiuously estimating the position of the orbit relative to the manifolds of the saddle-type limit cycle. In the following subsection, the results obtained considering a reduced subset of variables will be compared to those achieved using the complete set of state variables of the simple 7D vehicle-and-driver model. In case the analysis involves a more complex model, it is reasonable to expect that at least all the state variables of the simple model should be included to obtain results of acceptable accuracy. More rigorous and efficient criteria for stages 1 and 2 could perhaps allow to neglect some states.

Finally, it is worth stressing once again that the presented stability criterion can only be applied if the position of cycle points in the phase space is known. A digital twin of the vehicle (and driver) is required, alongside preliminary testing at the driver simulator, which could render the implementation of the criterion unreasonable in a real scenario. Nonetheless, the method can still be considered relevant since it makes clear, mathematically, how the saddle-type limit cycle influences the stable or unstable motion of vehicle-and-driver, and provides a real-time "stability index" (the coefficient c_u) that could be useful for control algorithms if it were feasible to apply the criterion in practice.

6.4.2. Basin of attraction: Lane Change and J-turn Maneuvers

In this section the Floquet theory-based stability criterion is utilized to compute the basin of attraction of equilibria of the simple vehicle-and-driver model, considering the motion both along a rectilinear and circular path. In this case, we consider a set of $N = 10^4$ disturbances uniformly distributed in the $(\dot{\delta}, y_G)$-plane (equivalently $(\dot{\delta}, d_G)$-plane for

circular motion), using a Sobol sequence. An initial disturbance on y_G (d_G) may refer to a violent lane change maneuver; a disturbance on $\dot{\delta}$ corresponds to a sudden J-turn maneuver, after which the driver has to return to the original path.

The response of the system to each perturbation is simulated and at each time instant the criteria defined in stages 1 and 2 are applied to assess whether the orbit is approaching the saddle-type limit cycle. If it is detected that the motion is being influenced by the limit cycle (i.e. the criterion at stage 2 is met), the current deviation of the orbit from the cycle ($\bar{\boldsymbol{\xi}}$) is expressed in the eigenbasis of the Poincarè map to evaluate whether the maneuver is being controlled or not (stage 3). As mentioned in the previous section, the tangent vectors will be computed relying solely on $\dot{v}$, $\dot{r}$, $\dot{\delta}$ and $\ddot{\delta}$. To compute the deviation $\bar{\boldsymbol{\xi}}$ instead, at first all 7 state variables are considered (v, r, ψ (θ), y_G (d_G), δ, $\dot{\delta}$, $\ddot{\delta}$); then, the results are compared to those obtained considering only v, r, δ, $\dot{\delta}$, $\ddot{\delta}$. In this case, out of the 7 eigenvectors of the map only 5 can be utilized since (6.14) must be a square system. Specifically, apart from the eigenvectors that correspond to the unit and unstable characteristic multipliers of the cycle, we select those with the smallest components of the neglected states. Results are shown in Fig. 6.4 for rectilinear motion (forward speed $u = 120$ km/h) and in Fig. 6.5 for circular motion ($u = 120$ km/h, $\rho = 130$ m).

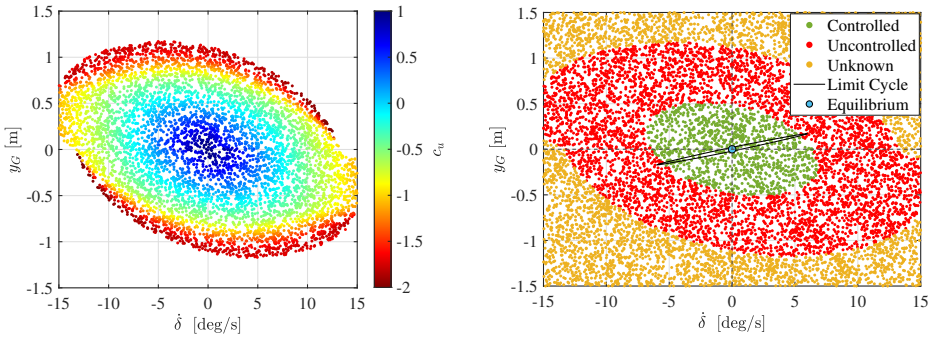

(a) Deviation $\bar{\boldsymbol{\xi}}$ computed with all state variables.

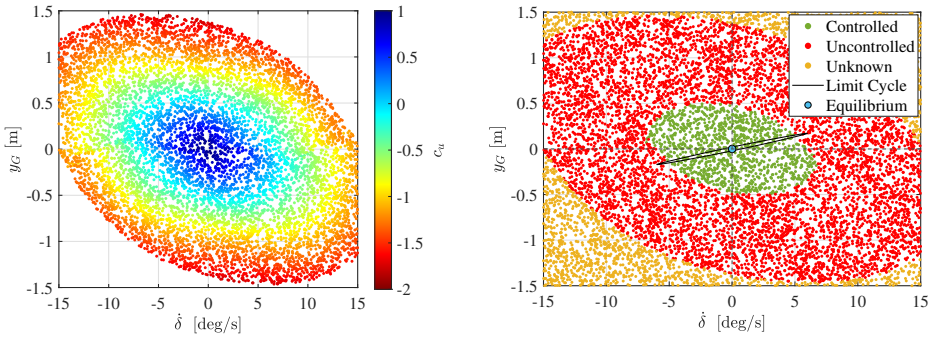

(b) Deviation $\bar{\boldsymbol{\xi}}$ computed with v, r, δ, $\dot{\delta}$, $\ddot{\delta}$ only.

Figure 6.4: Rectilinear motion, simple vehicle-and-driver model: basin of attraction in the ($\dot{\delta}$, y_G)-plane, obtained using Floquet theory. Speed $u = 120$ km/h.

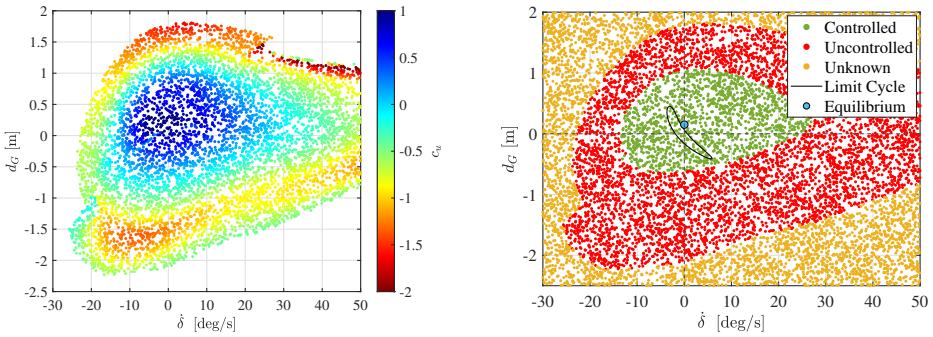

(a) Deviation $\bar{\boldsymbol{\xi}}$ computed with all state variables.

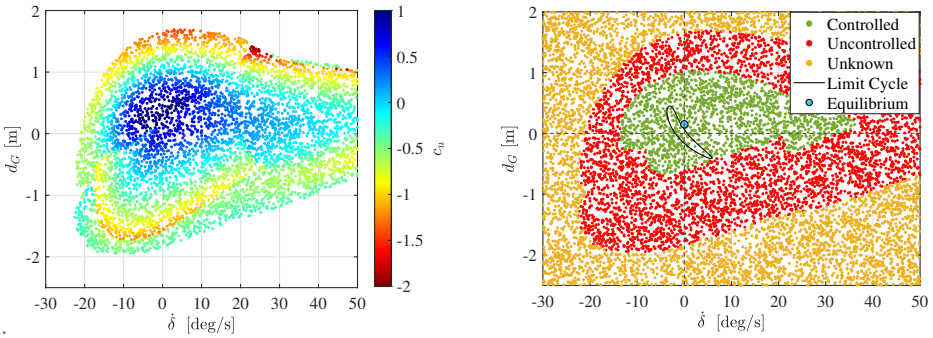

(b) Deviation $\bar{\boldsymbol{\xi}}$ computed with v, r, δ, $\dot{\delta}$, $\ddot{\delta}$ only.

Figure 6.5: Circular motion, simple vehicle-and-driver model: basin of attraction in the $(\dot{\delta}, d_G)$-plane, obtained using Floquet theory. Speed $u = 92$ km/h, curve radius $\rho = 130$ m.

The heatmaps on the left of the figures show for each simulation the value of the coefficient c_u that multiplies the unstable eigenvector of the Poincarè map, computed using Eq. (6.14) as soon as condition (6.13) is met. Orange points in the plots on the right represent initial states which lead to motions not influenced by the saddle-type limit cycle and whose stability could not be evaluated using the presented criterion (condition (6.13) was never met). The basin of attraction is always bounded by initial states that lead to $c_u \simeq 0$, i.e. that belong to the stable manifold of the saddle-type limit cycle.

The accuracy of the results was verified by computing the same stability regions utilizing the Lyapunov function described in Chapter 4; for the sake of space, the basins obtained with the Lyapunov function will not be shown here (it would be redundant regardless). Computing the deviation $\bar{\boldsymbol{\xi}}$ considering all 7 state variables (Figures 6.4a and 6.5a) allows to obtain almost the exact basin of attraction, meaning that the stability evaluation provided by the proposed criterion is quite reliable, at least for the simple vehicle-and-driver model. If $\bar{\boldsymbol{\xi}}$ is instead computed considering only a reduced subset of variables, the accuracy decreases, especially in the case of circular motion.

Further studies should be devoted to understand whether the stability criterion developed in the present work can effectively be utilized with more complex models and with real telemetry data. The treatment addressed in this chapter was aimed at providing the very basic notions and ideas that could be useful for future advancements on real-time stability sensing techniques.

Conclusions and Future Developments

In this thesis, the global stability of road vehicle and driver was studied. The primary scope was to characterise highly nonlinear behaviours exhibited by the system, expanding results coming from previous studies to steady-state cornering and providing insights into how saddle-type limit cycles can influence large motions of the system, both stable and unstable. This knowledge possibly enables the future development of control strategies that can promptly sense and correct unstable motions before a potentially fatal accident occurs, dramatically enhancing the safety of road vehicles, either human-driven or automated.

The analysis considered an oversteering vehicle, understeering at high lateral accelerations. A simple 2DoF single-track model was used for the vehicle (constant forward speed), while a single-point preview model with PD control was used to model the steering action of the driver. A third-order approximation of the delayed steering dynamics was employed, allowing a good compromise between accuracy and complexity. The coupled vehicle-and-driver system then has a total of seven state variables. Two models were developed to analyse both rectilinear and circular motion.

Initially, the local stability was studied referring to a motion slightly disturbed from steady-state, as function of the vehicle forward speed. Equilibria of the bare vehicle lose stability when one real eigenvalue becomes positive, those of the coupled system lose stability when the real part of a pair of complex conjugates eigenvalues becomes positive. The critical speed at which stability is lost is lower for lower curve radii, and is lower for vehicle-and-driver with respect to the vehicle with fixed control.

The local stability analysis lacks of realism since large motions caused by large disturbances are disregarded. The global behaviour of the vehicle, with and without driver control, was analysed performing a bifurcation analysis of the full nonlinear models. The bare vehicle undergoes a homoclinic bifurcation as the forward speed and/or steering angle are increased, through which all steady-state conditions corresponding to regular

driving (i.e. no drift) lose global, but not local stability: a stable limit cycle is generated, towards which some trajectories in the phase plane converge. This phenomenon is neither captured by a local analysis nor by an approach based on the handling diagram. Increasing further the speed and/or steering angle, the equilibrium becomes unstable through a saddle-node bifurcation and all trajectories converge to the stable cycle. Equilibria of the vehicle-and-driver system instead lose stability through a subcritical Hopf bifurcation: an unstable limit cycle exists when the equilibrium is still locally stable. The amplitude of the limit cycle increases as the speed decreases. This was shown to be true also for circular motion. Considering rectilinear motion, the Hopf bifurcation can become supercritical if driver parameters are changed. This way, a stable limit cycle exists when the equilibrium is unstable. An unstable cycle can still exist when the equilibrium is stable, although of high amplitude. The Hopf bifurcation remains instead subcritical for circular motion. It is clear that the driver fundamentally changes the behaviour of the system and the mechanism through which equilibria become unstable. In particular, the primary cause of limit cycle generation was identified in the steering actuation delay: if the delay vanishes, the Hopf bifurcation is suppressed along with the cycles, although this appears to be true only for rectilinear motion.

Unstable cycles of the vehicle-and-driver system are of the saddle type: nearby trajectories in the phase space approach the limit cycle and then they are repelled, either towards the stable equilibrium or towards a spin condition. A region of attraction then exists for the stable equilibria, delimited by the stable manifold of the cycle. Only if the initial state is inside this domain, does the system evolve towards the equilibrium. The domain of attraction for various vehicle speeds and curve radii was computed utilizing a kinetic energy-based Lyapunov function, focusing on disturbances defined on the (v, r)-plane, which correspond to the impulsive action of external forces and moments on the vehicle. At low speeds, the domain of attraction is well approximated by the Milliken diagram: the stability region is delimited by tyre saturation, in particular at the rear axle. It is then possible to detect the onset of an unstable motion by measuring tyre forces. The basin of attraction shrinks as the system operates closer to the Hopf bifurcation, for example by increasing the vehicle speed. The domain covers a significantly smaller region of the Milliken diagram, meaning that the stability threshold is quite lower than tyre saturation. In the case of circular motion, the basin of attraction appears as several distinct regions, as an interaction between multiple saddle-type limit cycles was discovered. Regardless, only the lowest amplitude cycle, which has the most influence on the system's motion, has been considered for the remainder of the work, since the simple vehicle-and-driver model is not intended to be used to characterise such complex behaviours.

To undestand if an unstable motion can be detected before the driver completely loses control of the vehicle, stable and unstable motions near the saddle-type limit cycle were analysed from a kinematic and energy standpoint, considering only rectilinear motion. The power of the rear axle lateral force is always negative, while the power at the front axle can be positive due to the driver's steering action, although the overall contribution is dissipative. The power of longitudinal forces, necessary to keep a constant speed, presents instead high positive peaks: the energy that is used to make the system unstable is taken from the forward motion, through the driver's action. If the motion is unstable, the kinetic energy increases quite abruptly a little before the tyres reach saturation: monitoring the evolution of the kinetic energy could be an effective strategy to detect an unstable motion. The same goal could be achieved by monitoring appropriately defined kinematic indices. If the motion is unstable, the diameter of the inflection circle remains low during the first instants of the exit phase of a turn, signaling that the yaw rate is not decreasing as it should. This effect becomes more evident at each oscillation, until the vehicle spins. Observing the orientation of the inflection circle or directly the moving centrodes gives information about how the front and rear slip angles are evolving at each instant during the motion. Both stable and unstable motions showed undesireable kinematic behaviour, perhaps because the lateral and yaw motions are mostly provoked by a disturbance rather than a voluntary steering action of the driver, as the fundamental component of the motion is in this case rectilinear.

Finally, a criterion to assess the stability of the motion of vehicle-and-driver close to the saddle-type limit cycle was derived based on Floquet theory. The deviation of the trajectory in the phase space from the cycle is analysed in relation to the cycle manifolds. Possible limitations and challenges include the requirement of knowing the position of cycle points in the phase space, the feasibility of measuring the state variables of the system in real-world applications, the ability to detect when the system trajectory is sufficiently close to the cycle to obtain a reliable evaluation of stability, and the adaptability of the approach when dealing with unstable manifolds of dimension greater than two. Nevertheless, the derivation of the method also serves as a formal demonstration of how the saddle-type limit cycle influences the stable and unstable motions of vehicle-and-driver, thereby highlighting its key role in global stability analysis.

This thesis work has been purely theoretical. Future developments involve above all studying the global stability of vehicle-and-driver for motions along a circular trajectory experimentally, starting at the driving simulator with a human driver in the loop. A bifurcation analysis considering a more complex vehicle-and-driver model (e.g. including throttle control by the driver or the intervention of Advanced Driving Assistance Systems)

should also be considered. Likewise, the proposed Floquet-based stability criterion should be tested on a more complex model and, if it proves viable, successively implemented at the driving simulator. Another possible research activity involves performing a study similar to the one presented by Biggio [15], aimed at developing a taxonomy of nonlinear behaviors as the tyre characteristics are varied, but considering the more realistic 7D vehicle-and-driver model and perhaps with the addition of circular motion. Additionally, a more refined study is needed to understand how the motion becomes unstable from the energy standpoint and whether a purely kinematic analysis [3] is effective in detecting the onset of unstable motions. A starting point could be to repeat the analysis presented in Chapter 5, this time focusing on circular motion.

Studies on global stability of road vehicle and driver are still in their infancy: there are many possible avenues where the research presented in this thesis can be continued, and the author is confident that any contribution will represent a substantial step towards the design of safer vehicles.

Bibliography

[1] G. Mastinu and M. Plöchl. *Road and off-road Vehicle System Dynamics Handbook*. CRC, Boca Raton, 2014.

[2] G. Mastinu, F. Della Rossa, G. Previati, M. Gobbi, and M. Fainello. Global stability of road vehicle motion with driver control. *Nonlinear Dyn.*, 111:18043–18059, 2023.

[3] M. Guiggiani. *The Science of Vehicle Dynamics*. Springer, Cham, 2018.

[4] W. F. Milliken and D. L. Milliken. *Race Car Vehicle Dynamics*. SAE, 1994.

[5] Y. A. Kuznetsov. *Elements of Applied Bifurcation Theory*. Springer, New York, 2004.

[6] J. Guckenheimer and P. Holmes. *Nonlinear Oscillations, Dynamical Systems, and Bifurcations of Vector Fields*. Springer, New York, 1983.

[7] S. H. Strogatz. *Nonlinear Dynamics And Chaos*. Perseus Books, New York, 1994.

[8] H. Pacejka. *Tire and Vehicle Dynamics*. Elsevier, Oxford, 2005.

[9] E. Ono, S. Hosoe, H. D. Tuan, and S. Doi. Bifurcation in vehicle dynamics and robust front wheel steering control. *IEEE Transactions on Control Systems Technology*, 6 (3):412–420, 1998.

[10] J. Edelmann and M. Plöchl. Handling characteristics and stability of the steady-state powerslide motion of an automobile. *Regular and Chaotic Dynamics*, 14(6):682–692, 2009.

[11] F. Della Rossa, G. Mastinu, and C. Piccardi. Bifurcation analysis of an automobile model negotiating a curve. *Veh. Syst Dyn.*, 50(10):1539–1562, 2012.

[12] C. G. Bobier-Tiu, C. E. Beal, J. C. Kegelman, R. Y. Hindiyeh, and J. C. Gerdes. Vehicle control synthesis using phase portraits of planar dynamics. *Veh. Sys. Dyn.*, 57(9):1318–1337, 2019.

[13] R. Lian and Z. Li. Lyapunov exponent based stability analysis for a high-dimensional nonlinear vehicle system under extreme conditions. To be published by SAE International, 2024.

[14] Z. Liu, G. Payre, and P. Bourassa. Nonlinear oscillations and chaotic motions in a road vehicle system with driver steering control. *Nonlinear Dyn.*, 9:281–304, 1996.

[15] D. Biggio. Analytical, numerical and experimental analysis of the non-linear vehicle/driver dynamical system. Master's thesis, Politecnico di Milano, 2018.

[16] A. Bertolami and D. M. Botto. Improving vehicle stability through milliken moment method, realtime force sensing and tire characterization. Master's thesis, Politecnico di Milano, 2023.

[17] I. Vörös. *Delayed dynamics of path-following automated vehicles*. PhD thesis, Budapest University of Technology and Economics, 2023.

[18] S. Oh, S. S. Avedisov, and G. Orosz. On the handling of automated vehicles: Modeling, bifurcation analysis, and experiments. *European Journal of Mechanics - A/Solids*, 90:104372, 2021.

[19] F. Della Rossa, M. Gobbi, G. Mastinu, C. Piccardi, and G. Previati. Bifurcation analysis of a car and driver model. *Veh. Syst. Dyn.*, 52(sup1):142–156, 2014.

[20] F. Della Rossa and G. Mastinu. Analysis of the lateral dynamics of a vehicle and driver model running straight ahead. *Nonlinear Dyn.*, 92:97–106, 2018.

[21] P. Miao, D. Li, Y. Yue, and C. Grebogi. Stability and bautin bifurcation of four-wheel-steering vehicle system with driver steering control. *Chaos: An Interdisciplinary Journal of Nonlinear Science*, 33(8):083122, 2023.

[22] W. Xianbin and S. Shuming. Vehicle coupled bifurcation analysis of steering angle and driving torque. *Proceedings of the Institution of Mechanical Engineers, Part D: Journal of Automobile Engineering*, 235(7):1864–1875, 2021.

[23] H. Wei, L. Li, Y. Xu, S. Lei, and Y. Wang. Dynamic shimmy behavior and bifurcation analysis of driver-vehicle-road system. *Meccanica*, 58:1733–1748, 2023.

[24] M. Plöchl and J. Edelmann. Driver models in automobile dynamics application. *Veh. Syst Dyn.*, 45(7-8):699–741, 2007.

[25] K. Guo and H. Guan. Modelling of driver/vehicle directional control system. *Veh. Syst Dyn.*, 22(3-4):141–184, 2007.

[26] C. C. Macadam. Understanding and modeling the human driver. *Veh. Syst Dyn.*, 40 (1-3):101–134, 2003.

[27] R. Sharp, D. Casanova, and P. Symonds. A mathematical model for driver steering

control, with design, tuning and performance results. *Veh. Syst Dyn.*, 33(5):289–326, 2000.

[28] A. Dhooge, W. Govaerts, Y. A. Kuznetsov, H. G. E. Meijer, and B. Sautois. New features of the software matcont for bifurcation analysis of dynamical systems. *Mathematical and Computer Modelling of Dynamical Systems*, 14(2):147–175, 2008.

[29] W. Govaerts, Y. A. Kuznetsov, H. G. E. Meijer, B. Al-Hdaibat, V. De Witte, A. Dhooge, W. Mestrom, N. Neirynck, A. M. Riet, and B. Sautois. *MATCONT: Continuation toolbox for ODEs in Matlab*, 2019.

[30] R. Genesio, M. Tartaglia, and A. Vicino. On the estimation of asymptotic stability regions: State of the art and new proposals. *IEEE Transactions on Automatic Control*, 30(8):747–755, 1985.

[31] C. Chicone. *Ordinary Differential Equations with Applications*. Springer, New York, 1999.

[32] J. D. Hadjedemetriou. Periodic orbits in gravitational systems. In B. A. Steves, A. J. Maciejewski, and M. Hendry, editors, *Chaotic Worlds: From Order to Disorder in Gravitational N-Body Dynamical Systems*, volume 227, pages 43–79, Dordrecht, 2006. Springer.

List of Figures

List of Tables